MEMOIRE D'HABILITATION A DIRIGER DES RECHERCHES

École Normale Supérieure de Lyon

Spécialité: Physique

présenté par

Sébastien AUMAÎTRE

le 22 juillet 2014

Fluctuations and instabilities in Out-of-equilibrium systems

DEVANT LE JURY COMPOSÉ DE:

M. Bernard CASTAING (rapporteur)

M. François DAVIAUD

M. Stéphan FAUVE (rapporteur)

M. Jean-Christophe GÉMINARD (Président)

M. Nicolas MUJICA

M. Marc RABAUD (rapporteur)

M Ingo REHBERG (excusé)

Laboratoire de Physique et Service de Physique de l'Etat Condensé (SPEC–CEA)

Contents

Chapter 1

Manuscript outline, organization and guidelines

This manuscript deals with the study of different dissipative out–of–equilibrium systems, mainly turbulent flows and granular matter. This manuscript is an opportunity to present several original results that have not been published anywhere else. The presentation of published works is reduced to the article abstracts. Hence one can consider that nearly 60% of the manuscript consists in unpublished works or projects (mainly sections 2.3, 2.4, 3.4, 3.5.1, 4.3, 4.5.3–5, and chapter 5). The division of our work into different chapters is somehow arbitrary. We do not follow the chronological order so that we obtain more coherent chapters. We choose to get each of the five chapters and even each section as self-consistent as possible. Therefore, we cannot prevent some repetitions and we apologize to readers about this. Moreover each section is introduced by a small abstract to help fast cross-reading but it also introduces some redundancy.

The chapter 2 gathers study on the role of fluctuations in out-of-equilibrium systems. The section 2.2 resumes works performed with François Pétrélis and Kirone Mallick on the action of multiplicative noise on various instabilities. Section 2.3 presents an original study, although former, on the action of a random forcing applied to dissipative systems. Several systems are reviewed. It may deserve some updates. Section 2.4 is also an original work where we test some new constrained imposed by the stationarity on the fluctuations of injected and dissipated power. This is also extended to the rate of energy transfer in a turbulent numerical model. The last section of this chapter outlines our works about the statistical properties of energy balance in granular gas.

The chapter 3 is devoted to the study of transitions in granular matter. First, in section 3.2, we summarize results obtained in a first post-doctoral position in the team of Ingo Rehberg at the Bayreuth universität where we studied ordering transition and segregation in a granular layer made of spheres and disks and driven by the horizontal swirling motion of the bottom plate. Horizontal vibration was used in our last Post-doc at Haverford College in the team of Jerry Gollub, to probe rheological transition in a set of grains. Section 3.4 gathers several practice training courses devoted to the study of a set of grains under centrifugal driving. It is more an illustration of the kinds of educational training proposed to students, than completely finished scientific work. The last section presents works performed in collaboration with Nicolas Mujica

(universidad de Chile) on a vibrated monolayer of grains. Especially, the subsection 3.5.1 presents a recent unpublished work where energetic considerations are used to predict the threshold to a phase where a bilayer cluster coexists with a less dense phase of grains in a monolayer.

The chapter 4 focuses on Magnetohydrodynamics. Section 4.2 is devoted to high magnetic Reynolds number and the dynamo effect studied in the VKS collaboration. The others sections are devoted to low Reynolds numbers where the magnetic field is almost unaffected by the flow. Section 4.3 presents an old but unpublished study on the effect of horizontal magnetic field on the efficiency of turbulent convective transport. This study initiated at the Laboratoire de Physique Statistique (LPS-ENS), has been continued and was mainly performed by François Pétrélis. Section 4.4 on instability in electromagnetically driven flow in the Taylor-Couette geometry is the post-doctoral work of Jean Boisson, whereas section 4.5 on free surface turbulence in electromagnetically driven flow is mainly the PhD thesis of Pablo Gutierrez.

The fifth and last chapter describes two additional research projects that we would like to realize in the near or distant future. They are designed as some groundwork of funding projects (the main ability required to a researcher nowadays...).

Chapter 2

Injected power and multiplicative processes in fluctuating out-of-equilibrium systems

2.1 General introduction

In this first chapter, we exhibit the part of our work that is the most closely related to our PhD thesis. It deals with the study of dissipative out-of-equilibrium systems made of a large number of degrees of freedom. Typical questions are: what can we learn on the system complexity by the study of global quantities such as the injected or the dissipated power, the heat flux or the internal energy? What are the connections between this quantities? What kind of predictions can be done on their fluctuations? When a clear separation of the scales occurs, one can try to describe the dynamics of the large scale modes by using stochastic equations where small scales are merged into a stochastic noise. This Langevin–like approach successfully describes the diffusion of large particles in equilibrium with a thermal bath of smaller particles. It has to be underlined here that we are concerned by systems intrinsically dissipative, governed by phenomenological equations where the dissipation is directly introduced via a viscous term in Navier-Stokes equation or inelastic collisions in granular gases, for instance [1].

Therefore, we are not here in the framework of the fluctuation-dissipation theorem or the fluctuation theorem, where the notion of thermostat has to be introduced and where energy exchanges of the order of kT are the only ones relevant for the theory. Indeed the fluctuation theorem, as introduced by [2, 3], and related relation [4, 5, 6], considers the fluctuations of the input power averaged on a time τ, ϵ_τ. It stipulates that the probability to observe a negative fluctuation of this quantity (let's note it: $-\epsilon_\tau$) over the probability to observe a positive one (ϵ_τ) is given by the ratio $Pr(-\epsilon_\tau)/Pr(\epsilon_\tau) = \exp(-\tau\epsilon_\tau/(k_BT))$, where T is the temperature of the thermostat with which the system is in contact. It is the equilibrium temperature of the system when there is no forcing applied. Therefore k_BT is of order of $4-5\times10^{-21}$ J at room temperature! and hence the fluctuation relation is relevant only for extremely small amount of input energy during a very short time in very small systems (like biomolecule, colloidal particles etc...). It is therefore far away from the energy and power fluctuations at work in any kind of macroscopic

dissipative systems[1].

In the first section, we are going to explore stochastic nonlinear dynamical equations to describe the dynamics of large scale variables. Many noise induced phenomena have been highlighted in such equations (starting from stochastic resonance to noise induced phase transition [7, 8]). We focus on the noise introduced by an unperfect control parameter and acting multiplicatively. This multiplicative noise is known to generate the On-Off intermittency. We evidenced this On-Off intermittency in an experimental device. In order to reconcile the experimental results and contradictory theoretical predictions, we study theoretically the effect of the low frequency noise on the instability threshold. In the next section, we consider the cases where the forcing is completely random (i.e with a zero mean value of the applied force). We are able to predict exactly the shape of the probability density function (PDF) of the injected power in the simplest model of dissipative systems and we show that, to the first order, this prediction agrees fairly well with results observed in a large variety of dissipative phenomena. In the last section of this chapter, we focus on the statistical properties of the coarse–grained rate of energy transfer in turbulent systems, where the power injected at large scales has to be transferred to small dissipative scales. This occurs via nonlinear processes. However, we show that in addition to the equality of the averages, the stationarity compels also the fluctuations of the rate of energy transfer as predicted by J. Farago [9].

[1] As noticed by Jean Farago, in macroscopic dissipative systems where negative fluctuations of the input power are observable, the fluctuation relation can be checked at least for an expansion around zero. From this procedure the one can extract an effective temperature T_{eff}. Usually one gets $T_{eff} >> T$, the real temperature of the thermostat. How this effective temperature is related to the temperature expected from the fluctuation theorem (which is assumed to hold everywhere) is still a puzzling question.

2.2 Instability with multiplicative noise: role of the low frequencies

Works in collaboration with: François Pétrélis[1] Kirone Mallick[2] Nicolas Leprovost[3]

Even simple unstable systems submitted to a multiplicative noise, present different dynamical behaviors. Above a first onset, they exhibit On–Off intermittency, i.e. their temporal trace presents random sequences of active bursts spaced by quiet and almost motionless periods. Although they have nonzero mean, their most probable value is zero. Then after a second onset, they loose this intermittent behavior and fluctuate around a finite value. We studied this behavior experimentally on the Rosenweig instability generated in a ferrofluid layer submitted to a vertical magnetic field. The multiplicative noise is introduced by a vertical random shaking of the ferrofluid layer [10]
These kinds of unstable systems have been studied mostly under the action of a multiplicative Gaussian white noise. Due to their flat power spectrum, only characterized by a single parameter, the role played by the low and high frequencies on instability cannot be distinguished. Through a van Kampen expansion, we have shown that the transition to On–Off intermittency is actually controlled by the low frequency noise. This idea has been applied successfully to analytically or numerically solvable models with different kinds of random applied forcing: harmonic noise (with two characteristic times), chaotic (coming from Lorenz equations) or dichotomous Poisson process [11, 12]. The models considered include supercritical instability and Hopf bifurcation [11, 12], potential well and Stochastic resonance [13], phase noise on parametric instability and random damping of an oscillator [14, 15].

2.2.1 Introduction and motivations

This work has been first motivated by the dynamo instability (see chapter 4 section 2). Indeed, even for the most conducting fluids the ratio of the viscosity, ν, over the magnetic diffusivity $1/(\sigma\mu_o)$ (called the Magnetic Prandtl number) is of order 10^{-5}, with μ_o the magnetic permitivity and σ the fluid conductivity. Actually it is also the ratio of the magnetic Reynolds number, $Re_m = \sigma\mu_o UL$ over the hydrodynamic one, $Re = UL/\nu$ with U and L some characteristic velocity and length scale. The magnetic Reynolds number estimates the advection of the magnetic field lines compared to their diffusion. To get amplification of the magnetic field, the magnetic field lines have to be stretched and twisted by the flow. Hence the necessary condition $Re_m \geq 1$ has to be reached to get dynamo action.It implies that $Re >> 1$ Therefore, the magnetic field will grow necessarily on a turbulent background with a highly fluctuating velocity field. If we describe the flow by a time averaged mean flow $\mathbf{U}$ plus a fluctuating part $\mathbf{u(t)}$, hence the induction equation describing the amplification on the magnetic field, $\mathbf{B}$ can be written (in a dimensionless form)

[1]LPS, École Normale Supérieure, Paris, France
[2]IphT, CEA-Saclay, France
[3]Stochastic Edge Fund, UK

$$\frac{\partial \mathbf{B}}{\partial t} = \nabla \times (\mathbf{U} \times \mathbf{B}) + \nabla \times (\mathbf{u} \times \mathbf{B}) + \frac{1}{Re_m} \Delta \mathbf{B} \tag{2.1}$$

where the fluctuating part of the velocity, u, acts multiplicatively on the unstable field, $\mathbf{B}$ through the second term of the right hand side of equation 2.1. In the VKS unconstrained dynamo experiment, fluctuations are expected to be very large (with hydrodynamics Reynolds number of order of 10^6).

During his PhD thesis, François Pétrélis tried to capture the effect of the fluctuations on the dynamo threshold [16]. He pointed out some contradictory theoretical prediction for the effect of noise on driven nonlinear oscillator. For instance, Lücke and Schank [17] performed a small noise expansion on an equation like:

$$\ddot{x} + \gamma \dot{x} = (\epsilon + \xi(t))\, x - x^3, \tag{2.2}$$

with a noise such that $\langle \xi(t)\xi(t') \rangle = \Delta^2 f(|t-t'|)$, Δ being the intensity of the noise and $f(|t-t'|)$ its normalized self-correlation function. They predicted a *normal scaling* for the moments of x above the instability threshold $\epsilon \geq 0$, i.e. $\langle x^{2n} \rangle \propto (\epsilon - \epsilon_o(\Delta))^n$ [17]. In contrast, Mallick and Marcq, starting from a more global analysis, based on the computation of the*Lyapunov exponent* of (2.2), concluded to an anomalous scaling of the moments, $\langle x^{2n} \rangle \propto (\epsilon - \epsilon_o(\Delta))$ just above the onset [18] with $\xi(t)$ a Gaussian white noise, i.e. with a Gaussian amplitude distribution and $f(|t-t'|) = \delta(t-t')$.

This contradiction is due to the intermittent time evolution of $x(t)$, induced by the multiplicative noise as first discovered by Fujisaka and Yamada [19]. This phenomena, called On–Off intermittency [20], implies power law behavior of the Probability Density Function of $x(t)$. Therefore without taking into account the nonlinear saturation, moments cannot be defined properly. This is well illustrated by the simplified over–damped version of (2.2):

$$\dot{x} = (\epsilon + \xi(t))\, x - x^3, \tag{2.3}$$

2.2.2 Experimental evidence of the On–Off intermittency

- *Intermittency at the edge of a stochastically inhibited pattern–forming instability [10]*
  F. Pétrélis, S. Aumaître, Eur. Phys. J. B **34** pp 281 (2003)

  Abstract: A layer of ferrofluid under a static vertical magnetic field is submitted to a random vertical vibration which acts as a multiplicative noise on the Rosensweig instability. At low noise amplitude the Rosensweig instability onset is delayed and our experimental results are in good agreement with the theoretical prediction of Lücke et al. [17]. For larger noise, a new regime is found where peaks appear and vanish randomly in time. Statistical properties of the temporal evolution of the fluid surface are presented.

2.2.3 Influence of the low frequencies of the multiplicative noise on various unstable phenomena

- *Low-Frequency Noise Controls On-Off Intermittency of Bifurcating Systems [11]*

  S. Aumaître, F. Pétrélis, K. Mallick, Phys. Rev. Lett. **95**, 064101 (2005)

  Abstract: A bifurcating system subject to multiplicative noise can display on–off intermittency. Using a canonical example, we investigate the extreme sensitivity of the intermittent behavior to the nature of the noise. Through a perturbative expansion and numerical studies of the probability density function of the unstable mode, we show that intermittency is controlled by the ratio between the departure from onset and the value of the noise spectrum at zero frequency. Reducing the noise spectrum at zero frequency shrinks the intermittency regime drastically. This effect also modifies the distribution of the duration that the system spends in the off phase. Mechanisms and applications to more complex bifurcating systems are discussed.

- *Effects of the Low Frequencies of Noise on On–Off Intermittency [12]*

  S. Aumaître, F. Pétrélis, K. Mallick, J. Phys. Stat. **123** pp909 (2006)

  Abstract: A bifurcating system subject to multiplicative noise can exhibit on–off intermittency close to the instability threshold. For a canonical system, we discuss the dependence of this intermittency on the Power Spectrum Density (PSD) of the noise. Our study is based on the calculation of the Probability Density Function (PDF) of the unstable variable. We derive analytical results for some particular types of noises and interpret them in the framework of on-off intermittency. Besides, we perform a cumulant expansion (N. G. van Kampen, 24, 171 (1976)) for a random noise with arbitrary power spectrum density and we show that the intermittent regime is controlled by the ratio between the departure from the threshold and the value of the PSD of the noise at zero frequency. Our results are in agreement with numerical simulations performed with two types of random perturbations: colored Gaussian noise and deterministic fluctuations of a chaotic variable. Extensions of this study to another, more complex, system are presented and the underlying mechanisms are discussed.

- *Escape from a potential well, stochastic resonance and zero frequency component of the noise [13]*

  F. Pétrélis, S. Aumaître, K. Mallick, Euro. Phys. Lett. **79** 4004 (2007)

  Abstract: For an overdamped particle evolving in a single potential and submitted to colored noise, we study numerically the problems of first passage time at the top of the

potential and of stochastic resonance. In the limit where the correlation time of the noise is small compared to the other characteristic times of the problem we show that properties of the solution related to long time behavior are controlled by the zero-frequency limit of the noise.

- *Effect of Phase Noise on Parametric Instabilities [14]*
  F. Pétrélis, S. Aumaître, S. Fauve, Phys. Rev. Lett. **94** 070603 (2005)

  Abstract: We report an experimental study on the effect of an external phase noise on the parametric amplification of surface waves. We observe that both the instability growth rate and the wave amplitude above the instability onset are decreased in the presence of noise. We show that all the results can be understood with a deterministic amplitude equation for the wave in which the effect of noise is just to change the forcing term. All the data for the growth rate (respectively the wave amplitude), obtained for different forcing amplitudes and different intensities of the noise, can be collapsed on a single curve using this renormalized forcing in the presence of noise.

- *Stability of a nonlinear oscillator with random damping [15]*
  N. Leprovost, S. Aumaître, K. Mallick, Eur. Phys. J. B **49** pp453 (2006)

  Abstract: A noisy damping parameter in the equation of motion of a nonlinear oscillator renders the fixed point of the system unstable when the amplitude of the noise is sufficiently large. However, the stability diagram of the system cannot be predicted from the analysis of the moments of the linearized equation. In the case of a white noise, an exact formula for the Lyapunov exponent of the system is derived. We then calculate the critical damping for which the nonlinear system becomes unstable. We also characterize the intermittent structure of the bifurcated state above threshold and address the effect of temporal correlations of the noise by considering an Ornstein-Uhlenbeck noise.

2.2.4 Perspectives

Recent works on the instability of a planar co–flowing sheet between liquid and gas reveal a transition from a convective instability where the unstable mode is advected downsteam to absolute instability where the unstable mode invades all the space [21]. Moreover, the phenomenology and the precise onset seem to be dependent on the level of velocity fluctuations of the inward gas flow. It is tempting to mimic these fluctuations by a multiplicative noise on a non-linear Ginzburg-Landau equation and to check how the growing spatial modes are affected by the multiplicative noise. Obviously this idea deserves much more bibliographic studies.

2.3 Injected power by a random forcing

Works in collaboration with : Claudio Falcón[1], Nicolas Mordant[2] , Eric Falcon[3], Claude Laroche[3], Stephan Fauve[4]

The fluctuations of the injected power necessary to drive a dissipative system into a nonequilibrium steady state, are studied. Here we develop the ideas presented in [22]. First, we will detail the derivation of an exact analytical formula of the PDF of these fluctuations in the simplest case of randomly forced dissipative systems. In order to do so, we compute first the joint PDF of velocity and applied force for the Brownian motion of a particle sustained by an Ornstein–Uhlenbeck (O–U) type of noise and then we deduce the PDF of their product. In this case, the Probability Density Functions (PDF) of the injected power, I, have a characteristic cusp at $I = 0$ and asymmetrical exponential tails. In the second part, we show that very different physical systems driven by a random forcing present identical features for the fluctuations of their injected power. Other related quantities like the heat flux in turbulent convection exhibit the same type of fluctuations. The agreements and discrepancies of the PDF of the model with the ones obtained in other dissipative systems are discussed in detail. Some other specific properties are also presented.

2.3.1 Short Introduction

Dissipative systems reach some interesting dynamical states only when they are forced. In that case one can always write an energy budget:

$$\frac{dE(t)}{dt} = I(t) - D(t) \tag{2.4}$$

where, E the internal energy, I the injected power and D the dissipated power, are all fluctuating variables. Indeed, usually one applies a constant force or one controls the speed of the excitation. The reaction of the system to this forcing depends on its level of complexity and goes often beyond the Le Chatelier Principle. For complex systems with many degrees of freedom this feedback will be quite fluctuating. Therefore, the injected power (product of the applied force time the propeller speed for instance in a turbulent flow) is also a fluctuating quantity. Despite the fact that it is a global variable integrated in space, the injected power will remain sensitive to large scale fluctuations. Therefore the study of injected power may be a tool to trace the complexity of out-of-equilibrium dissipative system.

Although the input power can be controlled in principle, in practice it is not so easy to do because it involves nonlinear control loops and we have to manage inertial effects to insure that

[1]Universidad de Chile, Santigo, Chile.
[2]LEGI, Université Joseph Fourier, Grenoble, France.
[3]MSC, Univeristé Denis Diderot, Paris, France.
[4]LPS, École Normale Supṕrieure, Paris, France

we control the fluctuations of power into the system[2]. Here we choose to study the limit where the forcing is perfectly random with a zero mean. We see that for a very simply linear model of dissipative system, the injected power can be computed exactly. Despite the simplicity of the model, the fluctuations of the injected power exhibit uncommon features, with asymmetrical exponential tails and a characteristic cusp around zero, the most probable value. The predicted PDF is tested on more elaborated systems submitted to a random forcing. In general there is a good agreement. Some possible causes of discrepancy like nonlinear effects or a constant drift, are discussed.

2.3.2 Power injected into a randomly forced overdamped particle

There are many experiments or models where the power is injected in a dissipative system via a random driving parameter (force or velocity). The simplest one is just an overdamped particle driven by an external random forcing. The governing equation is

$$\frac{dv(t)}{dt} = -\gamma v(t) + f(t) \tag{2.5}$$

where $v(t)$ is the velocity of a damped particle —considered as the system itself— γ is the damping coefficient and $f(t)$ is a random forcing.

This equation (2.5) is similar to Langevin equation [23], but the point of view is different. Here the system is *athermal*, because if the forcing is stopped therefore all motions just stop. But it is far from equilibrium, and $f(t)$ is an external random forcing imposed by an operator. To our knowledge, J. Farago in [24] was the first to analyze (2.5) as the simplest dissipative system fulfilling the equation (2.4) with $I(t) = f(t).v(t)$. Langevin type equations have been introduced to describe a mesoscopic particle in thermal bath, driven out–of–equilibrium, by the use of optical trap for instance [3, 25, 26, 27]. In contrast to our case, here the force applied on the particles can be split into two terms. The first is a random thermal noise, $\xi(t)$, for which the fluctuation-dissipation balance: $\gamma = \langle \xi(t)\xi(t') \rangle / (kT)$ holds. The second is the additional external force $F(t)$. This second term is the single that is taken into account theoretically to compute the power injected in a out–of–equilibrium in contact with a thermal bath.

Shape of the injected power

In [24] the fluctuations of injected power smoothed over time lag τ, I_τ, are computed for $f(t)$ taken as a Gaussian white noise. For the shortest time τ shown in [24] (equal to γ^{-1}), the computed PDF of I_τ presents one interesting feature: it has exponential non symmetrical tails. Figure 4.1 shows that this feature holds also for the PDF of the instantaneous injected power $I(t)$. These PDF are extracted from a numerical simulation of equation (2.5) where the force $f(t)$ is a O–U noise given by the equation:

[2]Experimentally, most of the time we control the force applied on the object exciting the medium, for instance the piston on granular gases or of the impellers in a turbulent stirred fluid. This is not exactly the force applied on the medium because of the inertia of the exciting object itself. One has to check that the inertial filtering of the exciter is negligeable, especially when the dynamics of the fluctuations are concerned.

$$\frac{df(t)}{dt} = -\beta f(t) + \xi(t) \tag{2.6}$$

(this is actually another Langevin equation), where $\xi(t)$ is a Gaussian white noise such as $\langle \xi(t)\xi(t')\rangle = \Delta\delta(t-t')$. Note that the number of parameters could be reduced by introducing the convenient time scale (for instance by using the dimensionless time $\tau = \beta t$ and replacing Δ by $\beta\Delta$). However it would not help necessarily for the comparisons that follow. The autocorrelation function of $f(t)$ has an exponential decay with a characteristic time $\tau_c = 1/\beta$. Two values of β are plotted in figure 4.1 for the same root mean square (rms) value of the force f and the same damping γ. In addition to the asymmetrical exponential tails, both curves present a characteristic cusp for $I = 0$. Note that a similar problem has been considered in [28] where the injected power into the Lagrangian frame of a 2D turbulent flow has been studied. Moreover the asymmetry is larger for $\beta_1 = 0.5$ than $\beta_2 = 5.0$. Actually, this captures the fact that the average of the injected power is larger for β_1 than for β_2 with $\langle I\rangle_{\beta_1}/\langle I\rangle_{\beta_2} = 4.12$. To conclude with this first example, it must be underlined that both PDF of v and f are Gaussian.

Derivation of an exact expression for the PDF of I

First, one should recall that the injected power is given by the product of two random variables, mainly a velocity $v(t)$ and a force $f(t)$, which have Gaussian distributions. They are necessarily correlated since $\langle I\rangle = \langle v.f\rangle$ does not vanish. It is a useful step to compute first the bivariate PDF, $\mathcal{P}(v,f)$, and then to deduce the PDF of I from it, by a suitable change of variable and integration:

$$\begin{aligned} P(I) &= \int_{-\infty}^{\infty} \mathcal{P}(v, I/v)dv/v \\ &= \int_{-\infty}^{\infty} \mathcal{P}(I/f, f)df/f \end{aligned} \tag{2.7}$$

Indeed, it is possible to compute $\mathcal{P}(v,f)$ for the coupled equations (2.5–2.6) since it is the solution of the solvable 2D Fokker–Planck equation [30]:

$$\partial_t \mathcal{P}(v,f,t) = -\partial_v\left[(f-\gamma v)\mathcal{P}(v,f,t)\right] + \beta\partial_f\left[f\mathcal{P}(v,f,t)\right] + \frac{\Delta}{2}\partial_{ff}^2\mathcal{P}(v,f,t) \tag{2.8}$$

The stationary solution of (2.8) is the bivariate normal distribution [30, 31]:

$$\mathcal{P}(v,f) = \frac{1}{2\pi\sigma_v.\sigma_f(1-r^2)^{1/2}} \exp\left[-\frac{1}{2(1-r^2)}\left(v^2/\sigma_v^2 - 2rvf/(\sigma_v\sigma_f) + f^2/\sigma_f^2\right)\right] \tag{2.9}$$

where

$$\sigma_f = \sqrt{\frac{\Delta}{2\beta}} \tag{2.10}$$

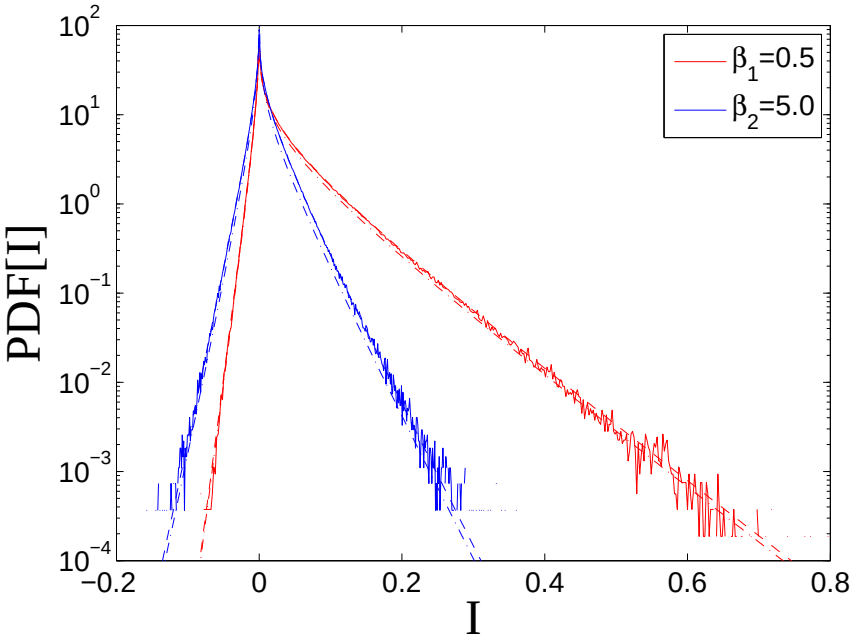

Figure 2.1: PDF of the power I injected by a random force into a damped particle following equation (2.5) with $\gamma = 1.0$. The time–correlated force obeys to (2.6) with $\beta = 0.5$ (red full line) and $\beta = 5.0$ (blue full line). In both case the rms value of force f is $\sigma_f = 0.224$. The dashed and dot-dashed lines are respectively the exact formula (2.15) and the approximated expression (2.17) of the PDF of the injected power into the dynamical systems (2.5–2.6). Numerical integration of equation (2.6) is performed within the Stratonovich interpretation. We use usual the trick with a time step in $\sqrt{\Delta t}$ to integrate the white noise [29].

is the standard deviation or rms value of f,

$$\sigma_v = \sqrt{\frac{\Delta}{2\beta\gamma(\gamma+\beta)}} \tag{2.11}$$

is the standard deviation or rms value of v, and

$$\begin{aligned} r &= \frac{\langle v.f\rangle}{\sigma_v\sigma_f} \\ &= \sqrt{\frac{\gamma}{\gamma+\beta}} \end{aligned} \tag{2.12}$$

is the correlation coefficient [31].

By integrating (2.9) over v (respectively f), it is straightforward to see that the PDF of f (resp. v) is a Gaussian with zero mean [31]. Moreover, the Cauchy–Schwartz inequality implies $\langle v.f\rangle \leq \sqrt{\langle v^2\rangle\langle f^2\rangle}$ and therefore r is always smaller or equal to one. It is worth to note that from (2.10), (2.11) and (2.12) one can deduce the mean value of the injected power from the input parameters:

$$\langle I\rangle = \frac{\Delta}{2\beta(\gamma+\beta)} \tag{2.13}$$

Note also that equation (2.10) can be recovered simply by averaging equations respectively (2.6) and (2.5) over time. Moreover the relation obtained by combining (2.10), (2.11) and (2.12):

$$\sigma_v = \sigma_f r/\gamma, \tag{2.14}$$

results from the balance between mean injected power $\langle I\rangle$ and dissipated power $\langle D\rangle = \gamma\langle v^2\rangle$ in (2.5).

With the bivariate normal PDF (2.9), the integrals (2.7) have an exact solution [32]:

$$P(I) = C\exp\left(r\frac{I}{(1-r^2)\sigma_v\sigma_f}\right)K_o\left(\left|\frac{I}{(1-r^2)\sigma_v\sigma_f}\right|\right) \tag{2.15}$$

where $K_o(X)$ is the modified Bessel function of 2d kind of zeroth order and C is a normalization constant. A more intuitive expression can be obtained by the use of the the steepest descent method to compute (2.7) with (2.9). One gets in the limit of large I:

$$\begin{aligned} P(I) &= \frac{\exp\left[rI/(1-r^2)\right]}{2\pi\sigma_v.\sigma_f(1-r^2)^{1/2}}\int_{-\infty}^{+\infty}\exp\left[-\frac{1}{2(1-r^2)}\left(v^2/\sigma_v^2\right)+I^2/(v\sigma_f)^2\right)\right]\frac{dv}{v} \\ &\sim C'\frac{\exp(\left[rI/(1-r^2)\right]}{\sigma_f}\exp\left[-\frac{1}{2(1-r^2)}\left(V_M(I)^2/\sigma_v^2\right)+I^2/(V_M(I)\sigma_f)^2\right)\right]/V_M(I) \end{aligned} \tag{2.16}$$

where $V_M(I) = \sqrt{|I|\sigma_v/\sigma_f}$ is the extremum of the exponential argument in the integral and C' is an integration constant. This leads to

$$P(X) = C''.\frac{\exp\left(rX-|X|\right)}{\sqrt{|X|}} \tag{2.17}$$

where we have introduced the reduced power: $X = I/[(1-r^2)\sigma_v\sigma_f]$ and C'' the normalization constant. This approximate expression is valid for large value of I and indeed does not give the right divergence near $I \to 0$. However, equation (2.17) gives a clear understanding of the asymmetrical decay of the PDF tails which is driven by the correlation coefficient r. At this level, we must also refer to mathematical works which have studied the PDF of the products of random variables many years ago [33]. Figure 4.1 shows that both equations (2.15–2.17) indeed fit the PDF of I obtained by numerical integration of (2.5–2.6).

2.3.3 Application to others systems

Beyond this simple model there are several real experiments or numerical models which can be randomly driven. In this section, we review few of them and we check if the PDF predicted in the simple case keeps some relevance.

Wave Turbulence

Wave Turbulence deals with the statistical steady state of a set of weakly nonlinear interacting waves, displaying Kolmogorov-Zakharov power-law spectra [34]. Although, theoretically, only the mean flux of energy $\langle I \rangle$ is important and is considered as a control parameter, experimentally large fluctuations of I appear. Moreover, the mean flux is not an experimental control parameter but it is fixed by the system itself. Here we present two wave turbulence experiments where this point is studied in the frame of random forcing.

- *Wave Turbulence experiments in water and mercury*

  A recent example of random forcing experiments in fluid dynamics is the surface wave turbulence generated by a wave–maker excited by a low–frequency Gaussian random noise [22, 35]. The authors measured simultaneously the velocity and the force applied on the moving blade of the wave–maker. Both display statistics close to a Gaussian. They deduced from these two quantities the PDF of I. Figure 2.2 (left) shows the PDF for the computed injected power for two different experimental configurations. Here, the main change in the experimental conditions was the size of the containers. For the computed curves, the working fluid was mercury (density $\rho = 13.6 \times 10^4 \mathrm{kg/m^3}$, kinematic viscosity $\nu = 1.2 \times 10^{-7} \mathrm{m^2/s}$ and surface tension $\sigma = 0.4 \mathrm{N/m}$). Once again, we see a cusp at $I = 0$ and asymmetrical tails. Note that in the smaller container the tails slightly depart from exponential fit. If the fluid is replaced by water, the main change is that tails become more symmetrical (not shown here). This fact seems to be due to the density difference, as shown in [22].

- *Wave Turbulence experiments in elastic plates*
  Bending waves on an elastic plate can also generate wave turbulence. It has been theoretically predicted that these waves can interact non-linearly between them to achieve a nonequilibrium steady state in thin elastic plates [36]. Measurements of the injected power to maintain this out-of-equilibrium steady state have been performed in a 2 $\mathrm{m^2}$ steel plate of 0.4 mm thickness (Young modulus $E = 2.0 \times 10^{11} N/m^2$, density $\rho = 7.85\ g/cm^3$). In a

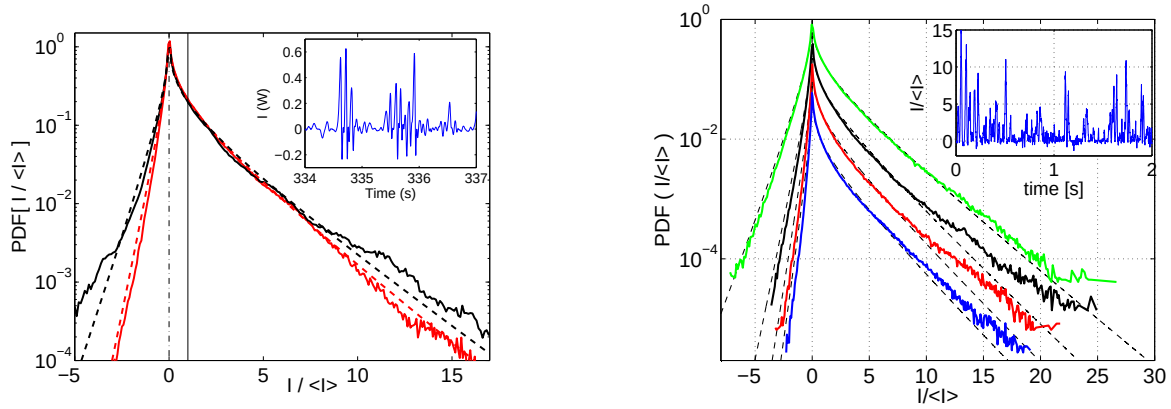

Figure 2.2: **(Left)**: PDF on the power injected by the random vibrations of a wave–maker into the surface wave turbulence for experiments in small (black) and large (red) container of mercury (from [22]). Data are normalized by its mean value $\langle I \rangle = 0.05$ [W]. The forcing is a Gaussian low frequency noise of bandwidth $[0, 6]$ Hz. Dashed line fits correspond to the formula (2.15). Vertical full and dashed lines show the corresponding average and most probable value. Inset: Temporal trace of the injected power over 3 s for the case $\langle I \rangle = 0.05$ [W]. **(Right)**: PDF of injected power into the bending elastic wave turbulence. Data is normalized by the mean value and the 4 curves have been shifted by a factor 3 for clarity. The forcing is a Gaussian low frequency noise of bandwidth $[0, 15]$ Hz. From bottom to top $\langle I \rangle = 0.64$, 0.33, 0.124 and 0.022 [W]. Dashed line fits correspond to the formula (2.15). Inset: Temporal trace of the injected power over 2 s for the case $\langle I \rangle = 0.64$ [W].

similar way as in [22], the injected power and its PDF have been computed by the means of measurements of velocity and force of the exciting piston. Figure 2.2 (Right) shows the PDF of the injected power I for different values of the rms value of the force. The typical features appear (a cusp at $I = 0$ and exponential asymmetrical tails). In this case, the larger is the rms value of the force, the larger is the asymmetry between positive and negative events of the PDF. Also we can see a small departure from the exponential tails of the PDF for large events of injected power.

Figure 2.2 shows that in both cases, equations (2.15,2.17) reproduce quite well experimental results. However, like in all real experiments, the random forcing cannot be modeled by an O–U noise. We checked that the shape of $P(I)$ is not modified by the use of more complex correlation functions for the forcing. Equation (2.5) with $\langle f(t) f(t+\tau) \rangle = \sigma_f^2 \exp(-\eta\tau) \left(\cos(\Omega\tau) + \eta/\Omega \sin(\Omega\tau)\right)$, a correlation function with two characteristic times: $1/\eta$ and $1/\Omega$ [37], has still fluctuations of the injected power given by (2.15). Of course equations (2.10–2.13) do not hold anymore but (2.14) remains true. To explain the small departure from the exponential tails observed in wave turbulence experiments in Figure 2.2, we can evocate nonlinear effects that are not taken into account in our simple model. This is explored in section 2.3.4.

The GOY shell model

Shell models have been introduced to mimic some aspects of the dynamics of fully developed turbulence in wave number space. A few tens of discrete modes are simulated with suitable short range interactions in order to reproduce the turbulent spectra. We choose here to study the *rate of energy transfer*[3] in the GOY shell model which has been optimized to mimic the turbulent intermittency [38, 39, 40]. The model follows the set of equation:

$$\frac{du_n}{dt} = \mathcal{F}(u_{n-2}, u_{n-1}, u_{n+1}, u_{n+2}) + f_4 \cdot \delta_{n,4} - \nu k_n^2 u_n \tag{2.18}$$

with $\mathcal{F}(u_{n-2}, u_{n-1}, u_{n+1}, u_{n+2}) = ik_n(u_{n+1}u_{n+2} - u_{n-1}u_{n+1}/2 - u_{n-1}u_{n-2})^*$, where $i^2 = -1$ and the * means complex conjugate and with $k_n = 2^n/16$ the wave number corresponding to the shell n and ν the viscosity. The second term in the rhs is the forcing. Instead of the usual constant forcing acting on the fourth shell, we use a random one. f_4 is given by an O–U type of noise (2.6). This allows us to keep a separation between the time scale of the injection of energy larger than dissipative one as it occurs in real turbulence. The effect of this injection time scale on the energy cascade is studied in more detail in the next section. It is shown there that such a forcing does not modify the energy cascade and the injected power fluctuations reproduce most of the statistical properties of the measured injected power in the wave turbulence experiments.

Two PDFs of I are shown in Figure 2.3. They correspond to different the correlation time $\tau_c = 1/\beta$ of the random force, keeping constant the rms value of the forcing, $\sigma_f = 7.1 \cdot 10^{-2}$, the total number of shells, $N_s = 20$, and the viscosity, $\nu = 4.0 \cdot 10^{-6}$. The asymmetry increases with τ_c, as it increases with the density of the fluid in the wave turbulence experiment. Figure 2.3 shows that equations (2.15,2.17) give a good estimation of the PDF of I as long as the correlation time of the force $\tau_c = \beta^{-1}$ is small. More precise study shows that the discrepancy begins when τ_c becomes of order of the characteristic time of the injection scale: $1/\sqrt{\sigma_f k_4} = 3.75$, with k_4 the wave number of the 4th shell where the force is applied. The reason why the discrepancy appears at that time remains an open question. However we may assume that the injection becomes more sensitive to the feedback of the shell model acting on the fourth shell, when the injection remains constant on time larger than the turnover time at the injection scale. Actually, we know that in the limit of a constant forcing, the injected power has to exhibit Gaussian fluctuations, reflecting the Gaussian fluctuations of the velocity. The action of a constant forcing is checked in the section 2.3.4. The study of the PDF of the rate of energy transfer through the following shells is postponed to the section 2.4.

A particle bouncing on random piston

It is surprising to find exactly the same shape of the PDF for the injected power in quite a different system. Indeed, the PDF of the injected power by a randomly moving piston on a single bouncing point particle are almost similar to those of the Figure 4.1 (as shown in Figure 2.4

[3]In the following we try to distinguish clearly the *rate of energy transfer* through the scales from the energy dissipation rate because their fluctuations are different although they have to be equal in average in the stationary regime.

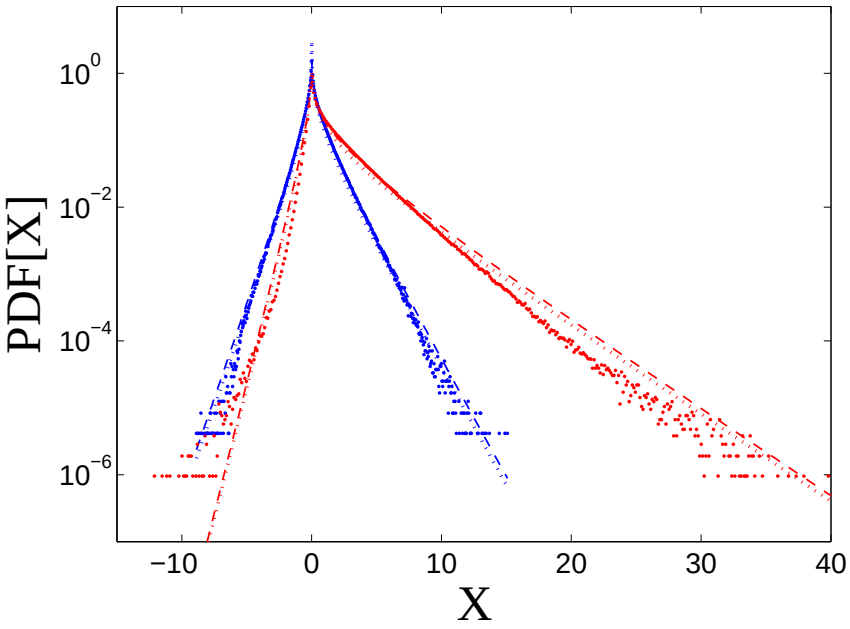

Figure 2.3: PDF of the renormalized power, $X = \frac{I/\sigma_v\sigma_f}{1-(\langle I\rangle/\sigma_v\sigma_f)^2}$, injected by a random forcing into the GOY shell model. The random force is modeled by the OU noise (2.6) with $\tau_c = \beta^{-1}$ equal to 1 (blue line) and 20 (red line) whereas other parameters: the rms value of the forcing $\sigma_f = 7.1 \cdot 10^{-2}$, the number of shells $N_s = 20$ and the viscosity $\nu = 4.0 \cdot 10^{-6}$, are kept constant. The dashed and dot-dashed lines are respectively the exact formula (2.15) and the approximated expression (2.17).

(Right)). Between collisions, the particle is submitted to a vertical gravity field of intensity g. In this 1D system, the dissipation is due to the inelastic collision between the moving wall and the particle. The rate of kinetic energy lost during a collision, characterized by a single *restitution coefficient* r, is $(1-r^2)$. The motion of the piston is a ramp between a maximum amplitude $\pm A$. The velocity of each ramp V is chosen randomly as shown in the sketch drawn in the inset of the Figure 2.4 (Left). To prevent that particle sticks on the piston, absolute piston velocities smaller than $|V_{min}| = 1.2\sqrt{gA}$ are prohibited. Elsewhere, V follows a Gaussian distribution with a standard deviation $\sigma_V \gg V_{min}$. In left part of Figure 2.4, one shows the PDF of V in a case where the prohibited velocity gap has been increased one hundred times to become visible.

In this system, the energy injected[4] at each collision is given by the product: $I = V.f$ where $f = (1+r)(V-v)$ with v the grain velocity before a collision. The right part of Figure 2.4 shows the dimensionless injected power $X/(1-\langle X\rangle^2)$ with $X = I\sqrt{1-2/\pi}/(\sigma_v\sigma_f)$ (this choice is justified in next paragraph), for two different values of r but the same value of σ_V and V_{min}. Once again, one finds the characteristic cusp at $X = 0$ and the asymmetric exponential tails. The asymmetry is larger for smaller restitution coefficient, i.e., for larger dissipation.

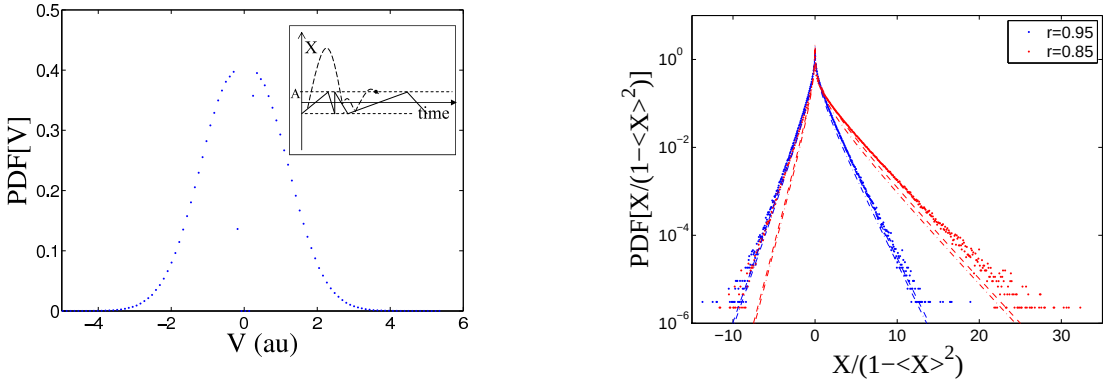

Figure 2.4: **(Left)**: PDF of the piston velocity normalized by its standard deviation σ_V with a prohibited gap between $\pm V_{min}$ (here $V_{min} = 0.3\sigma_V$). The inset shows a sketch of a trajectory where the full line gives the position of the piston and the long dashed line gives the trajectory of the ball. **(Right)**: PDF of the dimensionless power injected $X = I\sqrt{1-2/\pi}/(\sigma_V\sigma_f)$ by a random piston into an inelastic bouncing ball for a restitution coefficient $r = 0.95$ (blue line) and $r = 0.85$ (red line) where as $\sigma_V = 500\sqrt{gA}$ and $V_{min} = 1.2\sqrt{gA}$. The dashed and dot-dashed lines are respectively (2.15) and (2.17).

This is a surprising result because we must underline that although the mean piston velocity is zero, it most probable value is not zero because of the cut off introduced to prevent the sticking. Moreover the PDF of f is not a Gaussian in this model since the particle must have a velocity $v \leq V$ to collide with the piston and therefore the fluctuations of the momentum transfer $f = (1+r)(V-v)$ are always positive. In order to take that into account, we assume a semi–Gaussian PDF of $f(t)$ as a first crude approximation

[4]We consider here the energy because in this model the collisions are instantaneous. Therefore the power injected and dissipated during the collision are infinite. However, since dissipation and injection arise simultaneously, the balance between mean injection and mean dissipation holds also for the energy.

$$P(f) \quad = \sqrt{\tfrac{2}{\pi\alpha^2}}\exp(-\tfrac{f^2}{2\alpha}) \text{ for} f \geq 0 \qquad (2.19)$$
$$= 0 \text{ for} f < 0$$

where we get the average : $\langle f \rangle = \sqrt{2/\pi}\alpha$ and the variance $\sigma_f^2 = \alpha^2(1-2/\pi)$. By substituting σ_f by α in the argument of the exponential of the bivariate distribution (2.9) and in the definition of r (given in equation 2.12)), and by changing $\sqrt{2\pi}\sigma_f$ to $\sqrt{2/\pi}\alpha$ in the normalization factor of (2.9), one can recover the relations (2.15–2.17).

As long as the restitution coefficient, r, is close to one and the relative fluctuation of f are large compared to 1, one gets therefore a good estimation of the measured PDF of I as shown in figure 2.4–Right. But at smaller r, the PDF of f cannot be approximated by the semi-Gaussian curve (2.20), and the modified relations (2.15–2.17) does not fit the data correctly anymore, especially for the negative tail. We may also be more sensitive to the piston velocity cut–off.

Local heat transport in turbulent convection

It must be noted that this type of PDF is not specific to the injected power and have been observed with other related variables like the turbulent heat flux in convective transport. The studies on turbulent convection have been focused during long time only on the relation between the mean temperature difference, ΔT, imposed between top and bottom plate and the heat transport, Q, or in dimensionless variables between the Rayleigh number $Ra = \alpha_T g \Delta T H^3/(\nu\kappa)$ and the Nusselt number, $Nu = QH/(k\Delta T)$, with α_T, ν, κ, k respectively the thermal expansion, the viscosity, the thermal diffusivity and the thermal conductivity of the fluid, g the gravity acceleration, H the height between the thermalized plates. A typical sketch of the convective cell is depicted in figure 2.5 Only recently measurements have been performed on the fluctuations of the heat flux [41, 42, 43, 44]. It is again mostly the product of two random quantities: the velocity component $v_i(t)$, and the temperature perturbation $\delta T(t)$. These quantities have been estimated locally in the middle of a Rayleigh–Bénard convective cell [42], or by a Langrangian probe advected by the convecting fluid [43], or in numerical simulation where the spatial fluctuations can be obtained [44].

In all these cases, the PDFs present the same shape as shown in figure 2.6. The left part presents the 2 components of the dimensionless local heat flux $J_i(\vec{r},t)$, measured in [42] at the mid height of the cell close to the lateral walls where a convective large scale flow provides the most of the heat flux. In contrast to its horizontal counterpart, the average of the vertical component of this flux, $\langle J_z(\vec{r},t)\rangle$, is not expected to vanish since there is an average net heat flux from the bottom to top of the cell. The heat transport in the horizontal direction (x–axis) is more than ten times smaller, $\langle J_x(\vec{r},t)\rangle/\langle J_z(\vec{r},t)\rangle = 0.06$, therefore the PDF of the temporal fluctuations of local horizontal heat flux are almost symmetrical. The right part of figure 2.6 shows the instantaneous spatial fluctuations of the vertical heat flux estimated by a 3D direct numerical simulation of a large aspect ratio convective cell for two values for the Rayleigh number Ra [44].

We check also in figure 2.6 how equations (2.15,2.17) agree with the local heat flux fluctuations.

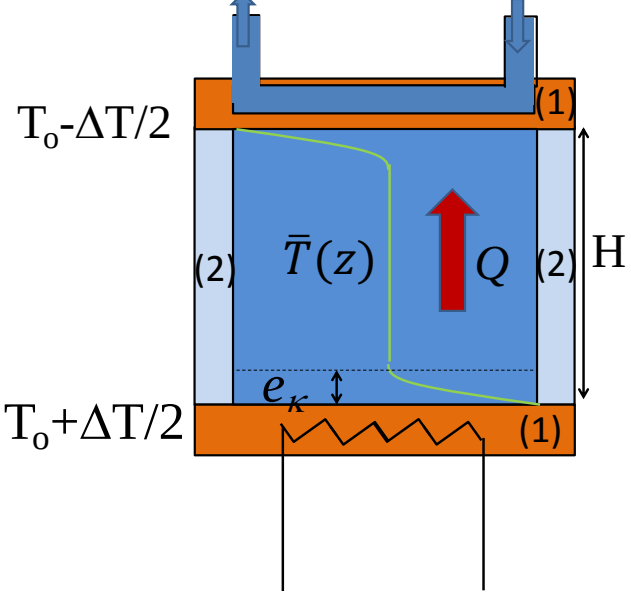

Figure 2.5: **(Left)**: Sketch of a turbulent convective cell in the Rayleigh-Bénard configuration. A fluid is enclosed between two horizontal plates made of good thermal conducting material (1) separated by a distance H. The bottom plate is heated usually with a resistive element at a temperatue $T_o+\Delta T/2$. The top plate is maintained at a temperature $T_o - \Delta T/2$ usually by a thermal bath. The insulating lateral boundary (2) insures that the mean heat flux Q is conserved along all the cell hight. In the turbulent regime the temperatures are mixed by the flow and the gradients of the mean temparature profile $\overline{T}(z)$ are concentrated in two thin thermal boundaries layer e_κ close the top and bottom plates.

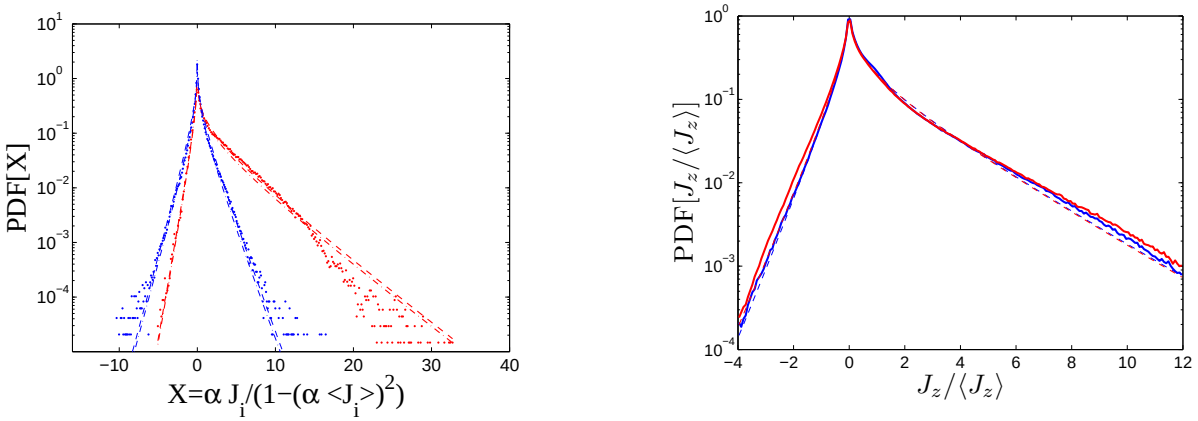

Figure 2.6: **(Left)**: PDF of the renormalized dimensionless local components of the heat transport, $X = \alpha J_i/(1 - (\alpha\langle J_i\rangle)^2)$ with $\alpha = 1/(\sigma_{v_i}\sigma_{\delta T})$, near the side wall of the convective cell in the turbulent regime (Ra=$2.6 \cdot 10^9$) extracted from [42]. Blue dots show the horizontal component whereas red dots show the vertical one. The dashed and dot–dashed lines show respectively the relations (2.15) and (2.17). The unknown coefficient α is used as fitting parameter. **(Right)**: PDF of the spatial fluctuations of the heat flux at $Ra = 10^8$ (red) and $Ra = 10^7$ (blue) extracted from [44] figure 11 a). Dashed line corresponds to relation (2.15) where r is used as fitting parameter

For local measurement close to the lateral walls, we use $\sigma_{v_i}\sigma_{\delta T}$ as a fit parameter[5]. One gets therefore $\sigma_{v_z}\sigma_{\delta T} = 254.40$ corresponding to a correlation coefficient $r_z = 0.76$ for the vertical flux and $\sigma_{v_x}\sigma_{\delta T} = 83.41$ corresponding to $r_x = 0.14$ for the horizontal one. We do not hope that these values are exactly the measured ones. Such a good agreement between the measurements and the formula (2.15) is surprising since there is a mean component to the vertical velocity and asymmetric temperature fluctuations. A simultaneous measurement with this probe together with a probe on the opposite wall would cancel this artifact and should give similar PDF. Actually the position of the local probe migth change the shape of the PDF. In [42] the probe is placed in the large scale wind that carries a large part of the heat flux. It is important to put the sensor there, in order to obtain PDF close to the one measured by a Lagrangian sensor or computed numerically. Local measurements in the center of the cell would be less representative of the heat transport. They may show different fluctuations and the agreement would be weaker. For the instantaneous fluctuations shown in the right part of figure (2.6), we used also $\sigma_{v_z}\sigma_{\delta T}$ as fit parameter, and we find $\sigma_{v_z}\sigma_{\delta T}/Nu \sim 1.53$,

2.3.4 Remarks and comments

Nonlinear effects

To explain the small departure from the exponential tails observed in wave turbulence experiments or in GOY shell models with large correlation time in the forcing, we can assume that nonlinear effects, that are not taken into account in our simple model, affect the system. To wit, we can introduce a nonlinear velocity-dependent damping in (2.5). We choose a simple nonlinear damping that promotes large fluctuations: $\gamma(v) = \frac{\gamma_o}{1+\alpha v^2}$, although others expressions have to be tested. The right part of figure 2.7 shows that such a nonlinear damping indeed increases the number of large events. Moreover the PDF of the velocity departs from a Gaussian as shown in the inset.

Effect of a mean force

Bouncing particles and local measurements of the heat flux are examples where the mean force or temperature fluctuations are *non* zero. Hence it could appear surprising that these systems keep a similar shape of their PDF. The consequences of an additional mean component in the forcing can be checked on the model equations (2.5,2.6). Analytical computations are still possible, although the formula is given in the form of a useless series expansion [33]. We have checked numerically how the addition of a mean forcing component affects the PDF of the injected power (see Figure 2.7 (left)). As long as $\langle f\rangle/\sigma_f$ is small (implying that $\langle v\rangle/\sigma_v = \sqrt{(\beta+\gamma)/\gamma}\cdot\langle f\rangle/\sigma_f$ is small for β and γ of order 1), the shape of $P(I)$ is just slightly modified. In the opposite limit, for $\langle f\rangle/\sigma_f \gg 1$ a Gaussian PDF is expected by analytical computation in agreement with Figure 2.7 (left).It is likely that most of the experimental PDF of injected power can be fitted by the intermediate cases [1, 45, 46, 47].

[5] we deduced it from a linear fit of the relation (2.21) extracted from the experimental PDF

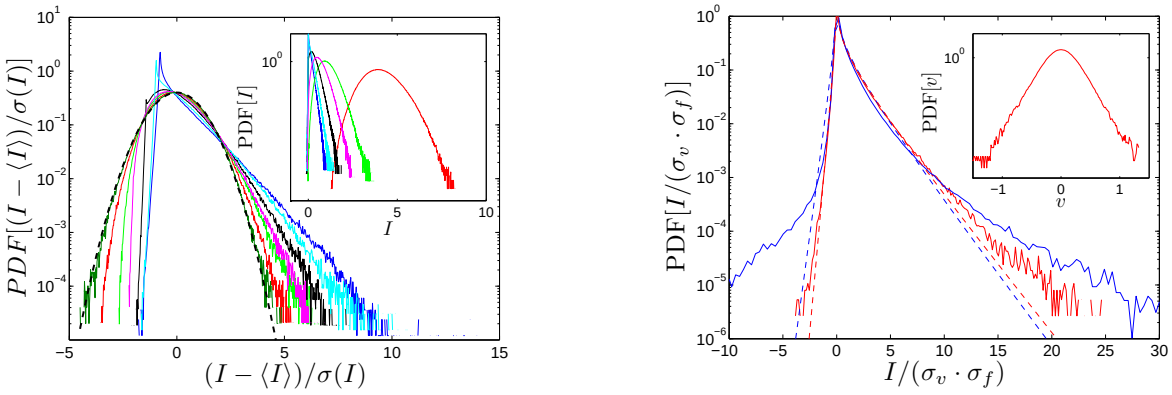

Figure 2.7: **(Left)**: PDF of the normalized injected power into the model (2.5,2.6) with a non-vanishing mean component of the applied force f with $\gamma = 1$, $\beta = 0.5$, $\sigma_f = 0.22$ and with $\langle f\rangle/\sigma_f = 0.2$ (blue); $\langle f\rangle/\sigma_f = 0.3$ (cyan), $\langle f\rangle/\sigma_f = 0.5$ (black), $\langle f\rangle/\sigma_f = 0.75$ (magenta) $\langle f\rangle/\sigma_f = 1.0$ (green), $\langle f\rangle/\sigma_f = 2.0$ (red), $\langle f\rangle/\sigma_f = 10.0$ (dark green).The dashed line is a Gaussian fit of zero mean and standard deviation equal to one. Inset: PDFs without normalization. **(Right)**: PDF of the injected power into the modified model (2.5,2.6) with a nonlinear damping coefficient $\gamma(v) = \frac{\gamma_o}{1+\alpha v^2}$ with $\gamma_o = 1$, $\beta = 0.5$, $\sigma_f = 0.22$ and with $\alpha = 1.0$ (red) and $\alpha = 2.0$ (blue). Dashed lines represent the formula (2.15). Inset: PDF of the velocity for $\alpha = 1.0$.

Some properties of the fluctuations

One can first compute the higher moments of the PDF (2.15). If we consider the dimensionless variables: $i = I/(\sigma_v\sigma_f)$, then the PDF of i , $P(i) \propto \exp\left(\frac{ri}{1-r^2}\right)\cdot K_o\left(\frac{|i|}{1-r^2}\right)$ is completely determined by the knowledge of $r = \langle i\rangle$. The first moment can be estimated by integration by part, and the resulting relative fluctuations $\sigma_i/\langle i\rangle$, the skewness $S = \langle(i-\langle i\rangle)^3\rangle/\sigma_i^{3/2}$ and the flatness $F = \langle(i-\langle i\rangle)^4\rangle/\sigma_i^4$, are respectively :$\sigma_i/\langle i\rangle = \sqrt{1+r^2}/r$, $S = (6r+2r^3)/(1+r^2)^{3/2}$ and $F = (9{+}42r^2{+}9r^4)/(1{+}r^2)^2$. Note that the relative root mean square (rms) fluctuations is a decreasing function of $r \in [0,1]$ whereas the skewness and the flatness are increasing functions of r.

One can also consider the singular limit of a white noise forcing used in [24]. It is obtained when β tends to infinity. In order to recover the Einstein's relation, one has to take σ_v^2 constant and proportional to a temperature. Therefore $\sigma_f \propto \sigma_v\cdot\sqrt{\gamma\beta} \to \infty$ and $r \to \sqrt{\gamma/\beta}$ vanishes. Assuming $\langle f(t)\cdot f(t')\rangle = D\delta(t-t')$, the Einstein relation will be written as

$$\gamma = \frac{D}{2\sigma_v^2} \tag{2.20}$$

and to recover (2.14) one has to take: $\sigma_f \overset{\beta\to\infty}{\longrightarrow} \sqrt{D\beta}$.This should allow to connect our work with [24].

Although it has been demonstrated that the Fluctuation Theorem [48] does not hold for Eq.2.5 when the temporal coarse-grained injected power is considered [24], it has to be noticed that the Gallavotti-Cohen fluctuation relation[2] works here for the instantaneous injected power I. Indeed, since $K_o(|X|)$ is even (as well as $\exp(|X|)/\sqrt{|X|}$), we get the fluctuation relation:

$$\log\left[\frac{P(I)}{P(-I)}\right] = \tau_c \frac{I}{kT} \tag{2.21}$$

where we used (2.10–2.12), $\tau_c = 1/\beta$ and we defined $kT \equiv \sigma_v^2/2$.

2.4 Some properties of the rate of energy transfer fluctuations in a turbulent model

Here, we first recall that the statistical stationarity of turbulent systems imposes several unobvious constraints on the fluctuations of the injected power, the dissipated power and the rate of energy transfer through the inertial range. In order to check the consequences of these constraints, we performed a study of the statistical properties of the rate of energy transfer in the GOY shell model. To underline how the statistical properties of the forcing propagate into the fluctuations of rate of energy transfer, we compare two types of forcing a constant and a random one. We show that, although the fluctuations of the injected power are very different, these poorly affect the fluctuations of the rate of energy transfer even in the first shells of the cascade. To explain this, we extend the result of the previous section to the PDF of the random product of an energy times a velocity. Indeed, in the beginning of the inertial range, the shape of the PDF of the nonlinear transport of the rate of energy transfer appears to be similar to the one of the correlated product of a random energy times a random velocity. We show that numerical observations on the GOY shell model are in agreement with the main constraint imposed by stationarity: the integral of the temporal correlation function of the rate of energy transfer has to be linked to the one of the injected power, and hence has to be independent of the scale in the inertial range. An extension to real 3D turbulence will be discussed to conclude.

2.4.1 Context and background

The classical scaling of the stationary, homogeneous and isotropic turbulence

Beyond their differences, all turbulent systems, including 2d and 3d turbulence and wave turbulence, merge into a common feature: they involve a constant rate of energy transfer in a large range of scales between the injection scale at which the system is forced (usually at large scale for 3D hydrodynamic turbulence) to a dissipation scale where irreversible diffusive processes become efficient. In between, in the so called inertial range, energy is just transferred scale by scale by nonlinear processes. This constant rate of energy transfer in a large range of scales in addition to dimensional considerations are enough to deduce the strongest result of homogeneous isotropic turbulence theory, the Kolmogorov fourth-fifths law[49]:

$$\langle \delta v_{//}(\mathbf{l})^3 \rangle = -\frac{4}{5}\epsilon l \tag{2.22}$$

where $\delta v_{//}(\mathbf{l}) = (\mathbf{v}(\mathbf{r}+\mathbf{l}) - \mathbf{v}(\mathbf{r})) \cdot \mathbf{l}/l$ is the velocity increment parallel to $\mathbf{l}$ and ϵ is the mean energy dissipation rate per unit of mass. This relation comes from the Karmàn-Howarth equation of the stationary, homogeneous and isotropic turbulence [49]. However, it can be deduced from dimensional arguments by assuming that the rate of energy transfer (preserved in the inertial range) through the scale l depends only on l and the velocity increment at that scale $\delta v_{//}$. Unfortunately, this reasoning does not hold for other moments, i.e. the deviations from the normal scaling $\langle \delta v_{//}(\mathbf{l})^n \rangle \propto l^n/3$ are clearly observed experimentally [50]. Several theoretical works have been devoted to explain this anomalous scaling [49]. Fluctuations of the rate of energy transfer through scales are assumed to play an important role in the statistical properties of turbulent flows [51].

Energy budget and stationarity

Like for all dissipative systems, one can write an energy budget for the hydrodynamic flows $\mathbf{u}(\mathbf{r}, t)$ by integrating Navier–Stokes equation:

$$\frac{d}{dt}\langle \mathbf{u}^2 \rangle = \langle \mathbf{f}(\mathbf{r})\mathbf{u}(\mathbf{r}) \rangle + \nu \langle \mathbf{u}(\mathbf{r})\nabla^2 \mathbf{u}(\mathbf{r}) \rangle \tag{2.23}$$

with $\langle \cdot \rangle$ standing for an averge on the whole volume of the flow and where the right hand side (rhs) represents the sum of the injected power, $I_o = \langle \mathbf{f}(\mathbf{r})\mathbf{u}(\mathbf{r}) \rangle$, and the dissipated power, $D = -\nu \langle \mathbf{u}(\mathbf{r})\nabla^2 \mathbf{u}(\mathbf{r}) \rangle = \nu \langle (\nabla \times \mathbf{u}(\mathbf{r}))^2 \rangle$. Moreover for turbulent systems, such a budget can be rewritten scale by scale in the form.

$$\frac{d}{dt}\langle \mathbf{u}_K^2 \rangle_K = I_K - \Pi'_K \tag{2.24}$$

where the subscript K means that we are dealing only with the coarse-grained quantities obtained by the use of a low pass filter upon a wave number K. Here Π'_K and I_K are: the rate of energy transfer up to K and the low pass filtered injected power respectively. For K being in the inertial range, i.e. $K^{-1} << K_o^{-1}$ the injection scale, we have $I_K \sim I_o$. In the same way, Π'_K is composed of two terms: $\Pi'_K = 2\nu\Omega_K + \Pi_K$. The first one, $2\nu\Omega_K$, where $\Omega_K = \langle |\omega_K|^2 \rangle$ is the cumulative enstrophy and where ω_K is the low pass filtered vorticity. This term is relevant only at small scale. The second, Π_K, is related to $\delta v_{//}(l)^3$ with $l \propto K^{-1}$. It is the nonlinear energy transfer. It is predominant in the inertial range [49].

Now, assuming that the system is statistically stationary, this imposes several constraints. First, one gets from (2.23) the obvious relation: $\overline{\langle I_o \rangle} = \overline{\langle D \rangle}$ where $\bar{\cdot}$ stands for time average and $\langle \cdot \rangle$ stands for an averge on the whole volume of the flow, as before . This means that, in average, the injected power has to be dissipated to reach a stationary state. In the same way in the inertial range, where $\Pi'_K \sim \Pi_K$, one gets $\overline{\langle I_o \rangle} = \overline{\langle \Pi_K \rangle}$. Assuming that Π_K only depends on u_K and $K \sim 1/l$ in the inertial range, by dimensional analysis one expects $\Pi_K \propto u_K^3 K$. Therefore, the scaling of the relation 2.22 is recovered. However the stationarity involves more relations between the fluctuating quantities of the right hand side of (2.23,2.24), which have been underemployed

until now. Indeed as shown in [24], the convergence of the large deviation function [52] associated with the smoothed quantities

$$I_\tau(t) = \frac{1}{\tau}\int_t^{t+\tau} I(t')dt'; D_\tau(t) = \frac{1}{\tau}\int_t^{t+\tau} D(t')dt'$$

implies a hierarchy of relations between the fluctuations of I and D as long as the energy has a finite correlation time. For instance, it has been demonstrated in [24][6]

$$\int_0^\infty \langle \Delta I(t+\theta)\cdot\Delta I(t)\rangle d\theta = \int_0^\infty \langle \Delta D(t+\theta)\cdot\Delta D(t)\rangle d\theta \tag{2.25}$$

with $\Delta X = X - \overline{X}$. With the usual definition of the correlation time: $\tau_X = 1/\sigma(X)^2 \int_0^\infty \langle \Delta X(t+\theta)\cdot\Delta X(t)\rangle d\theta$, $\sigma(X)$ being the standard deviation of X, (2.25) can be written :

$$\tau_I \cdot \sigma(I)^2 = \tau_D \cdot \sigma(D)^2. \tag{2.26}$$

This shows that fluctuations of injected and dissipated power are related, while they can occur at very different scales. Note that for a perfectly controlled injected power, which is formally possible but never used experimentally in practice, equation (2.26) loses its pertinence, since the rhs is undetermined.

As all these relations hold as well for (2.24). One can write in the inertial range:

$$\int_0^\infty \langle \Delta I(t+\theta)\cdot\Delta I(t)\rangle d\theta = \int_0^\infty \langle \Delta \Pi_K(t+\theta)\cdot\Delta \Pi_K(t)\rangle d\theta \tag{2.27}$$

$$\tau_I \cdot \sigma(I)^2 = \tau_\Pi \cdot \sigma(\Pi_K)^2. \tag{2.28}$$

Consequently, the fluctuations of the rate of energy transfer in the inertial range have to be connected to the fluctuations of the injected power at large scale. Moreover the relation (2.28) clearly shows that the normal scaling does not hold. Using the normal scaling with $\langle |u_k|^p\rangle \propto k^{p/3}$, we have $\tau_\Pi \cdot \sigma(\Pi_K)^2 \propto I_o^{5/3} K^{-2/3}$. Indeed $\sigma(\Pi_K)^2 = \overline{(\langle \Pi_K\rangle - \overline{\langle \Pi_K\rangle})^2} \propto \sigma_I^2$, with σ_I the standard deviation of I, and where $\tau_\Pi \propto (Ku_K)^{-1} \propto I_o^{-1/3} K^{-2/3}$ is the single time scale that depend only on u_K and K as expected in the inertial range. In contrast, the lhs of equation (2.28) is independent of K.

The shell model of Geldzer, Ohkitani and Yamada (GOY)

Some simplified models of turbulence have been developed to understand the scale by scale energy transfer mechanism. One of the most popular and useful for turbulence is the GOY shell model [38, 39, 53]. This model, that tries to mimic turbulent flows in a discrete wave number space,

[6] An easiest proof has been proposed by Stephan Fauve: taking the Fourier transform of (2.23 and multiplying it by $(\hat{I}+\hat{D})^*$ (with $\hat{X}$ the Fourier transform of X), leads to $|\hat{I}|^2 = |\hat{D}|^2$ in the limit of vanishing frequency ($\omega \to 0$) hence to equation (2.25) by using the Wiener–Khintchin's theorem.

succeeded to obtain an anomalous scaling, i.e. a scaling law that differs from the normal scaling of K41 turbulent theory where $\langle |u_n|^p \rangle \propto k_n^{-p/3}$. It describes the dynamics of the set of complex variables u_n associated to the discrete wave number $k_n = 2^n/16$ with the nonlinear set of equations:

$$\frac{du_n}{dt} = \mathcal{F}(u_{n-2}, u_{n-1}, u_{n+1}, u_{n+2}) + f_4 \cdot \delta_{n,4} - \nu k_n^2 u_n \tag{2.29}$$

where $\mathcal{F}(u_{n-2}, u_{n-1}, u_{n+1}, u_{n+2}) = ink_n(u_{n+1}u_{n+2} - u_{n-1}u_{n+1}/2 - u_{n-1}u_{n-2})^*$ is the nonlinear interaction term allowing the energy transfer, f_4 is the forcing acting on the fourth shell ($\delta_{n,4}$ being the Kronecker delta), and ν^{-1} plays the role of Reynolds number. The anomalous scaling of the GOY shell model has been intensively studied. The Tab. 1 reports the discrepancy between the normal scaling: $\langle |u_n|^p \rangle \propto k_n^{-p/3}$ and the one measured with a great accuracy for the GOY shell model in [54]: $\langle |u_n|^p \rangle \propto k_n^{-\zeta_p}$.

p	1	2	3	4	5	6
$\zeta_p/(p/3)$	1.125	1.057	1.00	0.951	0.90721	0.869

Tab. 1: Anomalous scaling in the GOY shell model from [54]

Moreover, in such a model, we have easily access to the kinetic energy or the rate of energy transfer coarse– grained up to the wave number K by summing equations 2.29 once multiplied by u_n*.

We are now going to check on this GOY shell model, how the statistical properties of the injected power bias the fluctuations of the rate of energy transfer at least in the first shells of the cascade. To do so we used a constant and a random forcing, both acting on the fourth shell only. Then we will check if there is a range of wave numbers where relation (2.27) holds. The numerical code, using a fourth order Runge-Kutta integration scheme has been first implemented by P. Poggi.

2.4.2 Results

Parameters and forcing of the GOY model

We integrate a set of $N = 20$ shells of the GOY model (2.29) . We choose $\nu = 4.10^{-6}$ and therefore the shortest time scale that has to be resolved is $t_o = (\nu k_N^2)^{-1} = 6 \cdot 10^{-5}$, with $k_N = 65536$. We force only the fourth shell, either by applying a constant force with $f_{4r} = f_{4i} = \sqrt{5 \cdot 10^{-3}}$, where the subscripts r, i stand for the real and imaginary part of the force. All the parameters are chosen in order to reproduce a well established turbulent spectrum. We also apply a random forcing sustained by the Ornstein–Uhlenbeck (O–U) noise. It is described by a Langevin type equation

$$\frac{df_{4r,i}}{dt} = -\gamma f_{4r,i} + \xi \tag{2.30}$$

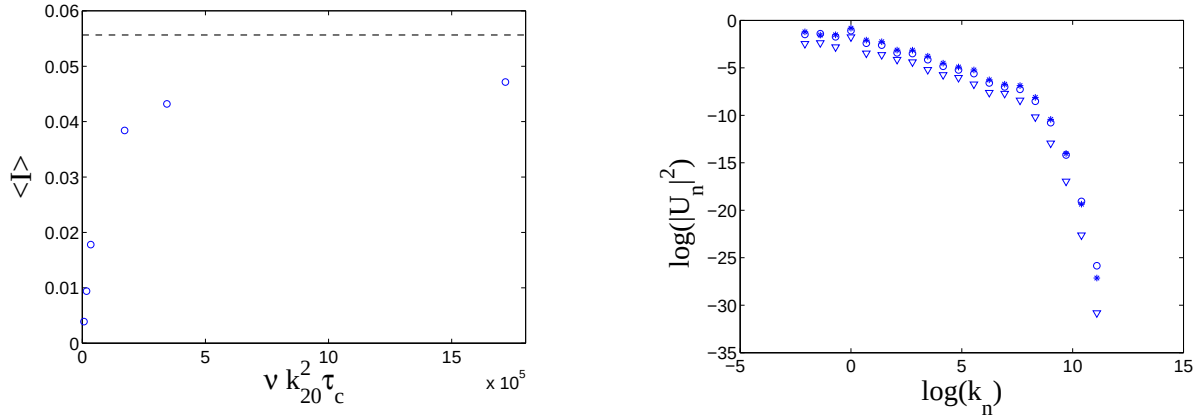

Figure 2.8: **Left**: Mean power injected by (i) a constant force (dashed line) of strength $f_o = 0.071$ and (ii) a random force ($\circ$) following eq. (2.30) with a standard deviation $\sigma_f = 0.071$ as a function the dimensionless correlation time of the force $\nu k_{20}^2 \tau_c$. **Right**: Energy spectra of the velocity amplitude for a constant forcing ($*$) for a random forcing with dimensionless correlation times: $\nu k_{20}^2 \tau_c = 1.7 \cdot 10^4$ ($\bigtriangledown$), and $\nu k_{20}^2 \tau_c = 1.7 \cdot 10^5$ ($\circ$).

where $\tau_c = \gamma^{-1}$ is the characteristic time of the forcing, and where the gaussian white noise ξ is such that $\overline{\xi(t) \cdot \xi(t')} = 2D\delta(t - t')$. In most of the result presented hereafter we choose $\gamma = 0.1$ and $D = 5 \cdot 10^{-3}$. By doing so, we expect to recover a forcing close to the constant case in the limit of infinite correlation time τ_c. Note that in order to perform statistical analysis, we need to solve (2.29) on time scale T much larger than τ_c, itself much larger than t_o.

Effect of the forcing on the turbulent cascade properties

First we check on figure 2.8 how the velocity spectra are affected by the forcing. The left part shows the injected power as a function of the correlation times of the random forcing; hence it exhibits the efficiency of the forcing to supply energy in the system. A short correlation time, i.e. shorter than t_o makes the forcing inefficient because the applied force acts mostly incoherently at the time scale of the fourth shell. But the efficiency grows rapidly with τ_c. The right part of figure 2.8 shows the variance of the velocity modes as a function of the wave number in log–log plot. It illustrates that the scaling law behaviors of the velocity spectra are not seriously affected by the characteristic time of the applied force.

Fluctuations of power with a constant forcing vs a random forcing

The next step is to study the probability density functions (PDF) of the injected power. They are shown in figure 2.9. Both forcing have quite different statistics at this level. With a constant forcing we have a smooth PDF close to a Gaussian although it has a small skewness, and has therefore a mean value close to the most probable value. In case of random forcing, PDF are

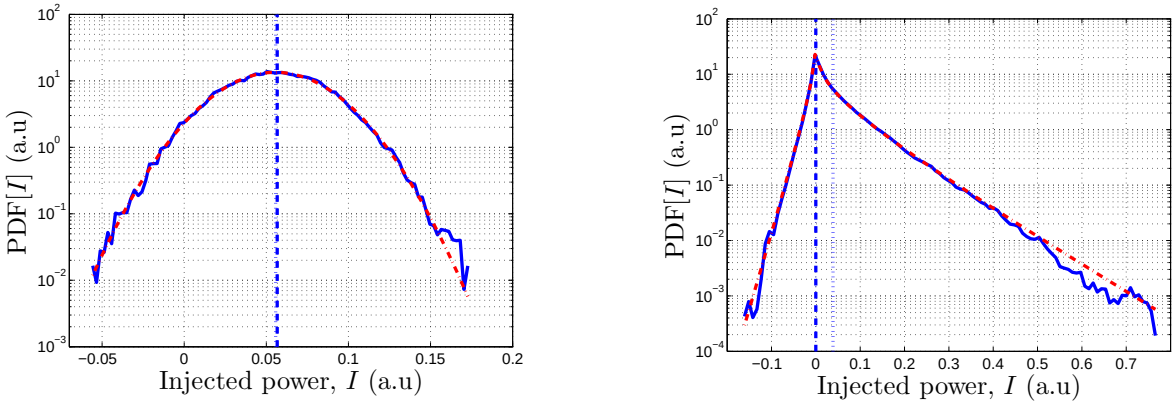

Figure 2.9: **Left**: PDF of the power injected by a constant forcing. The dot–dashed line in red gives the corresponding Gaussian fit. **Right**: PDF of the power injected by an O-U random forcing with $\gamma = 0.1$ and $D = 5 \cdot 10^{-3}$. The dot–dashed line in red is given by (2.31). The vertical dotted line and the vertical dashed line show respectively the mean and the most probable values.

far from Gaussian with their asymmetrical exponential tails and a characteristic cusp at zero which the most probable value. As shown in the previous sections of this chapter, despite this unusual shape, the PDF of the injected power can be well understood with a simple model of two Gaussian correlated variables f and u, with $\overline{f} = \overline{u} = 0$, described by two simple correlated Langevin equation as already proposed in section 1.3 and [22]. The PDF, $P(I)$, of their product can be computed exactly:

$$P(I) = C \exp\left(r \frac{I}{(1-r^2)\sigma(v)\sigma(f)}\right) K_o\left(\left|\frac{I}{(1-r^2)\sigma(v)\sigma(f)}\right|\right) \tag{2.31}$$

with $K_o(X)$ a Bessel function of 2d kind and where $r = \overline{f \cdot u}/\sigma(v)\sigma(f) = \overline{I}/\sigma(v)\sigma(f)$ is the correlator of u and f. As shown in figure 2.9, equation (2.31) perfectly fits the PDF of the power injected by a random force in the GOY shell model as long as the correlation time τ_c is not much larger than the characteristic time of injection $1/\sqrt{D.k_4} = 2.4 \cdot 10^5 t_o$. For larger τ_c, a small discrepancy can be observed between the skewness of (2.15) and that measured in the shell model (less than 30% for τ_c up to $2 \cdot 10^6 t_o$). Note that, as shown in figure 2.7 by adding a mean value, f_o, to the dynamics of f in the correlated Langevin model, one can evolve continuously from a PDF with a shape like in figure 2.9–right to figure 2.9–left just by increasing the ratio $\overline{f_o}/\sigma_f$.

PDF of the rate of energy transfer

We can now check the fluctuations of the rate of energy transfer under these two kinds of forcing. Multiplying (2.29) and summing up to a wave number $K = 2^M/16,\ M > 4$, one gets the following expression for the rate of energy transfer:

$$\Pi_K = \left[iK(u_{M+2}u_{M+1}u_M - \frac{3}{4}u_{M+1}u_M u_{M-1})^* + cc\right]/2 \tag{2.32}$$

Despite the different statistics at the level of the injected power generating the cascade, one observes in figure 2.10 that the PDF of the rate of energy transfer are almost similar in the different shells of the inertial range. That is true even in the shell next to the forcing. It is worth to note that whatever is the forcing, the rate of energy transfer in the shells next to the forced shell, shares some similarities with the power injected by random forces: a cusp in zero and positive and negative asymmetric tails. However these tails do not seem exponential. By going deeper into the shells, the asymmetry increases with less and less negative events, and the tails become fatter until the dissipative regime is reached. There a power law behavior, $P(\Pi_{17}) \propto \Pi_{17}^{-\gamma}$ is observed with a exponent γ near -2.5.

To understand the shape of the PDF in the shell next to the injection, we can remark that rate of energy transfer appears in (2.32) as the product of three random correlated variables of zero mean. Formally, from a dimensional point of view, the rate of energy transferred by the nonlinearities in the inertial range is proportional to the product of the wave number times the energy arriving at that scale times the velocity increment at that scale. Actually, in the simplest shell model [55], where shells are correlated with their nearest neighbors, the rate of energy transfer Π_i coming from shells larger than i will imply that the energy, $E_{i-1]} = U_{i-1}^2$ times the velocity of the shell i.

One can assume that the velocities keep a PDF close to a Gaussian at the beginning of the energy cascade and therefore the PDF of E_I is a χ^2 distribution, because it is the distribution for the square of a variable with a Gaussian distribution. The velocities of two successive shells are not statistically independent in the inertial range since $\langle \Pi_i \rangle \sim k_i \langle U_i U_{i+1}^2 \rangle$ is equal to the injected power. It is then tempting to use the bivariate normal distribution (2.9) to describe the conjugate distribution of the velocities of two successive shells, $\mathcal{P}(U_{i+1}, U_i)$. Then the PDF of Π_i, noted $Q(\Pi_i)$, can be estimated for large ϵ_i by integrating

$$Q(\Pi_i) = \int_{-\infty}^{+\infty} \mathcal{P}(U_{i+1}, \Pi_i / U_{i+1}^2) / U_{i+1}^2 dU_{i+1}$$

By the steepest descent method in the limit of large Π_i, one gets:

$$Q(\Pi_i) \propto \frac{\exp\left[\frac{-1}{2(1-r^2)}\left(\frac{|\Pi_i| g^+(r)}{k_i \sigma_{U_i} \sigma_{U_{i+1}}^2}\right)^{2/3} G_{\Pi_i}^+(r)\right]}{(|\Pi_i| g^+(r))^{2/3}} + \frac{\exp\left[\frac{-1}{2(1-r^2)}\left(\frac{|\Pi_i| g^-(r)}{k_i \sigma_{U_i} \sigma_{U_{i+1}}^2}\right)^{2/3} G_{\Pi_i}^-(r)\right]}{(|\Pi_i| g^-(r))^{2/3}} \tag{2.33}$$

where $r = \langle U_i U_{i+1} \rangle / (\sigma_{U_i} \sigma_{U_{i+1}})$, $g^{\pm}(r) = \sqrt{r^2+8} \pm r$, $G_{\Pi_i}^{\pm}(r) = 1 \pm 4r \; sign(\Pi_i)/g^{\pm}(r) + (2/g^{\pm}(r))^2$ and $sign(X)$ gives the sign of X. Surprisingly, this kind of PDF fits quite well the one obtained in the first shell of the inertial range of the GOY model, as shown in figure 2.11, although the rate of energy transfer, involving interactions between three successive shells, takes a more complex form in this case . Such a PDF reminds as well the shape of those measured in [56] (Fig 6), where the spatial fluctuations of the local rate of energy transfer are measured.

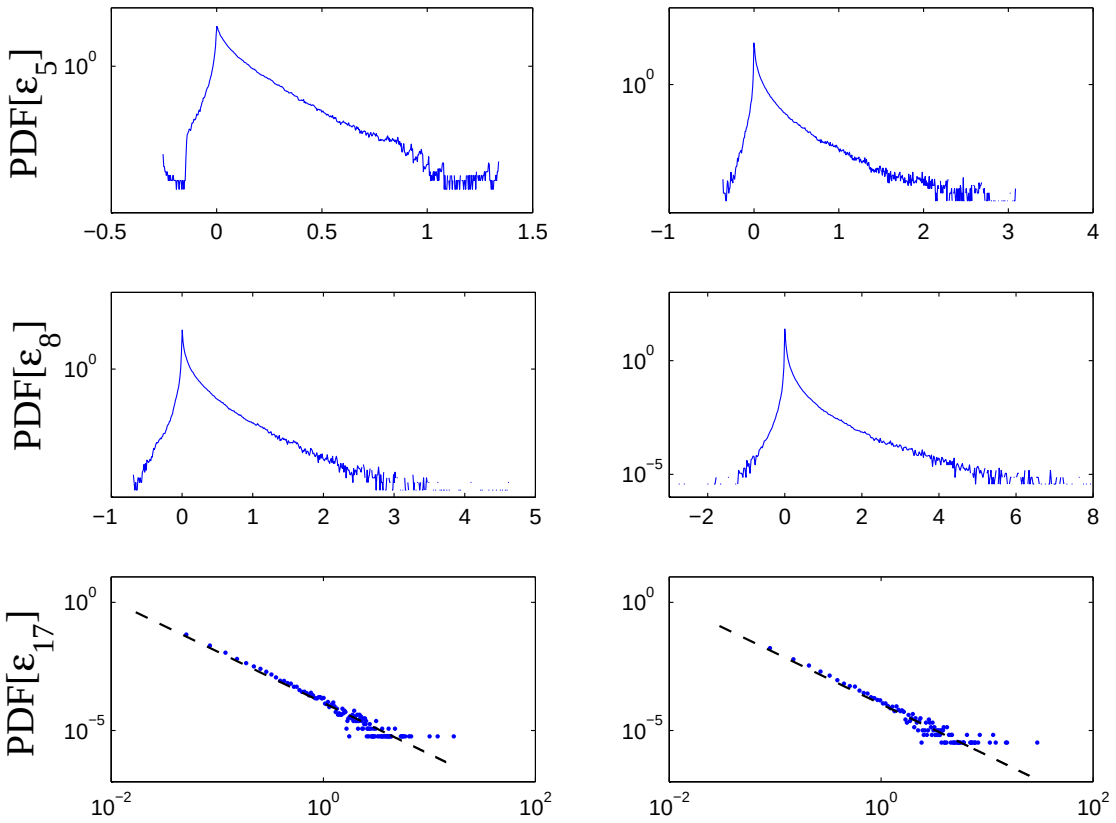

Figure 2.10: **Left**: Probability density function of the rate of energy transfer through the shell 5, 8 and 17, from top to bottom for a constant forcing. **Right :** Idem with a random forcing. The dashed lines on the bottom figures represent a power law with a exponent -2.5.

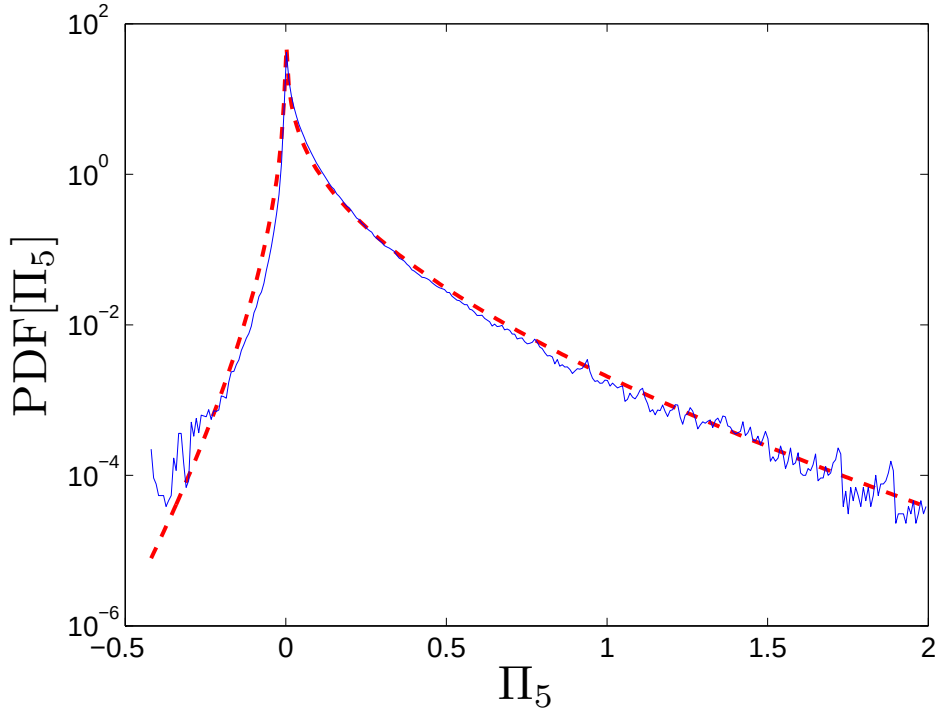

Figure 2.11: PDF of the rate of energy transfer through shell 5 (around which velocities are Gaussian) in a GOY shell model with a random forcing (continuous blue line) and its fit by (2.33) (red dashed line), where r and $\sigma_{U_i}\sigma^2_{U_{i+1}}$ are used as fitting parameters.

Correlation of the rate of energy transfer

The previous reasoning could explain the shape of the rate of energy transfer in the beginning of the inertial range as long as the velocities are Gaussian. Indeed the rate of energy transfer is just a product of correlated random variable. Therefore the forcing seems to have finally few effects on this shape of the PDF in all the following steps of the cascade. Hence the fluctuations of rate of energy transfer seem independent of the injected power. However it does not explain the modification of the PDF in the deeper shells that become more and more time–intermittent. Moreover, it does not account for the break of the normal scaling. However if equations (2.27,2.28) hold in the turbulent shell model, they may induce constraints in the cascade and they may force it to be more and more intermittent. Therefore it seems pertinent to check these equation in the GOY shell model.

In virtue of Wiener–Kinchin theorem (linking the integral of the self-correlation function to the Power Spectrum Density (PSD) at 0 frequency) instead of computing the integral of the correlation function that is noisy, it is easiest to estimate the limit at 0 frequency of the PSD of the energy transfer $S_\Pi(0)$. Despite the noise induced by the high level of intermittency of the time series, figure 2.12 shows at worst a very small dependency of $S_\Pi(0)$ with the layer of the shell up to the 15th shell. Even for this shell, when the dissipation rate $\epsilon_K = \nu \sum_{n=0}^{1} 5k_n^2 u_n^2$ is taken into account, the relation (2.27) still holds. For the higher shells, the intermittency of the temporal trace of $\epsilon_K(t)$ is too strong to obtain a reasonable limit. In any caseKi, the question of the validity of (2.27) corrected by dissipation, has to be raised, especially because a power law behavior can be observed for the PSD up to vanishing frequencies.

However, at least in the range of shells between 4 and 15, a scaling law can be deduced for the correlation time of Π_K following (2.28): $\tau_\Pi \propto S_\Pi(0)/\sigma(\Pi_K)^2$. With this definition, the correlation time of the rate of energy transfer can be fitted by a power law with an exponent close to 1/4 as shown in figure 2.13. It is worth to notice that this result is in agreement with the anomalous scaling of the GOY shell model given in Tab.1 and in turbulent measurement [49, 50]. Indeed assuming that $\sigma(\Pi_{k_n})^2 \propto k_n^2 \langle |u_n|^6 \rangle$, one gets $\tau_\Pi \propto k^{-0.262}$ since $\zeta_6 \sim 1.738$ in Tab.1 with $\langle |u_n|^6 \rangle \propto k_n \zeta_6$. However, this result differs from [54] where the correlation time of the rate of energy transfer is proposed to be $\tau_\Pi \propto k^{-0.78}$. Note that in ref. [54] another definition of τ_Π is used. This definition necessitates an a priori fitting function to describe the correlation function of the rate of energy transfer at short time. Our definition has the benefit of simplicity but can miss complex behaviors involving different correlation time scales. If this discrepancy is not yet fully understood, one can suspect that both definitions probe different time scales. Indeed only short time scales are probed with the fitting procedure proposed in [54].

2.4.3 Concluding remarks

Although the statistical properties of the injected power are sensitive to the type of forcing (constant or random), we show that in contrast, the PDFs of the rate of energy transfer in the cascade, seem insensitive to the injected power statistics even near the forcing scale. We suspect that it is due to the fact that the PDFs of rate of energy transfer result from the product of 3 random velocities that are almost Gaussian near the forcing scale. Beyond this apparent

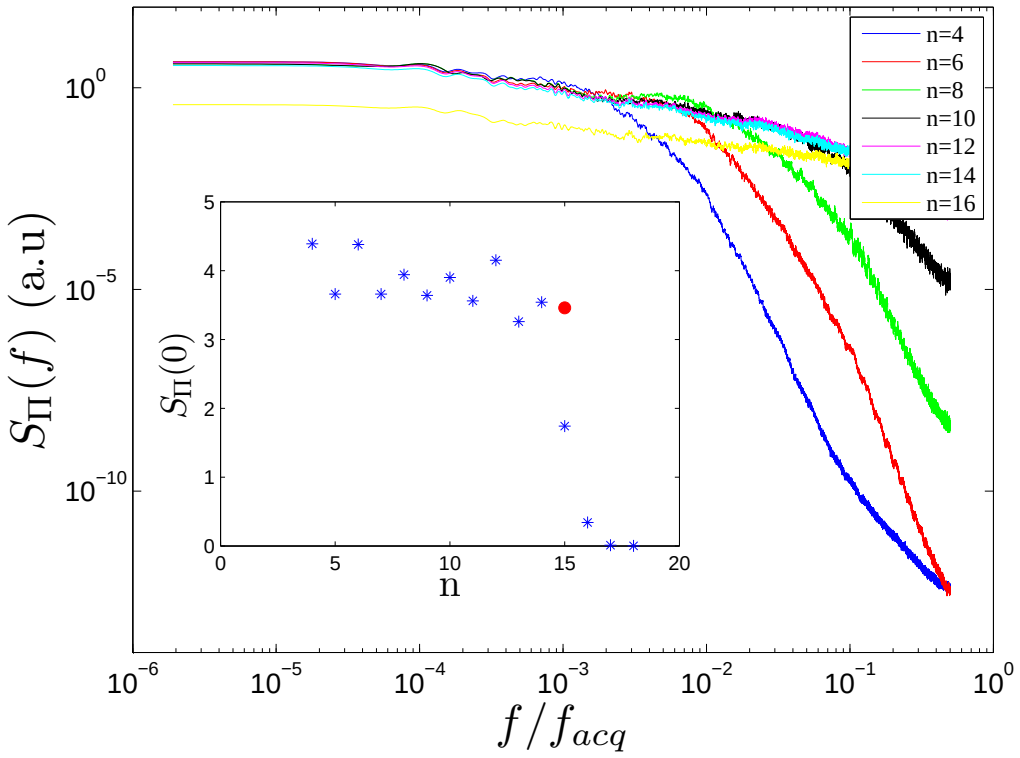

Figure 2.12: Power spectral density of the rate of energy transfer Π_K,$S_\Pi(f)$ for different shell layers. The blue asterix in inset show the smallest frequency limits of this PDS, $S_\Pi(0)$. The red dot shows for the 15th shell, the limit of the PDS at null frequency when dissipation is taken into account.

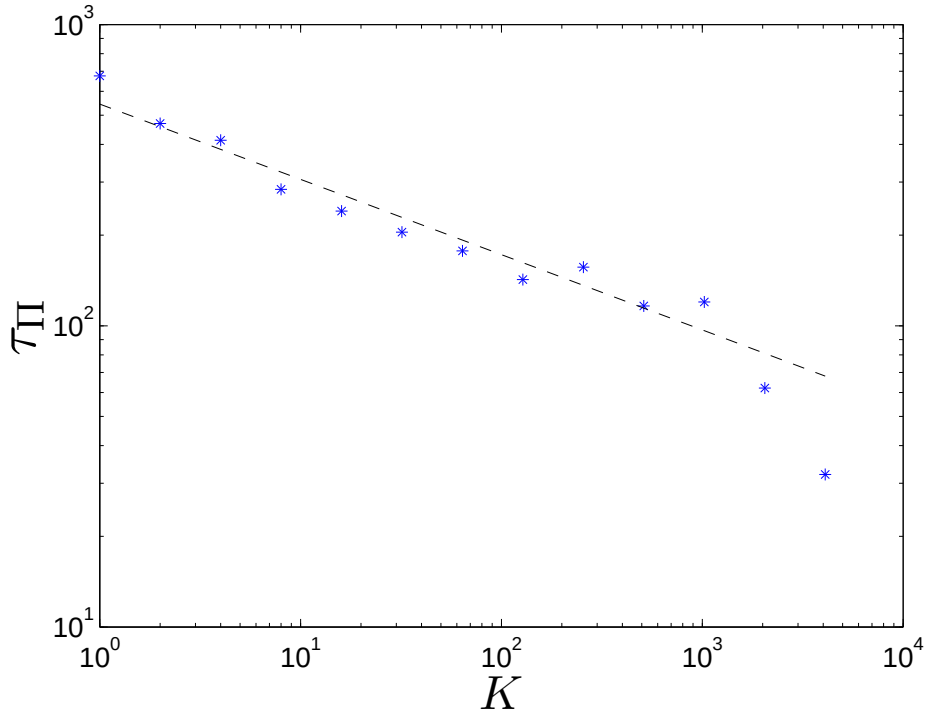

Figure 2.13: Correlation time of the rate of energy transfer τ_Π. The dashed line is a power law, $\tau_\Pi \propto K^{1/4}$.

disconnection between the statistics of the injected power and the rate of energy transfer, these quantities are actually correlated due to the constraints imposed by stationarity. This kind of correlations can not be studied with the probability density function. By analysing the Power Density Spectra of the rate of energy transfer, we show that the relation (2.27) that links the fluctuations of the injected power with the ones of the rate of energy transfer, holds in the GOY shell model as long as the intermittency is not too strong, i.e. until the 15th shell. At higher wave number where the system becomes highly intermittent, the power density spectrum of the rate of energy transfer seems to tend to a power law. Hence it is not finite at vanishing wave numbers anymore and the integral of the self-correlation function of the rate of energy transfer might diverge. The pertinence of equation (2.27) is therefore questionable, although it is found on strong arguments based on stationarity. Relation (2.27) might be recovered if the part of the energy dissipated in each of the high wave number shell, is taken into account. Unfortunately, even for the simplified GOY shell model, the convergence of the statistics is so slow that it is difficult to be really conclusive.

The correlation time of the rate of energy transfer differs from the unique time scale, τ_n that can be built in the inertial range if the scaling hypothesis of the classical Kolomogorov 41 (K41) theory is accepted. Indeed assuming that the only relevant quantities are $|u_n|$ and k_n in the inertial range, thus one get that $\tau_n \propto 1/(\langle |u_n| \rangle k_n)$ hence $\tau_n \propto k_n^{-2/3}$. The relation (2.27) shows that the correlation time of the injected power cannot be forgotten in the inertial range. This implies the breakdown of the scaling hypothesis and we cannot assume that the fluctuations of the rate of energy transfer at one scale depend on the scale only.

To go further, one needs to understand how the constrains imposed by stationary can imply the intermittent behavior of real turbulent flows. Hence, as a first step, we need to extend the results obtained for GOY shell model to real hydrodynamic turbulence. Indeed, in 3D turbulence, the intermittency can be introduced through a scale dependent weight of the spatial averages [49]. In shell models, the notion of physical space is somewhat lost. Figure 2.14 shows the intermittency of the rate of energy transfer into shells in the inertial range and how bursts evolve. Here the average time used to compute the correlation function should have also a frequency weight dependency that has to be clarified. Another challenge is to be able to perform an experimental test of the correlation between injected power, dissipated power and rate of energy transfer. The fluctuations of injected power have been measured in the enclosed von Kármán flow [45, 46, 47]. A universal shape has been proposed to explain these fluctuations [57, 58, 59] despite the fact that experimental results are contradictory. Indeed this shape is not recovered in all experimental measurements, maybe due to system inertia and filtering problems [45, 46, 47]. There are experimental attempt to measure the time average of the rate of energy transfer in anisotropic turbulence using stereo-PIV [60] and in part of the volume of a turbulent open flow generated in a square duct using Holographic particle image velocimetry measurements [61]. However, to our knowledge, there is no attempt to correlate injected power, disspated power and rate of energy transfer through scales experimentally. Using two dimensional simulations under constant stretching [62], a first exploration has been tried in [63]. In the last part of this manuscript devoted to perspectives and further works, we propose experiments that should allow such measurements.

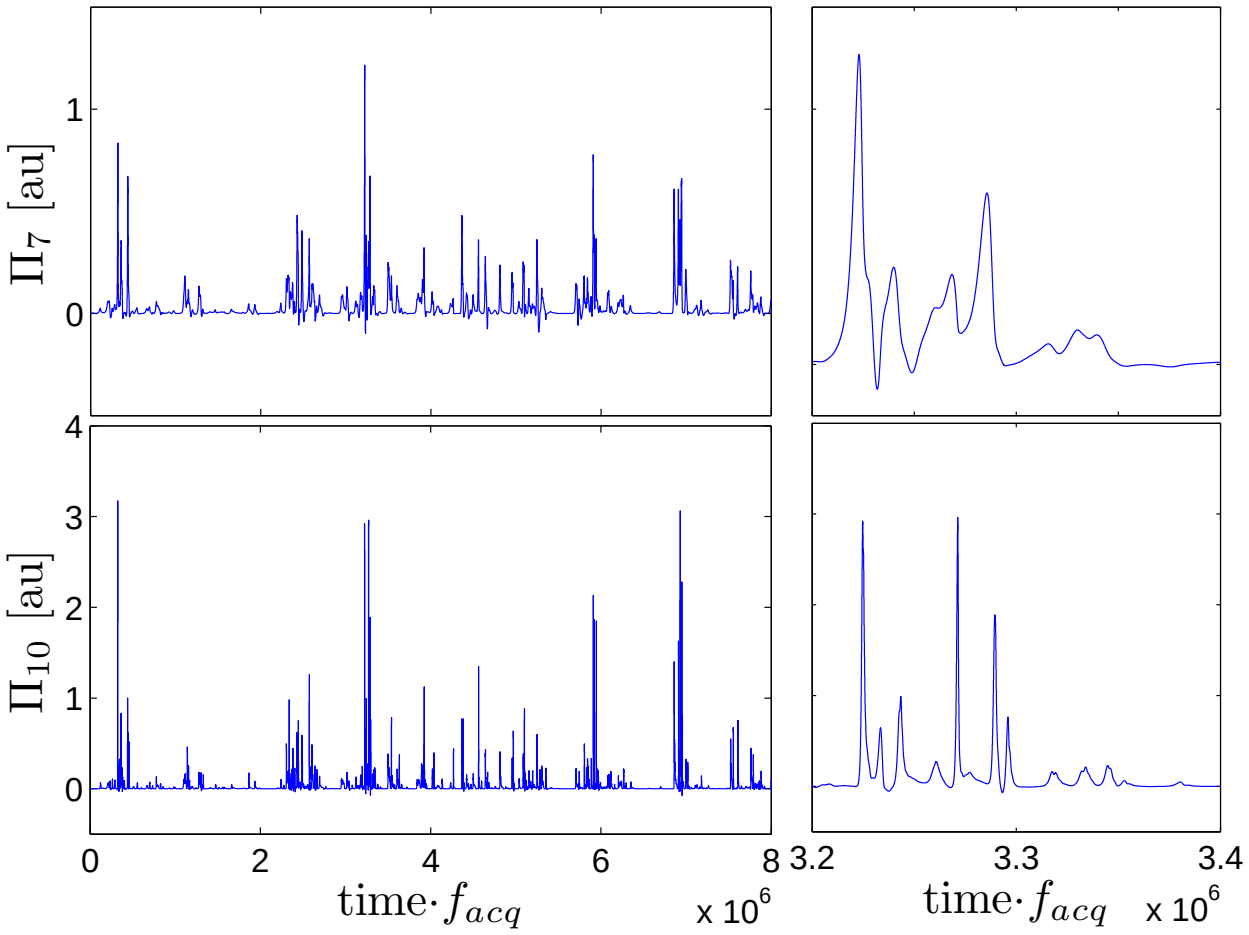

Figure 2.14: Temporal trace of the rate of energy transfer Π_i in the 7th (top) and the 10th (bottom) shell of the inertial range. Notice the different y-axis scale. The right part amplifies a burst evolution.

2.5 Statistical properties of power and energy in a granular gas and path to equilibrium

Works in collaboration with :

Stephan Fauve[1], Eric Falcon[2], Jean Farago[3], Angel Alastuey[4], Sean Mc Namara[5], Yves Garrabos[6],

Vibrated granular gas (VGG), even without external field such as gravity, is an archetype of out–of–equilibrium systems, where energy dissipation in the bulk by inelastic collisions and energy injection by a moving boundary imply spatial inhomogeneity and non-Gaussian statistics. Using event–driven molecular dynamics simulations, we studied the statistical properties of global quantities like kinetic energy $E(t)$ and the energy injected $I(t)$ or dissipated $D(t)$ per excitation period, of a set of N monodisperse disks in 2D. By a careful energy budget in the diluted limit, we established the scaling $\nu_c \propto \nu_p \propto \sqrt{N}$, for the collision frequency between particles, ν_c, and with the moving wall of the container, ν_p, where N is the number of particles [65]. This prediction is in good agreement with the measurements performed in zero-gravity flight [64]. To go further, we study the fluctuations of $E(t)$, $D(t)$ and $I(t)$ which are always related by the relation $dE/dt = I - D$ [66]. Although, $D(t)$ and $I(t)$ have to be equal in average, they are far from having similar fluctuations. From the fluctuations of the energy, which follow a χ^2-law, we extract an effective number of degrees of freedom $N_f < N$ and a corresponding effective temperature, $T_E = \langle E \rangle / N_f$ which is intensive in contrast to the usual definition of granular temperature, $T_g = \langle E \rangle / N$ that is not intensive in general. Using the framework of large deviations and a *fluctuation type relation*, we study the fluctuations around zero of the injected power smoothed over time τ: $I_\tau(t) = \int_t^{t+\tau} I(t')dt'$. It allows us to define another intensive temperature $T_F \equiv \partial F(I_\tau)/\partial(I_\tau)|_{I_\tau=0}$, where $F(I_\tau)$ is the large deviation function associated with $I_\tau(t)$. However, both temperatures, T_E and T_F are not equal. Finally, we check successfully the relation established in [9] relating correlation time and variance of the injected and dissipated power. In order to get a better understanding of the out–of–equilibrium nature of VGG, we searched for a double limit in which the dissipation tends to 0 (i.e. the restitution coefficient, r, tends to 1) and the number of grains tends to infinity. Our goal is to find a continuous path to reach a thermodynamic limit in order to check how a typical out-of-equilibrium system reaches an equilibrium state where all thermodynamic functions are well defined [67].

[1]LPS, École Normale Supérieure, Paris, France
[2]MSC, Université Paris VII, France
[3]L, Université de Starsbourg, France
[4]laboratoire de Physique, ENS-Lyon, France
[5]Stuggart, Germany
[6]ICMCB, Université Bordeaux I, France

We did that in a 2D VGG, by balancing of the energy input by the moving wall and the energy dissipated in the bulk of a 2D VGG. We extract from this balance a useful scaling to recover the quasi-elastic limit. In the scaling regime, we keep the density $n_o = N/L^2 << 1$, and $(1 - r^2)(n_o L d)$ constant when $N \to \infty$ and $r \to 1$, with L the size of the container and d the particles diameter. With this scaling, the non-dissipative case $(1-r) \to 0$, is not singular anymore if the size of the system is increased accordingly. Therefore, Gaussian fluctuations and central limit theorem are recovered. The usual granular temperature $T_g = \langle E \rangle / N$ is now intensive. Moreover in this limit the *fluctuation relation* based on the fluctuations on the injected power, gives an effective temperature equal to the usual granular temperature T_g [67]. Hence we have a tool to go continuously from the non dissipative hard sphere gas at equilibrium to a granular gas out-of-equilibrium.

- *Collision statistics in a dilute granular gas fluidized by vibrations in low gravity [64]*

  E. Falcon, S. Aumaître, P. Évesque *et al*, Europhys. Lett. **74** –5 (2006) pp 830–836

  Abstract: We report an experimental study of a dilute gas of inelastic colliding particles excited by vibrations in low gravity. We show that recording the collision frequency together with the impulses on a wall of the container gives access to several quantities of interest. We observe that the mean collision frequency does not scale linearly with the number N of particles in the container. This is due to the dissipative nature of the collisions and is also directly related to the non-extensive behavior of the kinetic energy (the granular temperature is not intensive).

- *Collision frequencies and energy flux in a dilute granular gas [65]*

  S. Aumaître, S. Fauve, Phys. Rev E, **73** 010302(R) (2006)

  Abstract: Recent experimental study of a granular gas fluidized by vibrations in a low gravity environment has reported that the collision frequency ν_p of the particles with the container boundary scales roughly like N^α with $\alpha = 0.6 \pm 0.1$, where N is the number of particles. Using numerical simulations, we show that this scaling is observed on a wide range of N, both for ν_p and for the particle-particle collision frequency ν_c. Simple scaling arguments show that this behavior is related to the energy flux in the granular gas, from injection by the moving boundary to dissipation by inelastic collisions. We predict in the dilute limit that the collision frequencies scale such as $\sqrt{N}$, in fair agreement with experimental measurements.

- *Energy and power fluctuations in vibrated granular gases [66]*

  S. Aumaître, J. Farago, S. Fauve and S. Mc Namara, Eur. Phys. J. B **42** (2004) pp255–261

Abstract: Using two-dimensional numerical simulations of a granular gas excited by vibrating one of the container boundaries, we study the fluctuations of its total kinetic energy, of the power injected into the gas by the moving boundary and of the power dissipated by inelastic collisions. We show that an effective number N_f of degrees of freedom that depends on the inelasticity of collisions can be extracted from the probability density function (PDF) of the fluctuations of the total kinetic energy E. $\langle E\rangle/N_f$ is then an intensive variable contrary to the usually defined granular temperature $T_{gr} = \langle E\rangle/N$. We then show that an intensive temperature can also be calculated from the probability of certain large deviations of the injected power. Finally, we show that the fluctuations of injected and dissipated power are related such that their ratio is inversely proportional to the square-root of the ratio of their correlation times. This allows to define a quantity homogenous to a temperature that is intensive and conserved in the process of energy dynamics from its injection by the driving piston to its dissipation by inelastic collisions.

- *A quasi-elastic regime for vibrated granular gases [67]*

  S. Aumaître, A. Alastuey, S. Fauve, Euro. Phys. J. B. **54**–2 263–266 (2006)

  Using simple scaling arguments and two-dimensional numerical simulations of a granular gas excited by vibrating one of the container boundaries, we study a double limit of small $(1-r)$ and large L, where r is the restitution coefficient and L the size of the container. We show that if the particle density n_0 and $(1-r^2)(n_0Ld)$ where d is the particle diameter, are kept constant and small enough, the granular temperature, i.e. the mean value of the kinetic energy per particle, $\langle E\rangle/N$, tends to a constant whereas the mean dissipated power per particle, $\langle D\rangle/N$, decreases like $1/\sqrt{N}$ when N increases, provided that $(1-r^2)(n_0Ld)^2 < 1$. The relative fluctuations of E, D and the power injected by the moving boundary, I, have simple properties in that regime. In addition, the granular temperature can be determined from the fluctuations of the power $I(t)$ injected by the moving boundary.

Chapter 3

Instabilities and transitions in granular matter

3.1 Introduction

The granular gas excited by a moving boundary studied (at the end of the previous chapter), is a canonical example of out-of-equilibrium dissipative systems. One important feature of this study is that the energy input at the boundary scale like L^{D-1}, for a system of size L in dimension D, whereas the energy dissipated by inelastic collisions in the bulk scales like L^D. The energy has to be transfered in the bulk and that implies inhomogeneity and non-extensivity of this kind of systems as illustrated in [68]. However, one can tune the system in a such way that the energy input occurs in the bulk with the same dimension as the dissipation. Although the extensivity is recovered at least a low density, this is still an out-of-equilibrium system exhibiting specific features induced by his dissipative nature. These features will depend on the excitation. We explored some of them.

An easy way to perform an excitation in the bulk of the granular material, is to use a monolayer. In the first type of excitation that we considered, a layer of spheres and disks are driven by the rolling and the friction induced by the swirling motion of the bottom plate. Under this excitation all spheres will roll with almost the same velocity whatever is their mass or their size. Hence, we are far from equilibrium state, since there is not equipartition of the energy between particles. A mixture of small spheres and large disks exhibit a segregation of the disks in the center due to a *shadow effect* between disks, whatever is the driving intensity and the density of small spheres or big disks[1] as long as there are collisions between the spheres and disks, pushing the disks. The clustering is induced here by the very different mobility of the two species under the excitation. The behavior of a mixture of spheres of different sizes is quite different. As long as the density of spheres is small, all kind of particles exhibit the same random motion and roll with the same velocity on the plate. Segregation and transition to an ordered phase occur only when the compressing collisions with lateral walls of the container become dominant in the energy input. We used also an horizontal periodic acceleration to underline the complex rheology of a

[1] we need at least 2 disks !

layer made of set of grains compacted under gravity..

We also use centrifugal forces to compress a layer of light grains. In a first experiment, the layer is confined between two plates and the friction on the top plate is therefore an important parameter. In a second experiment, the particles are free to move on the parabolic shape of a fluid in solid body rotation, and the capillarity becomes relevant. We also present a pedagogical example where we use the centrifugal force to explore static and rolling friction of a sphere on a parabolic support. Finally we study a horizontal monolayer of monodisperse spheres under vertical vibration. This layer is confined in 2 dimensions by 2 horizontal plates spaced by less than 2 sphere diameters. In this configuration a highly out-of-equilibrium phase transition to an ordered state is observed when the forcing amplitude is increased. We try to understand it by energetic considerations. When a dipolar interaction between grains is added, another kind of transition is observed when the system is cooled down. In the last case, the dissipative aspects of the grains seem less relevant.

3.2 Ordering and segregation in a swirled monolayer of grains

Works in collaboration with :
Ingo Rebherg [1], Christophe Krülle[2],

A monolayer of spheres can be excited on one side with a moving wall like in previous Molecular Dynamic simulations but also in the bulk, for instance by rolling on a horizontal moving table. We choose a swirling motion, i.e. a sinusoidal motion in X and Y axis of the horizontal plane, to drive a layer of monodisperse spheres enclosed in a circular boundary fixed on the moving table. At low filling fraction spheres gently roll in a disordered motion in the center of the cell. The local filling fraction of the spheres adjusts to prevent the energetic collisions with the lateral boundaries. This is not possible anymore when the filling fraction is increased above a critical value Φ_c. Lateral boundary then compresses the medium which transits into a more ordered dense state. When spheres of two sizes are put on the table, they start to segregate at the same Φ_c. Bellow this filling fraction, both species roll on the table with the same velocity [69].
Another kind of segregation is observed when spheres are mixed with cylinders. Due to friction, cylinders alone would be motionless, but they move under the action of the small colliding spheres. These collisions, and thus the mean applied force, are not symmetrical because there is a shadowing effect due to the presence of neighboring cylinders. In this case, the velocity of the clustering can be described if the collisions relevant to overcome the static friction of the cylinder on the accelerated plate are the only ones taken into account [70].

[1]EPV, Universität Bayreuth , Germany
[2], Stuggart,Germany

- *Granular Phase Transition as a Precondition for Segregation [69]*
  S. Aumaître, T. Schauntz, C.A Krülle and I. Rehberg, Phys Rev Lett **90**–11 114302 (2003)

  Abstract: Experimental results are presented on the segregation of a mixture of spheres with two different sizes, rolling on a circularly vibrating table. Beyond a critical density of particles, a demixing occurs, leading to a clustering of the larger ones. A monodisperse layer of spheres shows a liquid-solid-like phase transition at a slightly lower critical density. These critical particle densities are both found to be independent of the driving frequency, but decrease with increasing vibration amplitude.

- *Segregation in granular matter under horizontal swirling excitation [70]*

  S. Aumaître, C.A. Krülle and I. Rehberg, Phys Rev E **64** 041305 (2001)

  Abstract: A segregation phenomenon in a horizontally vibrated monolayer of granular matter is studied experimentally. In a binary mixture of small spheres and larger disks, the collapse speed of the disks increases dramatically with increasing granular temperature. The scaling behavior can be understood by applying arguments from kinetic gas theory.

3.3 Rheology of a compact layer of grains vibrated horizontally

Works in collaboration with :
Jerry Gollub [3], C. Puls[3]

A horizontal vibration was also used to check some aspects of the rheological properties of a shallow layer of thin glass grains [71]. Two hysteretic acceleration onsets, one for the starting flow, and the second for the stopping flow, have been exhibited. This was already observed in a different geometry [72]. The variation of these thresholds with the layer depth was studied and compared to onsets of flowing in the same cell placed on an inclined plane. Similar behaviors were observed although the oscillating flow presents a weaker layer depth dependency. We also studied the dynamics of the free surface of the layer under the horizontal vibration. We discovered an intermediate regime where the grains flow only during one part of the cycle. There is also a puzzling phase mismatch between the grains motion and the forcing. It has been shown recently that most of these features are shared by visco–plastic fluid layers [73].

[3]Haverford college, PN, USA

- *Comparing flow thresholds and dynamics for oscillating and inclined granular layers [71]* S. Aumaître, C. Puls, J.N. McElwaine and J. Gollub Phys Rev E **75** 061307 (2007)

Abstract: The onset and dynamics of flow in shallow horizontally oscillating granular layers are studied as a function of the depth of the layer and imposed acceleration. Measurements of the flow velocity made from the top and side are presented in the frame of reference of the container. As is also found for avalanches of inclined layers, the thresholds for starting and stopping of flow are slightly different. The variation with depth of the starting acceleration Γ_{start} for the oscillating layer is similar to the corresponding variation of the tangent of the starting angle $\tan(\theta_{start})$ for avalanches in the same container at low frequencies, but deviates as the frequency is increased. However, the threshold behavior depends significantly on the measurement protocol. Just above Γ_{start}, the motion decays with time as the material reorganizes over a minute or so, causing the apparent threshold to increase. Furthermore, the rms velocity as a function of acceleration rises more sharply above the starting threshold if the first minute or so of excitation is discarded. Once excited, the rheology of the material is found to vary in time during the cycle in surprising ways. If the maximum inertial force (proportional to the container acceleration amplitude) is slightly higher than that required to produce flow, the flow velocity grows as soon as the inertial force exceeds zero in each cycle, but jamming occurs long before the inertial force returns to zero. At higher Γ, the motion is fluid like over the entire cycle. However, the fraction of the cycle during which the layer is mobile is typically far higher than what one would predict from static considerations or the behavior of the inclined layer. Finally, we consider the flow profiles as a function of both the transverse distance across the cell at the free surface and also as a function of the vertical coordinate in the boundary layer near the sidewall. These profiles have time-dependent shapes and are therefore significantly different from profiles previously measured for avalanche flows.

3.4 Stuctures of a centrifuged layer of grains

Works in collaboration with :

Emmanuelle Debourdeau [1], Alexis Soulier[2], Vincent Padilla[3], Cecile Gasquet–Wierthel[3], Claude Laroche

[1]Stage de Ecole des ponts et Chaussées, France
[2]stage de M1 Université d'Orsay
[3]Sphinx–SPEC CEA-Saclay, France

Another way to compress the grains, is to use the centrifugal force. If some spheres immersed in a gap of a more dense fluid, are submitted to a rotational motion, they feel an inward radial pressure gradient acting like artificial buoyancy that pushes the spheres into the center. When we start with a relatively high filling fraction (about 50–60 %) we observed the formation of an annular dense structure at a given range of rotating rate. We note that this phenomenon is highly sensitive to the friction grain on the upper plate and it flatness . Then we start the study of the motion and the final equilibrium position of a floater on the parabolic free surface of a fluid in solid body rotation. We exhibit the primary role of the wetting. Finally we focus on the behavior of spheres on a rotating support of parabolic shape. We study the equilibrium position of a single sphere as a function of the rotation rate. This position is bounded by the static friction. Then, we measured the rolling friction on the same device by considering the transients to equilibrium. To go further, we will have to consider the behavior of a set of spheres when the equilibrium radius cannot contain all the particles.

3.4.1 Centrifugation of a layer fluid filled with light particles

This work was mainly performed by Emmanuelle Debourdeaux during the 3 months of her training course in spring 2010. Our aim was to study the structure of a layer of grains compressed by a centrifugal effect. To do so, we sandwiched some polypropylene spherical particles (of density 0.9) in water as depicted in figure 3.1. The gap, e, between top and bottom plate is adjustable such that $e \leq 2d$. Once the fluid reaches the solid rotation regime, one could expect that the particles mainly feel the pressure gradient compensating the centrifugal force. This should push the particles radially to the center with a strength $(\rho_f - \rho_p)V_p r\Omega^2$, with ρ_f (resp. ρ_p) is the density of the fluid (resp. the particles), V_p the volume of the particles, r its radial position and Ω, the rotation rate. In addition one should observe tangential motion induced by the Coriolis force.

Motion of a single particle

We study first the motions of a single particle. It was initially placed at the circumference of the cell. Then the cell is put in rotation. The solid rotation is reached after that the viscous dragging takes place. It occurs after a time of order of $(e^2/\nu) \sim 16$ s, with $e \sim 4$ mm the gap and $\nu = 10^{-6} m^2/s$ the kinematic viscosity of the fluid. Hence most of our measurements are not performed in the stationary regime. Moreover one has to take into account the viscous damping and the friction on the top confining wall. This latter effect is actually dominant. To reduce the friction, we add a wetting agent (moreover it helps also to remove air bubbles).

Figure 3.2–left shows the trajectory, in the co-moving frame, of a single particle driven at 2 different rotation rates. As expected these trajectories are mainly radial despite the fact that we are not in the fully solid rotation regime. Moreover, figure 3.2–right shows that in a large part of its trajectory in the co-moving frame, the radial velocity of the particle is proportional to the centrifugal velocity $r\Omega$. The proportionality factor is about the same as the one excepted for the lowest rotation. Note that the final position is not zero due to friction and seems to depend more on the details of the experiment (initial condition, the friction rugosity etc...) than on the rotation

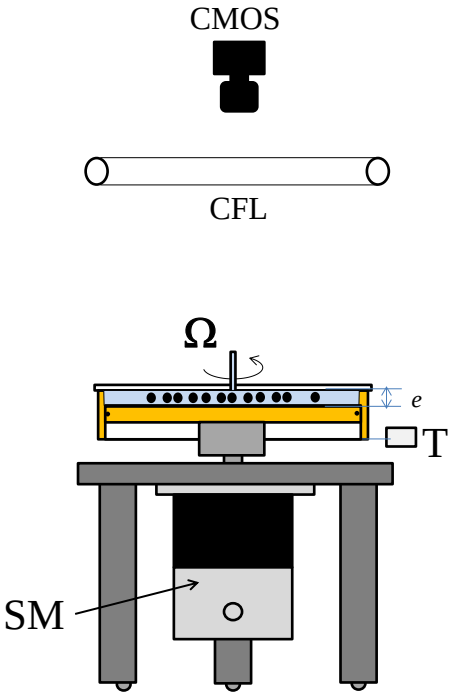

Figure 3.1: Experimental device: A cylindrical closed container, filled with water and polypropylene spherical particles of d=2 or 2.5 mm diameter, rotates around the vertical axis. The gap is maintained smaller than 2d. The motion is driven by the steep motor (SM) and controlled by the tachymeter (T). The radial position, r, of a polypropylene spherical particle (P) is followed by a camera and is enlighten by a circular fluorescent light (CFL).

rate. We checked that a larger particle made of the same material goes faster, as expected the proportionality of the centrifugal to the particle volume.

Final structure of a set of particles

Then we studied a set of identical particles. We mix particles (with a magnetized steel sphere and a magnet) in order to start with a homogeneous distribution. Then we rotate the cell. We study the stationary pattern obtained after a long time (of order of 900 turns although we check that we reached indeed a stationary state with very long measurements about a day). As shown in figure 3.3–c for a filling fraction of 0.5, at high rotation rate, the particles of 2mm diameter, quickly cluster in the center of the cell. It probably occurs during the transient regime. At low rotation rate, particles also cluster in the center of the cell, maybe because they have very slow motion and thus they have time to find a path to go to the center without jamming (see figure 3.3–a). However, in between, there is an intermediate range where particles jam into a stable dense ring as shown on the figure 3.3–b.

In order to quantify this effect, we compute the area filled by collapsed particles in a shell between a radius $R_1 = R/20$ and $R_2 = R/4$ around the center of the cell. We plot on the main

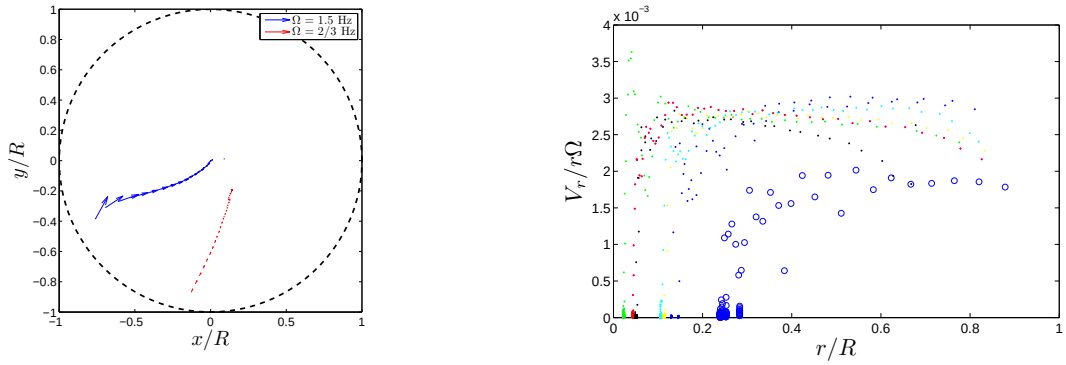

Figure 3.2: **Left**: Trajectories in the co-moving frame of a single particle of diameter $d = 2$ mm driven at a rotation rate of $\Omega = 2/3$Hz (red arrows) and 1.5 Hz (blue arrows). The arrows length is proportional to the velocity. **Right** The radial velocities of the particle normalized by the centrifugal velocity $r\Omega$ as the function of the radial position of the particle for rotation rates of $\Omega = 2/3$Hz (open blue circle) $\Omega = 1$Hz (blue points) $\Omega = 7/6$Hz (cyan points) $\Omega = 4/3$Hz (green points) $\Omega = 3/2$Hz (yellow) $\Omega = 5/3$Hz (magenta points), $\Omega = 11/6$Hz (red points, $\Omega = 2$Hz (black points).

panel of figure 3.3, the final minus the initial value of this area divided by the particle surface as a function of the rotation rate Ω. It exhibits a minimum near $\Omega = 0.3$ Hz for a filling fraction of 0.5. When the filling fraction is increased up to 0.6, this value is shifted to a larger v,alue of 0.43 Hz. With the 2.5 mm diameter particles, it seems to go on the other way (minimum at 0.4 Hz at a filling fraction of 0.5 and 0.3 Hz at 0.6).

Final remarks

We stopped this experiment after these first preliminary results because we broke (for the second time) the top glass plate (made of 5 mm glass plate with a home-made hole of 5mm in the center). Once replaced by a thicker plate, we were not able to reproduce these results. This could be due to a misalignment of the bottom and top plate, the change of the friction property or a small bending introduced in the two first thin plates by the home-made hole. To avoid the problem of the friction on the top plates, we decided to focus on the motion of a floating particles moving on the parabolic free surface of a fluid in solid rotation. Preliminary results are presented hereafter.

3.4.2 Motion of a floater on the free surface of a fluid in solid rotation

Motivations

To suppress the friction on the upper plate, we can consider the motion of floaters on the free surface of a fluid in solid rotation. Actually the problematic is quite different. Indeed the free surface of a liquid in solid rotation adopts a parabolic shape where gravity compensates the centrifugal force. In the stationary regime all points at the surface are motionless. Hence a floater receives a buoyancy force modified by centrifugal force and should be in equilibrium at any position of the free surface as long as the capillary forces are neglected. If we assume a

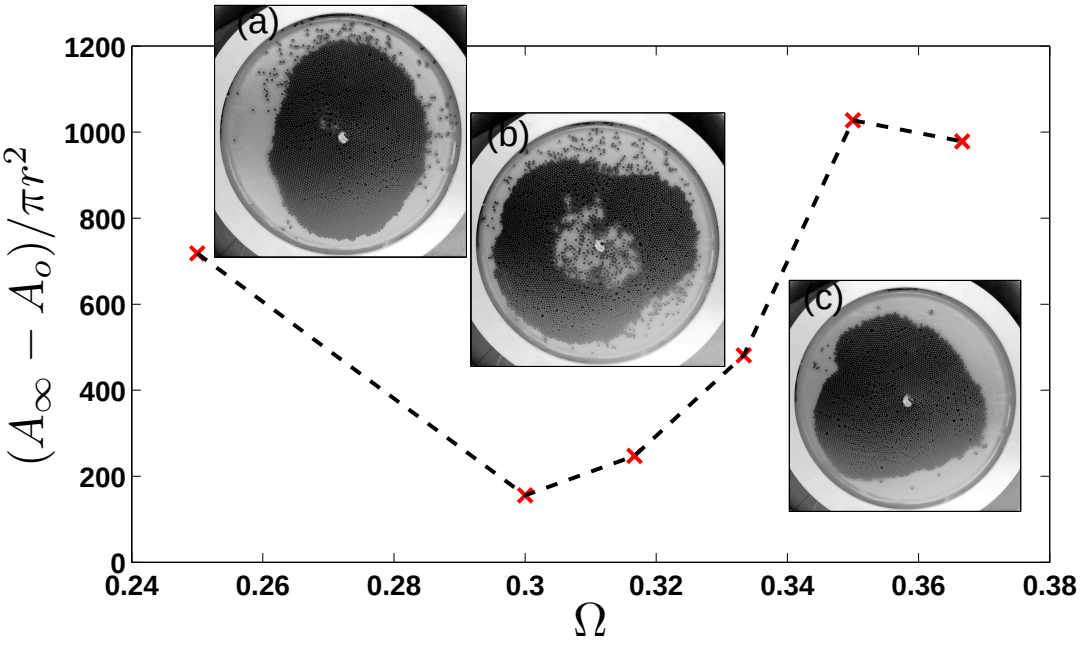

Figure 3.3: **Insets**: Final state of a monolayer of polypropylene particles of 2 mm diameter immersed in water with a filling fraction of 0.5, (a) with a rotation rate of 0.25 Hz, (b) with a rotation rate of 0.3 Hz, (c) 0.37 Hz. **Main panel** Number of particles in the circular shell included between the radius R/20 and R/4 as a function of the rotation rate Ω.

symmetrical meniscus around the particles, as the buoyancy is just corrected by the mass of liquid displaced by the meniscus, then a floater should be in mechanical equilibrium everywhere at the surface. However the meniscus might be deformed by the centrifugal force and may apply a radial force. If a motion occurs, the strength and even the direction of this resulting force are not obvious and this is even truer with its variations with the rotation rate, the wetting or the relative density of the sphere. We started to explore these phenomena with the device sketched in figure 3.4. This study has also some connections with the study of floaters moving on the surface of a turbulent flow presented in section 4.5.2 and in [74]. Indeed in this case, some of these effects could affect the motion of floaters experiencing the rotation of vertical vortex on deformed surface generated by a turbulent flow.

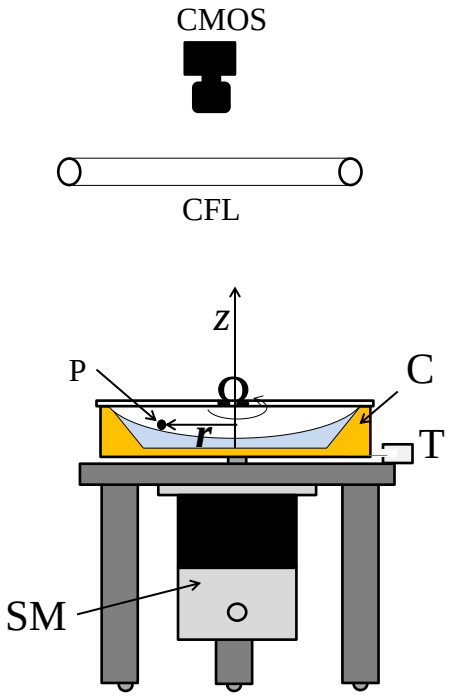

Figure 3.4: Experimental device: A cylindrical closed container (C) half-filled with water rotates around the vertical axis. The motion is driven by the steep motor (SM) and controlled by the tachymeter (T). The radial position, r, of a polypropylene spherical particle (P) of d=2 or 2.5 mm diameter and density 0.9 is followed by a camera and is enlighten by a circular fluorescent light (CFL).

Preliminary results

Preliminary and qualitative results have been obtained by Alexis Soulier and Romain Graziani during a one month training course. They mainly studied the motion of a single spherical particle of 2 or 2.5 mm diameter made of polypropylene lighter than water (density $\rho_s = 0.9$). These spheres are mainly partially wetted particles if not special procedures are followed. We changed

the wetting by addition of a wetting agent Ilford. Up to now, our studies were limited to two wetting cases (a partial wetting and an almost full wetting), but we do not know exactly yet the contact angle. Both water and the air over it are in solid rotation at the rate Ω. The particles are initially placed at a large radius. We study their motion at various rotation rates. We get the following results.

- *Pure water*: We studied first the motion of a sphere in pure deionized water. Figure 3.5–left shows the successive positions of a 2.5 mm sphere in rotating frame (the camera being synchronized with the rotation rate) at a rotation rate 0.5 Hz. Particle moves toward the center as confirmed by the radial position shown in figure 3.5–right. The motion is very slow (of order of a mm/s) and a static position is reached only after about 8h for a rotation rate 0.5Hz, as shown figure in 3.6 for the tangential and radial velocity. This phenomenology is recovered for all the explored rotation velocities running from 0.25 to 1Hz[2], except that the motion slows down when the rotation rate is smaller.

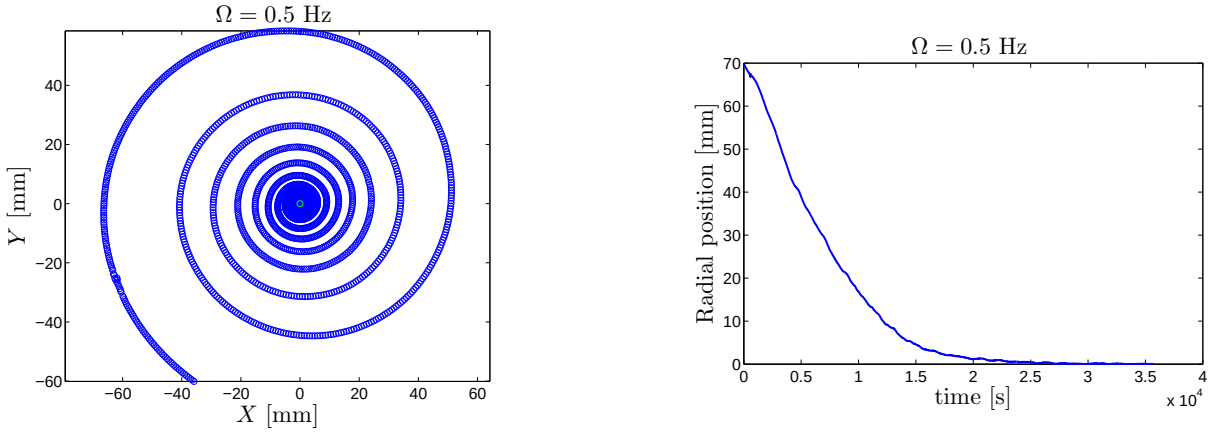

Figure 3.5: Particle position in the co-moving frame (left) and time evolution of the radial position (right) of a partially wetted particle in pure water, at a rotation rate of 0.5 Hz

- *For fully wetting particles*: When a wetting agent is added, the phenomenology seems to change. Indeed the particle reaches an equilibrium radius, at least at low rotation rate. This is illustrated in figure 3.7 where the particle position and the radial velocity are plotted for a rotation rate of 0.5 Hz. The oscillations visible at long time may be due to a small misalignment of the particles circular trajectory with the cell center. It could be induced by a slight shift of the cell axis. The log–log plot of the tangential velocity presented in figure 3.8–left seems to show a small residual velocity illustrating that the particle still moves in the rotating frame (as it seems to be the case also in figure 3.7–left). Hence the particle seems to keep a slight delay. Finally figure 3.8–right shows the final position of the particle as a function of the rotation rate. Clearly the equilibrium radius decreases with the rotation rate.

[2]The lower limit was fixed by our patience, the higher was fixed by the height of the cell

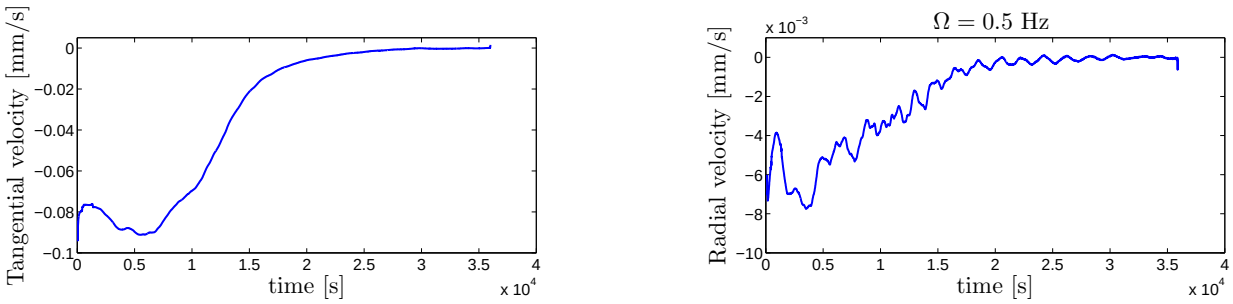

Figure 3.6: Tangential (left) and radial (right) velocities of a partially wetted particle in the co-moving frame, at a rotation rate of 0.5 Hz.

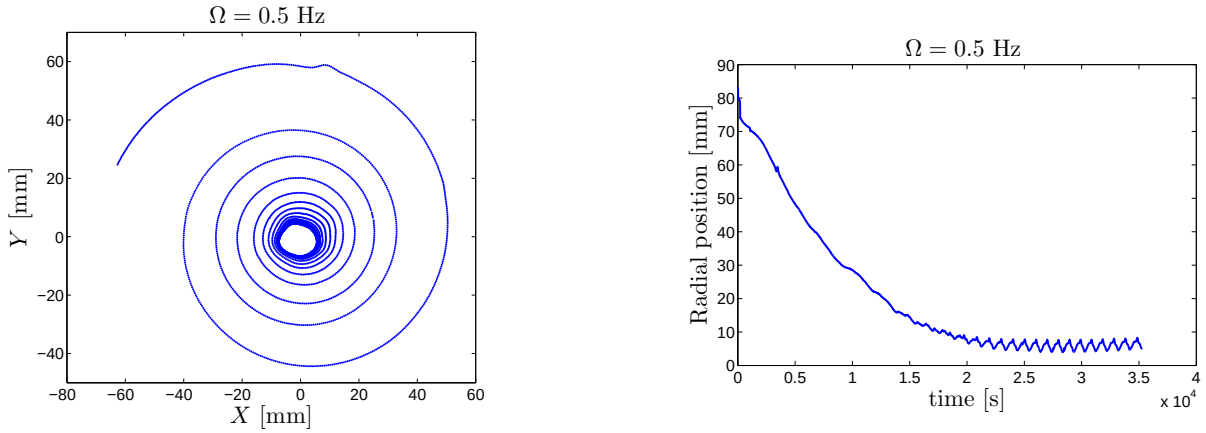

Figure 3.7: Particle position in the co-moving frame (left) and time evolution of the radial position (right) of a fully wetting particle, at a rotation rate of 0.5 Hz

Perspectives

The displacement of the particle can be understood by the force induced by the dissymmetric deformation of the meniscus due to the centrifugal force. However the stop of the particle at a finite radius is more puzzling. The meniscus deformation around the sphere could be weaker in fully wetting case than in the partially wetting case (it also depends on the buoyancy and on the position of the waterline) and the viscous drag may be larger for the more immersed particle. Therefore the radial force applied by the meniscus can be also weaker and viscous damping may be more efficient to stop the particles, since the immersed part is larger. To confirm these hypotheses, one has to check how the final equilibrium depends on the wetting and capillarity force, the relative density of the particle and its diameter or the fluid viscosity? To go further, we need more systematic measurements changing continuously the wetting. This implies that we are able to measure it. It will be interesting to estimate the meniscus in situ during the motion by synthetic Schlieren methods [75] for instance. We also need to perform measurement with particles of various densities (we did not try yet heavier non wetting particles for instance) and diameters. The next steps could be the study of the structure adopted by a set of floaters

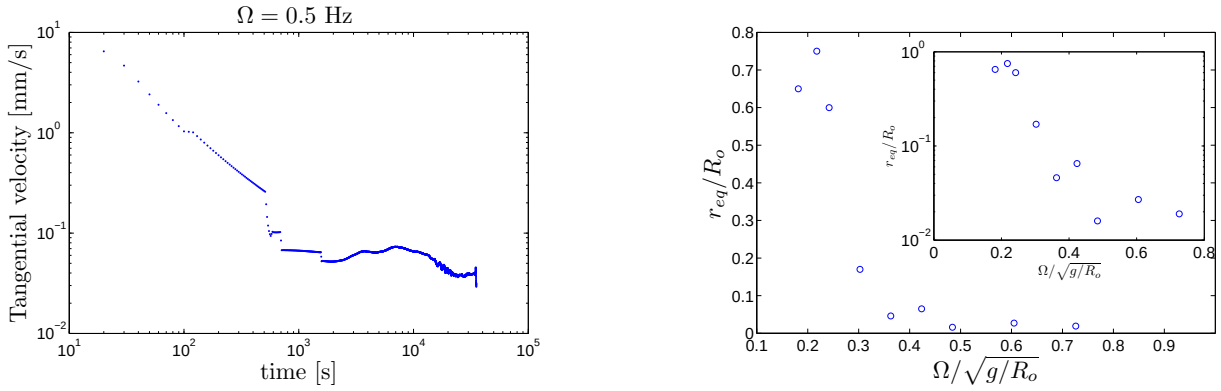

Figure 3.8: Tangential velocity of a fully wetting particle in the co-moving frame at a rotation rate of 0.5 Hz (left) and the final radial position of wetting particles as function of the rotation (right)

interacting by capillary force [76, 77]. In the context of floaters at the surface of a turbulent flow, one can also estimate the role of the shear applied by the upper fluid, by maintaining the cover plate fixed in the lab frame for instance.

3.4.3 Dynamics of a sphere on a parabolic support in solid rotation

- *Friction of spheres on rotating parabolic support [78]*

A. Soulier and S. Aumaître submitted to Am. J Phys. (2014)

Abstract: This pedagogical article illustrates the role of friction in the motion of a rolling sphere on parabolic support rotating around it axis. Indeed, we show that the rolling onset imposed by the static friction on the tangential forces gives a range of equilibrium positions at any rotation rate. In contrast, the frictionless case has finite equilibrium position at only one rotation rate where gravity and centrifugal force balance. This maximum equilibrium radius is measured experimentally and gives an estimate of the static friction of spheres made of different materials. Due to the particular choice of the support, some easy analytical calculations allow theoretical predictions either for the static position or for their stability. These predictions can be compared with experimental results. The stability analysis involving the rolling friction, the rolling friction coefficient is measured in the same device, by checking the dissipation during rolling.

3.5 Order–disorder transition in a layer of spheres vibrated vertically

Works in collaboration with :
Nicolas Mujica [1], Loreto Oyarte[1] Pablo Gutierrez–Matus[2] Cecile Gasquet–Wierthel[2], Vincent Padilla[2]

A horizontal monolayer of monodispere spheres, sandwiched between two plates spaced by less than 2 sphere diameters can be excited also in the bulk by vertical vibration. In the case of non-interacting hard spheres, a complex phase diagram involving two-layer clusters with different structures have been exhibited. In order to understand the transitions, we explore the mechanical and energetic balances between each phase. Dimensionless equations tend to show that a specific scaling for the vertical velocities is necessary to get the convenient time of collision with boundaries that allows to recover some of the experimental predictions. Then we considered the case of magnetized spheres interacting via a dipolar interaction. At high vibration, the medium is disordered. When the acceleration is adiabatically decreased a cluster is observed at a given threshold of the dimensionless acceleration. It is made of a monolayer structured in a triangular lattice. When the driving is increased again, a hysteretic behavior is observed and a higher threshold is necessary to reach the disordered state. Then we performed a quench of the system from the disordered state to the hysteretic region. After a transient in a metastable state, we studied in details the dynamics of the cluster growth.

3.5.1 Mechanical and energetic balances in a monolayer of inelastic spheres and phase transition

Introduction

At the end of the ninety's, J.S. Olafsen and J.S. Urbach [79] exhibited a typical out-of-equilibrium behavior of a monolayer of inelastic grains. They vibrated vertically a monolayer of spheres of diameter d, sandwiched between to plates with a gap, H such that spheres cannot overlap i.e. $1.5d < H < 2d$. By increasing the forcing, they revealed a surprising transition to a more ordered state involving a part of the grains. These clusters are formed by a bilayer of grains with crystal-like lattice (triangular or square) that nearly fits the gap. Although this transition shares similarities with usual phase transitions [80], the phase space is quite complex. Indeed it depends on many parameters (the amplitude and the frequency of the forcing, the gap, the filling fraction of the spheres, the restitution coefficient...) and it seems to be not clearly understood [81]. One of these features is that the driving amplitude threshold of the transition tends to become independent of the driving frequency when this frequency becomes large enough [81] (it is also

[1]universidad de Chile, Santiago, Chile
[2]Sphinx–SPEC CEA-Saclay, France

the regime in which gravity can be neglected. This is a minimal requirement that theoretical predictions must recover. Here we check if a careful energetic and mechanical budget between each phase can help to extract some information about the transition onset.

Energy and mechanical balance

For a single sphere of mass m and diameter d bouncing at the velocity v on a plate of infinite mass moving at the periodic velocity V_p with a restitution coefficient r, one can split the energy transferred during one collision ΔE into two terms:

$$\Delta E = m\left\{V_p(1+r)\left[V_p - v\right] - (1-r^2)\left[V_p - v\right]^2/2\right\} \tag{3.1}$$

where the first term on the rhs is the energy injected to the particle during the collision with the walls and the second term is the energy dissipated during this collision. Whereas the latter is always positive, the former can be either positive or negative. The different cases are depicted in figure 3.9. Indeed, as shown for the case C in figure 3.9, if Vp is negative (piston going down) and $v < V_p$ such that the collision occurs, then the particle restitutes energy to the piston. Actually for high restitution coefficient the speed of the particles becomes large such that $|v|/|V_p| >> 1$. Hence the probability of a negative energy input, where $V_p < 0,\ V_p - v \sim -v > 0$ (case C), becomes almost as probable than a positive energy input, where $V_p > 0,\ V_p - v \sim -v > 0$ (case A), whereas the case B in figure 3.9, where $V_p > 0, v > 0$ but $V_p - v > 0$ becomes very unlikely. Therefore the injection becomes less efficient when the dissipation is reduced. However, the limit $r \to 1$ is singular. A careful computation, assuming a Gaussian distribution of the sphere velocity decorrelated from the piston velocity, reduces the mean energy input to $m\langle V_n^2\rangle$ in this case [82].

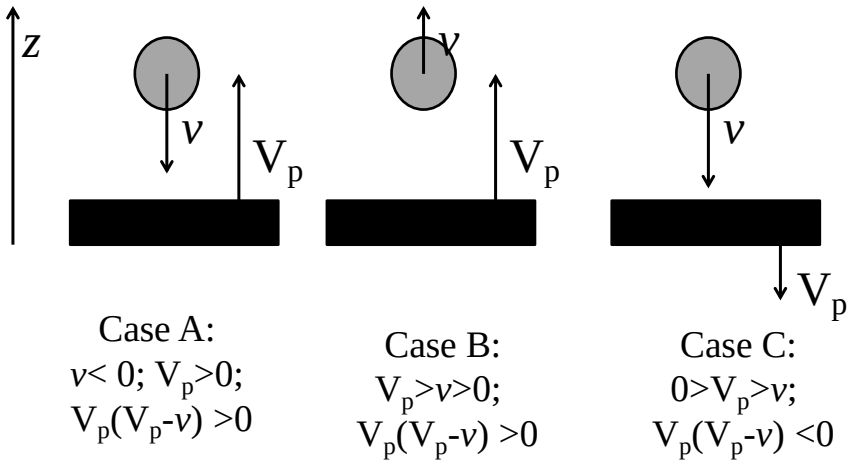

Figure 3.9: Sketch of the three types of vertical collisions between a moving wall of velocity V_p and a sphere of velocity v.

If we consider a single monolayer bouncing on the plate containing N_L particles, occupying of a surface S_L and moving with a horizontal rms velocity u, one can estimate the energy density or pressure, P_L in the layer as

$$P_L = m\frac{N_L}{S_L}u^2 \tag{3.2}$$

In a bilayer of N_s particles occupying a surface S_s having an rms horizontal velocity u' bouncing on a plate, the pressure takes the similar form:

$$P_S = m\frac{N_S}{S_S}u'^2 \tag{3.3}$$

The mechanical stability imposes an equality of the pressure in each phase, $P_L = P_S$ [3]. Moreover the total number of spheres, N, is fixed in the experiment $N = N_L + N_S$. Finally in the ordered bilayer phase, the occupied surface is fixed by the number of particles and the geometry of the order phase, one has $N_s = \alpha \cdot S_S$. In a prefect triangular lattice made of two layers, one gets $\alpha = 4/(\sqrt{3}d^2)$. Altogether, this links the horizontal rms velocity in each phase as follow:

$$u' = f(n)u \tag{3.4}$$

with $n = N_s/N < 1$, $f(n) = \sqrt{\frac{1-n}{\alpha/\rho_o - n}}$ where $\rho_o = N/S$ with $S = S_L + S_S$ the total surface of the cell [4].

Note that $\alpha/\rho_o > 1$ hence $f(n) \leq 1$. Figure 3.10 shows that $f(n)$ is a decreasing function of n. This relation can be checked experimentally. At least, it is known that $u \geq u'$.

If we try to estimate the injected power in each phase, starting from (3.1) one gets for the liquid phase:

$$I_L \sim mN_l\langle V_p(1+r)\left[V_p - v\right]\rangle\nu_L \tag{3.5}$$

where ν_L is the collision frequency in this liquid phase with the top and bottom confining plates and v is the vertical velocity in the monolayer. Similarly in the solid phase,

$$I_S = mN_S\langle V_p(1+r)\left[V_p - v'\right]\rangle\nu_S \tag{3.6}$$

where ν_s is the collision frequency in the ordered phase with the top and bottom confining plates and v' is the vertical rms velocity.

[3] Here, for simplicity, we neglected the excluded volume occupied by the spheres. However it can be taken into account by using the equation of state proposed by Carnahan and Starling based on accurate virial expansion $P_x = \frac{N_x}{S_x}mu_x^2\frac{1+y+y^2-y^3}{(1-y)^3}$ with $y = N_x a/(HS_x)$ where a is the excluded volume $a \sim 2\pi Hd^2/3$. This adds a relevant correction especially in the dense phase [83].

[4] Using the equation of state proposed by Carnahan and Starling in the dense phase where $N_S/S_s = \alpha$ one get a correctif factor to equation (3.4) of order unity. For $\alpha = 4/(\sqrt{3}d^2)$ one has $u' = 0.87f(n)u$. Using the Carnahan and Starling's equation in both phase states imlpy a silghly more complex relation between u and u' that do not differ qualitativelly from equation (3.4).

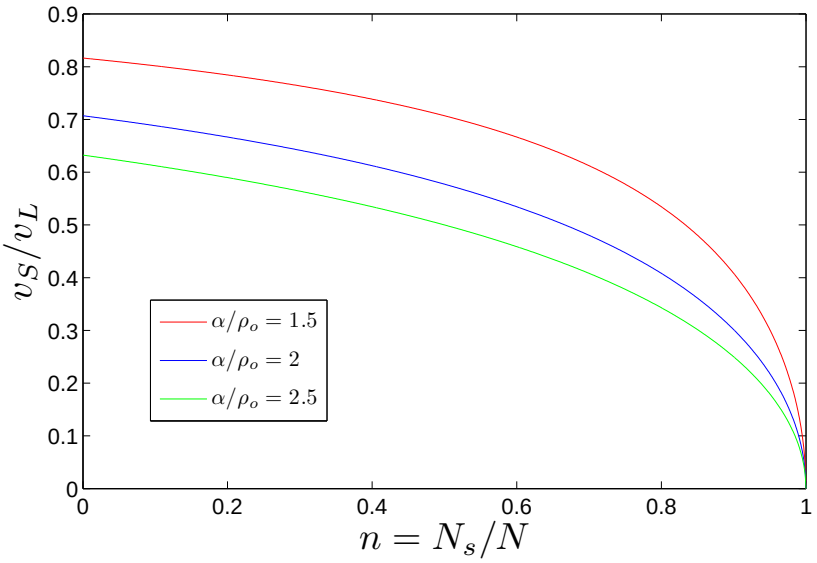

Figure 3.10: u'/u vs n for $\alpha/\rho_o d^2 = 1.5, 2, 2.5$

In the same way, one can try to estimate the dissipated power. In the disordered phase, because of the low particles density, one can assume that the main dissipation comes from the collisions with the top and bottom walls. Thus the mean dissipated power is given by

$$D_L = \frac{mN_L(1-r^2)}{2}\langle[V_p - v]^2\rangle\nu_L. \tag{3.7}$$

This assumption is not allowed in the ordered dense state where

$$D_S = \frac{mN_S(1-r^2)}{2}\langle[V_p - v']^2\rangle\nu_S + \frac{mN_S(1-r'^2)}{2}\langle u'^2\rangle\nu'_S \tag{3.8}$$

where ν'_S and r' are the collisions frequencies and the restitution coefficient between particles. When both phases are present, in the stationary regime one should have:

$$I_L + I_S = D_L + D_S \tag{3.9}$$

Dimensionless equation and relevant time scale

Hereafter we will restrict our study to the high frequency regime with particles having high restitution coefficients. In this case the only relevant time scale is the driving period. Moreover, one can expect that, in this low dissipative regime, the vertical velocities of the particles become larger than the piston velocities and that both velocities are uncorrelated. In this limit, one can

take: $\langle V_p\,[V_p - v]\rangle \sim \langle V_p^2\rangle$ in the injected power in both phases. For the dissipated power, one has to take $\langle [V_p - v]^2\rangle \sim \langle v^2\rangle$. The frequency collisions with the confining walls are given by the inverse of the free flight time: $\nu_L = v/h,\ \nu_s = v/h'$, with $h = H - d$ the mean free gap for the disordered particles between the top and bottom plates separated by a distance H and where $h' = H - \beta d$ is the mean free gap for the ordered particles. $1 < \beta < 2$ is a geometrical factor fixed by the ordered structure and thus it can be linked to α. The collision frequency between particles is linked to the mean free path in this phase and can be crudely estimated as: $\nu'_S = \alpha d u'$. Introducing the velocity scale $V_p = A\omega$, the time scale $1/\omega$ and the power scale $(1+r)mNVp^2\omega$, in equations (3.5–3.8), one gets the dimensionless set of equations

$$
\begin{aligned}
i_L &= (1-n)yA/h && (3.10)\\
i_S &= ny'A/h' && (3.11)\\
d_L &= (1-r)(1-n)y^3A/(2h) && (3.12)\\
d_s &= (1-r)n\left[y'^3A/h' + \tfrac{1-r'^2}{1-r^2}x'^3\alpha dA\right]/2 && (3.13)
\end{aligned}
$$

with $y = v/V_p,\ y' = v'/V_p$, and $x' = u'/V_p$. To go further, in addition to the power balance (3.9), we need a criterion allowing the cohesion of the ordered cluster.

Clusterization onset

In order to maintain its high density state, one can assume that the dense phase dissipates more than the disordered phase. Hence above the onset, one can assume $d_L|_c \leq d_S|_c$, with the equality reached at the onset. Therefore, due to (3.9) one gets also $i_L|_c + i_S|_c = 2d_l|_c$ at the onset. In the dense phase, where there are a lot of inter-particles collisions we may assume an isotropic velocities redistribution thus $x' \sim y'$. From these two equalities, one gets:

$$
\frac{(1-n_c)}{n_c}\frac{y_c^3}{y_c'^3} = \frac{h}{h'} + \frac{1-r'^2}{1-r^2}\alpha dh \tag{3.14}
$$

$$
1 + \frac{n_c}{(1-n_c)}\frac{y'_c}{y_c}\frac{h'}{h} = (1-r)y_c^2 \tag{3.15}
$$

From equations (3.14) one gets that

$$
\begin{aligned}
\frac{y_c}{y'_c} &= \left[\tfrac{n_c}{(1-n_c)}\left(\tfrac{h}{h'} + \tfrac{1-r'^2}{1-r^2}\alpha dh\right)\right]^{1/3} && (3.16)\\
&= 1/F(n_c, r, r', H, d, \rho_o, \alpha)
\end{aligned}
$$

And thus from (3.15) one gets:

$$y_c = \sqrt{\frac{1 + \frac{n_c}{(1-n_c)} F(n_c, r, r', H, d, \alpha) \frac{h'}{h}}{(1-r)}} \tag{3.17}$$

In any case, in order to get a threshold at a given amplitude whatever are the frequencies, one must not take $v \propto A\omega$. Indeed, otherwise the forcing disappears from (3.17) due to the natural choice of piston velocity as the single characteristic speed. An alternative is to assume that v is induced by the free flight of the particle in the gap after receiving a force $A\omega^2$ hence $v \propto \sqrt{Ah}\omega$ and thus

$$A_c = \frac{(1-r)(H-d)}{1 + \frac{n_c}{(1-n_c)} F(n_c, r, r', H, d, \alpha) \frac{h'}{h}} \tag{3.18}$$

Finally, one has still to determine the size of the ordered cluster appearing at the threshold. At least, a cluster is made of 4 particles, but with $n_c = 4/N << 1$, it seems impossible to satisfy $d_L|_c \leq d_S|_c$. If we believe this cohesive criterion, many small clusters or one macroscopic cluster have to grow at the onset [5]. In order to determine n_c, we need an additional relation between y and y'. Therefore, despite all the previous assumptions, we cannot go further without the missing link between the vertical velocity in each phase or, equivalently by using (3.4), the link between horizontal and vertical velocity in each phase. For the new assumptions that we have to do, one can follow different points of view

- We already assumed that $x' \sim y'$, one can also admit that $x \propto y$ (the equality seems not a reasonable hypothesis in the liquid phase where one expect $y > x$). Hence, one can write $y'_c/y_c = \gamma f(n_c)$, where $\gamma \leq 1$ is a proportionality constant between x and y. Together with (3.17), this gives n_c as a function of the control parameters. Surprisingly, n_c does not depend on the forcing parameters in the limit we choose. Within this hypothesis all the rms velocities are proportional to $\sqrt{Ah}\omega$. To be in the regime $v >> A\omega$ one has to keep $A << h$.

- We can adopt another point of view where all the horizontal velocities have the more usual scaling $u \propto A\omega$ in both phase. Hence, we have to put $x' \propto \sqrt{h'/A}y'$ in (13). Thus the ratio (3.17) explicitly depends on the driving amplitude as follow:

$$\frac{y_c}{y'_c} = \left[\frac{n_c}{(1-n_c)} \frac{h}{h'} \left(1 + \frac{1-r'^2}{1-r^2} \sqrt{\frac{A}{h'}} \alpha d A \right) \right]^{1/3} \tag{3.19}$$

  Therefore A_c is given by an implicit formula combining (3.19) with (3.15) and n_c should depend on the driving amplitude.

[5] In our crude modeling we do not distinguish dissipation in the bulk of the cluster from the one in the border. The latter should be less efficient; hence the large clusters should be promoted, as observed in experiments. A refined model should include these kinds of surface tension effects.

Order of magnitude and measurement perspectives.

To conclude, we can check if the estimated expressions for n_c and A_c are realistic. We follow the data of figure 6 of ref. [81]. The initial filling fraction, $\Phi_o = \rho_o \pi (d/2)^2$ (ratio of the surface occupied by the spheres over the total surface) is about 0.77. For $H = 1.75d$ i.e. $h = 0.75d$, they observed a bilayer cluster with a square lattice. Hence the filling fraction is about $\Phi_s = \alpha\pi(d/2)^2 = 1.57$ in the ordered phase, if one assumes that the spheres are perfectly compacted. It is probably not the case. Indeed the relative motion of the spheres and the vertical vibration should imply a looser lattice with lattice parameter $2d \geq a \geq d$. Therefore, $0.39 \leq \Phi_s = \pi d^2/(2a^2) \leq 1.57$. For the square lattice of parameter a, one gets $h' = H - d(1 + \sqrt{1 - a/(2d)})$ with a lower bound equal to $h' = 0.043d$ and an upper bound $h' = 0.75d$. Whereas the restitution coefficient between spheres, r', is stipulated, no information is given about the restitution coefficient, r, between the wall and particles. We will assume, $r = r' = 0.92$ or $r = r' = 0.77$. Assuming that the relation (3.4) holds for vertical velocity as well (i.e. $\gamma = 1$), and combining with (3.17), one can resolve n_c numerically (it does not depend on r or r' if $r = r'$). The result is shown figure 3.11. n_c evolves between 15% and 20% in the available range of the lattice parameter. This seems reasonable. From n_c, we can deduce A_c as a function of the lattice parameter. The value is shown in the inset of figure 3.11 for $r = 0.92$. It evolves around 0.05. For $r = 0.77$, it evolves around 0.15. It is not so far from the result of figure 6 of [81], considering the crude approximations, especially for the high restitution coefficient which is the most in framework of our model [6]. At least the condition $A_c << (H - d)$ is fulfilled. It has to be noticed that the denominator of (3.18) only slightly varies (between 1.21 and 1.18). Therefore A_c is mainly determined by the numerator $(1 - r)(H - d)$.

Although they are quite speculative, the previous analytical estimations give some guidelines for further measurements. This result should at least motivate more systematic measurements of the critical amplitude as a function of the initial density, the gap and the coefficient of restitution of the wall. Moreover many hypotheses can be checked experimentally. The mechanical equilibrium, (3.4), can be easily checked with a high speed camera. In the same way, one can estimate the link between vertical and horizontal velocity in each phase, although an accurate measurement of the vertical velocity in the narrow gap may be challenging. Such a measure will allow to check the quite speculative but essential expression $v \propto \sqrt{A(H - d)}\omega$. Pushed further, these kinds of arguments could also predict the structure of the crystal, considering for instance that the most dissipative one is the most stable.

3.5.2 Order–disorder transition in a layer of magnetized spheres vibrated verticallly

- *Phase transition in an out-of-equilibrium monolayer of dipolar vibrated grains [84]*

  L. Oyarte, P. Gutierrez, S. Aumaître and N. Mujica, Phys Rev E **87**-2 022204 (2013)

  Abstract: We report an experimental study on the transition between a disordered liquid-like state and an ordered solid-like one, in a collection of magnetically interacting macro-

[6] In figure 6 of [81] one has $A_c/d \sim 0.07$ for $r' = 0.92$, r is unknown. For $r' = 0.77$, A_c is 60% larger in our prediction than in experiment, but in both case, the threshold increases when r' decreases.

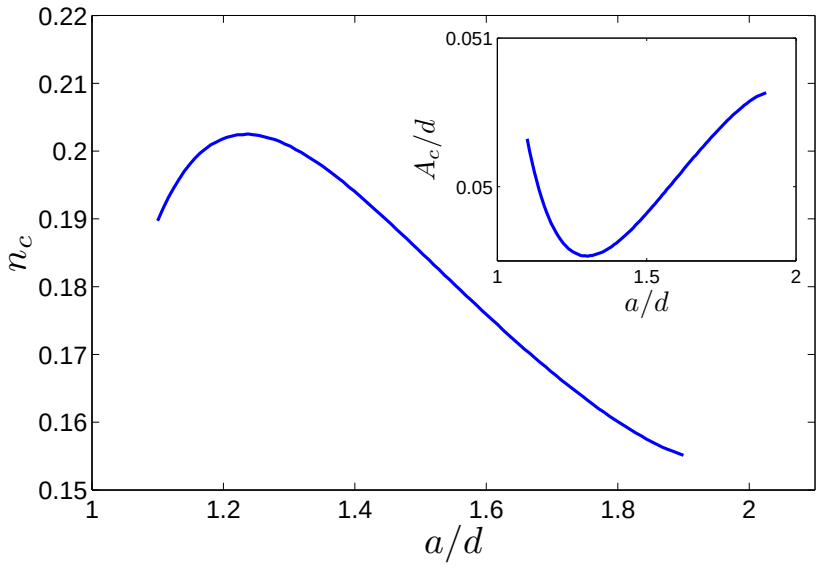

Figure 3.11: Relative number of spheres in the order phase, n_c as a function of the lattice parameter, a. The inset gives the critical amplitude, A_c, as a function of a for coefficients of restitution $r = r' = 0.92$.

scopic grains. A monolayer of magnetized particles is vibrated vertically at a moderate density. At high excitation, a disordered, liquid-like state is observed. When the driving dimensionless acceleration Γ is quasi-statically reduced, clusters of ordered grains grow below a critical value Γ_c. These clusters have a well defined hexagonal and compact structure. If the driving is subsequently increased, these clusters remain stable up to a higher critical value Γ_l. Thus, the solid-liquid transition exhibits a hysteresis cycle. However, the lower onset Γ_c is not well defined as it depends strongly on the acceleration ramp speed and also on the magnetic interaction strength. Metastability is observed when the driving is rapidly quenched from high acceleration, $\Gamma > \Gamma_l$, to a low final excitation Γ_q. After this quench, solid clusters nucleate after a time lag τ_o, either immediately ($\tau_o = 0$) or after some time lag ($\tau_o > 0$) that can vary from seconds up to several hundreds of seconds. The immediate growth occurs below a particular acceleration value Γ_s ($\leq \Gamma_c$). In all cases, for $t \geq \tau_o$ solid cluster's temporal growth can be phenomenologically described by a stretched exponential law. Finally, by taking into account the finite size of our system and by using simple assumptions we propose an alternative tractable theoretical model that reproduces cluster's growth, but which analytical form is not a stretched exponential law.

Chapter 4

Instabilities in Magnetohydrodynamics

4.1 Introduction

Magnetohydrodynamics describes the motion of a conducting fluid. Such flows are common in geophysics and astrophysics and in many industrial processes [85]. Magnetohydrodynamics combines the hydrodynamic equations for the velocity field and the induction equation for the magnetic field. It is used in the limit where the fluid velocity is small compared the speed of light c.Therefore the equation of Maxwell-Ampere:

$$\nabla \wedge \mathbf{B} = \mu_o \mathbf{J} + \frac{\mathbf{1}}{\mathbf{c^2}} \partial_\mathbf{t} \mathbf{E} \tag{4.1}$$

reduces to

$$\nabla \wedge \mathbf{B} \approx \mu_o \mathbf{J} \tag{4.2}$$

where $\mathbf{B}$ is the magnetic field, $\mathbf{J}$ is the electrical current density, $\mathbf{E}$ is the electric field and $\mu_o = 4\pi \cdot 10^{-7}$ is the magnetic permeability of vaccum. Moreover, one has to be in a limit where the Ohm's law holds:

$$\mathbf{J} \approx \sigma(\mathbf{E} + \mathbf{v} \wedge \mathbf{B}) \tag{4.3}$$

where σ is a constant and uniform electrical conductivity. To be able to define such transport coefficient, one needs a collision frequency of the charges, f_c, much larger than the typical frequency of the turbulent flow. Therefore, the electrical conductivity is of order of $\sigma \sim ne^2/(mf_c)$, where n is the charge density and e is the elementary charge. Finally the charges trajectory must not be modified by the magnetic field to prevent magneto-resitive effects. Therefore, the collision frequency has to be larger than the Larmor frequency of the charge : eB/m. These approximations are completely justified in liquid metal but problems can occur in rarified plasma[86]. Taking the curl of (4.3) together with the Maxwell-Faraday equation: $\nabla \wedge \mathbf{E} = -\partial_t \mathbf{B}$, one gets the induction equation. It can be written in a dimensionless form as:

$$\partial_t \mathbf{B} + (\mathbf{v}\nabla)\mathbf{B} = (\mathbf{B}\nabla)\mathbf{v} + \frac{1}{Re_m} \Delta \mathbf{B}. \tag{4.4}$$

The feedback of the magnetic field on the fluid velocity occurs via the Lorentz force. The Navier-Stockes equation is traditionally written in dimensionless form as:

$$\partial_t \mathbf{v} + (\mathbf{v}\nabla)\mathbf{v} = -\nabla p + \frac{N}{Re_m}(\nabla \wedge \mathbf{B}) \wedge \mathbf{B}) + \frac{1}{Re}\Delta \mathbf{v} \tag{4.5}$$

where we used the characteristic length L, the characteristic velocity U_o and the characteristic magnetic field B_o. The three dimensionless parameters are the Reynolds number $Re = U_o \cdot L/\nu$, the magnetic Reynolds number $Re_m = \mu_o \sigma U_o \cdot L$ and the interaction or Stuart number $N = \sigma B_o^2 L/(\rho U_o)$, where ν is the fluid viscosity.

The magnetic Reynolds number estimates the advection of the magnetic field lines by the flow compared to their diffusivity. When it is very small, the magnetic field is almost unchanged by the velocity field. The value of the magnetic diffusivity $1/\sigma\mu_o$ is usually very large (compared to the kinematic viscosity) in the liquid metals[1]. Therefore most of the laboratory experiments driven by electric currents and magnetic fields are in the low Re_m limit. However, it does not mean that no induction phenomena occurs. Indeed a strong applied magnetic field can induce some currents in good conducting fluid, but the magnetic field generated by this current will remain small compared to the applied one. These induction phenomena explain the concentration of the current in a thin boundary layer close to the wall where the induced currents, opposed to applied ones, vanish due to the no slip boundary conditions. It has to be taken into account when electromagnetic forcing is used to stir the fluid. Indeed, in a good conducting fluid with high magnetic field, the forcing occurs only in a thin Hartmann boundary layer of depth $e_H = \sqrt{\rho\nu/\sigma}/B_o$, near the walls and not in the bulk. This low Re_m limit will be adapted to describe the experiments presented in section 4.3–4.5.

In the high Re_m limit, the magnetic field lines almost follow the flow. An important condition to reach the dynamo action, i.e. the self–generation of a magnetic field by the motion of a conducting fluid, is to get an advection strong enough to overcome the diffusion of the magnetic field, hence $Re_m > 1$. In all liquid metals $Re_m/Re << 1$ therefore the flow has to be turbulent. The role of turbulence on dynamo action was one of the main aims of the experiment VKS presented in the next section

[1]For liquid Sodium, one gets, at 100 C, a magnetic diffusivity about 0.08 and a kinematic viscosity about 7.3×10^{-7}. Their ratio, called the magnetic Prantdl number, is small $\nu\mu_o\sigma \sim 10^{-5}$.

4.2 Magnetic field generation and its dynamics in an unconstrained liquid metal flow : The VKS experiment.

Works in collaboration with the VKS-collaboration[0]*:* Jean Boisson[1], Bérengère Dubrulle[1], François Daviaud[1], Cecile Gasquet–Wierthel[1], Vincent Padilla[1] Sophie Miralles[2], Nicolas Bonnefoy[2,4] Nicolas Plihon[2], Phillippe Odier[2], Jean–François Pinton[2], Mickael Bourgoin[2,5] Gauthier Verhille[2,6] Johann Hérault[3], François Pétrélis[3], Stéphan Fauve[3], André Skiara[4],

When the advection of the magnetic field lines in an electrically conducting fluid is large enough, i.e. when $Re_m > 1$, then self-generation of a magnetic field can occur. Such dynamo instability is assumed to be at the origin of most of the magnetic fields of the universe. For instance the Earth magnetic field is generated by the convective motion of the molten iron in the liquid core. In such cases, where liquid metals are concerned, the magnetic Prandtl number $Pr_m = Re_m/Re = \mu_o \sigma \nu$, involving only the fluid properties, is intrinsically small (of order 10^{-5}), therefore the dynamo instability grows always from a turbulent flow. In order to reduce the amount of power necessary to reach the onset, all dynamo experiments are performed in liquid sodium because of its high conductivity and its low fusion temperature (97.8^o C). A high magnetic Reynolds number is a necessary but not sufficient condition to get a self-sustained dynamo in a conducting fluid. In addition, it necessitates usually a two steps process to generate the suitable induced currents that enhance the magnetic perturbation. The first experimental dynamos were based on very constrained flows inspired by theoretical configurations known to generate dynamo action [87, 88].
The aim of the VKS experiment was to achieve dynamo action in an unconstrained flow in order to get a better understanding of the role of the turbulent fluctuations on the instability mechanism. In this experiment where the liquid sodium is mainly stirred in a cylindrical vessel by two counter–rotating impellers , the dynamo was reached, after ten years of optimization, in September 2006, hence three months before my arrival into the team [89, 90, 91, 92] ! The first unexpected observation was the growth of a magnetic field that is, in average, mainly an axial dipolar magnetic field. Actually, it demonstrates that the magnetic field cannot be generated only by the mean flow.

[0]We only mention here the members of the collaboration currently present in the team, but the experiment has involved many more persons

[1]Sphinx–SPEC CEA-Saclay, France
[2]Laboratoire de Physique, ENS–Lyon, France
[5]LEGI, Université J. Fourier Grenoble I, France
[6]IRPHE, Université Aix–Marseilles I, France
[3]Laboratoire de Physique Statistique, ENS, France
[4]SSS, CEA–Cadarache, France

Indeed the cinematic numerical simulations, based on the mean flow, predicted an equatorial dipole. These numerical predictions were in agreement with the Cowling's anti-dynamo theorem that forbids an axial magnetic field generated by a flow possessing an axial symmetry. The ENS team proposed a mechanism involving the helicity generated at the trailing edge of the impeller's blades to explain the axial magnetic field [93]. Although this mechanism was confirmed by numerical simulation, it does not explain completely one important feature of the VKS-dynamo: the dynamo is observed only with full iron impellers with high magnetic permeability. Steel impellers with iron boundaries at rest, mixed impellers (iron blades and steel disks or steel blades and iron disks, etc...) do not generate dynamo action. A better understanding of the role of this boundary condition is still lacking, and a dynamo action in an unconstrained flow without (moving) iron is the next experimental challenge. Since 2006, in addition to the magnetic boundary conditions of the moving impellers, some experiments were performed to check the role of some others implemented optimizations in the first stages of the VKS experiment. In contrast to full iron impeller, the shape of the blades, lateral boundary conditions, a inner ring in the mid–plane, are shown to be not absolutely necessary to reach the dynamo onset, although they modify the dynamo threshold.
The second surprise of the experiments performed in 2006 comes from the observation of numerous dynamical regimes of the magnetic field when the impellers velocities were mismatched [90, 94, 95, 96]. In all configurations which generate a magnetic field, we studied extensively these dynamical regimes. Almost all of them : erratic reversals [90, 94], oscillations [94, 97], bursts [95, 96], bi-stability between a stationary and an oscillatory dynamo [97] as well as magnetic field localization [98], can be understood within the framework of the dynamical model proposed by F. Pétrélis and S. Fauve involving the interaction of two modes with a dipolar and a quadrupolar geometry, taking into account the symmetries of the experiment and mimicking the turbulent fluctuations by random noise [99].

I remind hereafter, the articles of the VKS collaboration where my contribution has been significant, i.e. by doing more than preparing and participating to the experimental runs, performing few data analysis and reading back manuscript. Most of the publications on the VKS experiment can be found in the bibliography

- *Chaotic Dynamos Generated by a Turbulent Flow of Liquid Sodium [94]* F. Ravelet, M. Berhanu, R. Monchaux, S. Aumaître, A. Chiffaudel, F. Daviaud, B. Dubrulle, M. Bourgoin, Ph. Odier, N. Plihon, J.-F. Pinton, R. Volk, S. Fauve, N. Mordant, and F. Pétrélis, Phys. Rev. Lett. **101** 074502 (2008)

  Abstract: We report the observation of several dynamical regimes of the magnetic field generated by a turbulent flow of liquid sodium (VKS experiment). Stationary dynamos, transitions to relaxation cycles or to intermittent bursts, and random field reversals occur in a fairly small range of parameters. Large scale dynamics of the magnetic field result from the interactions of a few modes. The low dimensional nature of these dynamics is not smeared out by the very strong turbulence of the flow.

Here I contributed to the figure 3, although the preliminary plot was slightly different (the final version is due to François Pétrélis, I think). I hope, it helped a little Stephan Fauve and François Pétrélis to build or confirm their model of the dynamics of the magnetic field.

- *Bistability between a stationary and an oscillatory dynamo in a turbulent flow of liquid sodium [97]*
  M. Berhanu, B. Gallet, R. Monchaux, M. Bourgoin, Ph Odier, J.-F. Pinton, N. Plihon, R. Volk, S. Fauve, N. Mordant, F. Pétrélis, S. Aumaître, A. Chiffaudel, F. Daviaud, B. Dubrulle and F. Ravelet, J. Fluid Mech. **641** pp 217–226

Abstract: We report the first experimental observation of a bistable dynamo regime. A turbulent flow of liquid sodium is generated between two disks in the von Kármán geometry (VKS experiment). When one disk is kept at rest, bistability is observed between a stationary and an oscillatory magnetic field. The stationary and oscillatory branches occur in the vicinity of a codimension-two bifurcation that results from the coupling between two modes of magnetic field. We present an experimental study of the two regimes and study in detail the region of bistability that we understand in terms of dynamical system theory. Despite the very turbulent nature of the flow, the bifurcations of the magnetic field are correctly described by a low-dimensional model. In addition, the different regimes are robust; i.e. turbulent fluctuations do not drive any transition between the oscillatory and stationary states in the region of bistability.

Here, with François Pétrélis and André Skiara, I performed most of the measurements presented in the article. I contributed also to the outline and to the plot of most of the graphs of the first draft of the paper, mainly written by François Pétrélis. The last version benefited also of improvements provided by the model managed by Basile Gallet.

4.3 Turbulent convection of a liquid metal with a horizontal magnetic field

Works in collaboration with :
Stephan Fauve[1], François Pétrélis[1], Students[1]

This part is mainly due to the work of François Pétrélis. I initiated the study but he performed most of the measurements and he wrote the report hereafter. We present the obtained results here, because they would have been probably lost otherwise.

[1]LPS, École Normale Supérieure, Paris, France

Turbulent convection is an old but still puzzling problem. One of the major questions is to understand the role of the turbulent advection versus the large scale mean flow in the heat transport efficiency. This is especially important to understand the ultimate regime (if it exists) where the transport is dominated by turbulent advection. Some studies that try to reduce the large scale mean flow, did not notice any substantial changes in the mean heat transport. Here we use a magnetic field to reduce fluctuations. More precisely, we study the effect of a horizontally applied magnetic field on the turbulent properties of a liquid metal driven by thermal convection. We show that the averaged heat-flux is not modified by a magnetic field until $0.11\,T$. This contrasts with the turbulent temperature fluctuations that are strongly reduced, up to a factor 2/3 in our experiment. This last phenomenon is controlled by a dimensionless parameter that compares the buoyancy force to the Lorentz force.

4.3.1 Introduction

It has been known for a long time that the main global effect of turbulence is to increase transport properties of momentum, heat, etc., but predicting effective transport coefficients (viscosity, heat diffusivity, etc.) is still a basic open problem of turbulence. A lot of theoretical tools have been used in order to model the effect of small scale turbulent fluctuations on transport coefficients but predicting from the governing equations the drag on an object moving in a turbulent flow or the heat transported by turbulent convection are unsolved problems. A large amount of data exists for the mean heat transfer by turbulent convection between two horizontal boundaries (Rayleigh-Bénard geometry). Depending on the parameter range, they are more or less roughly described by asymptotic laws mainly derived using dimensional arguments [100, 101]. In all experiments, the heat flux fluctuates in time around its mean value because the spatial average of local fluctuations does not vanish. This is not taken into account in theoretical models and has been studied experimentally only recently [102]. The aim of this work is to study the effect of small scale turbulent fluctuations on the mean heat transfer. This can be achieved by applying an external magnetic field to a convective flow of a liquid metal.

The effect of an external magnetic field on the Rayleigh-Bénard instability onset has been studied by Chandrasekhar [103]. Its main effect is to inhibit velocity gradients along its axis. Consequently, the instability onset is delayed when the field is vertical whereas it is unchanged for convection rolls parallel to the field axis regardless of lateral boundaries effects. A horizontal magnetic field does not affect these two-dimensional motions but inhibits three-dimensional secondary instabilities of the convection rolls [104, 105]. We thus use an external horizontal magnetic field to change the amount of turbulent fluctuations without modifying the large scale two-dimensional flow. We observe that the mean heat-flux is not modified within less that 3% when three-dimensional turbulent fluctuations are suppressed to 67% of their initial value by increasing the applied field.

4.3.2 Experimental set-up and measurements

The experimental set-up consists of a cubic container, $d = 90$ mm in length. The upper and lower boundaries are copper blocks. The temperature of the upper one is kept constant up to 10^{-2} C with a regulated water circulation. The lower block is heated with a constant electric current. The temperature difference ΔT is measured with platinum resistors glued in the lower and upper copper blocks. The lateral boundaries are made of PMMA and thus are electrically insulating. The working fluid is mercury. The Prandtl number, $Pr = \nu/\kappa$, where ν is the kinematic viscosity and κ is the heat diffusivity, is $Pr \simeq 0.026$ at working temperatures. Local temperature fluctuations are measured with thermistors glued flush with the boundaries. The heat flux per unit surface, q, is measured with flux-sensors Omega HFS-3. They consist of series of 100 thermocouples mounted across a thin layer of kapton, 0.23 mm thick and with a known heat conductivity, 0.3 W/m.C. Their response time is 0.6 s.

An electromagnet provides a roughly uniform horizontal magnetic field; the strength of the field B can be varied up to $B = 0.11\,T$. The magnetic Prandtl number $P_m = \mu_0 \sigma \nu$, where μ_0 is the vacuum magnetic diffusivity and σ the liquid metal electric conductivity, is $P_m = 1.48\,10^{-7}$ for mercury at working temperature. We reach Rayleigh numbers $Ra = \frac{g\alpha d^3 \Delta T}{\nu\kappa}$ of $3\,10^7$. The corresponding typical flow velocity v estimated by a balance between inertia and buoyancy is $v \simeq 4\,cm\,s^{-1}$ resulting in a maximum Reynolds number $Re = v\,d/\nu \simeq 3\,10^4$ and a magnetic Reynolds number $R_m = v\,d\,\mu_0\,\sigma = 4.5\,10^{-3}$.

4.3.3 Effect of a horizontal magnetic field on the mean convective heat flux

We first study the effect of the magnetic field on the mean heat flux $\langle q \rangle$. To wit we plot in figure 4.1 the Nusselt number, $Nu = \langle q \rangle d/(\kappa \Delta T)$, *i. e.* the convective heat flux normalized by the heat flux that would exist in the absence of convection for the same ΔT. It appears clearly that the magnetic field has very little effect on the mean heat flux, smaller than 3% for the highest values of the Rayleigh number. In other word a horizontally applied magnetic field, up to $0.11T$, does not modify the average flux of energy in our turbulent convective volume.

4.3.4 Standard deviation of the temperature fluctuations

We now turn to the fluctuations of temperature and first study the fluctuations at the surface of the lower plate T_{cb}. In figure 4.2, we plot the standard deviations of T_{cb} as a function of the applied temperature difference for various magnetic fields. For a fixed magnetic field, the temperature fluctuations are increasing functions of the applied temperature gradient. At fixed temperature gradient, the fluctuations are strongly decreased by the magnetic field.

To identify the dimensionless parameter that controls the reduction of temperature fluctuations, we plot in figure 4.3 the temperature fluctuations normalized by the temperature difference as a function of the dimensionless parameter Lj defined by

$$Lj = \frac{\sigma B^2}{\rho} \sqrt{\frac{d}{\alpha g \Delta T}}\,. \tag{4.6}$$

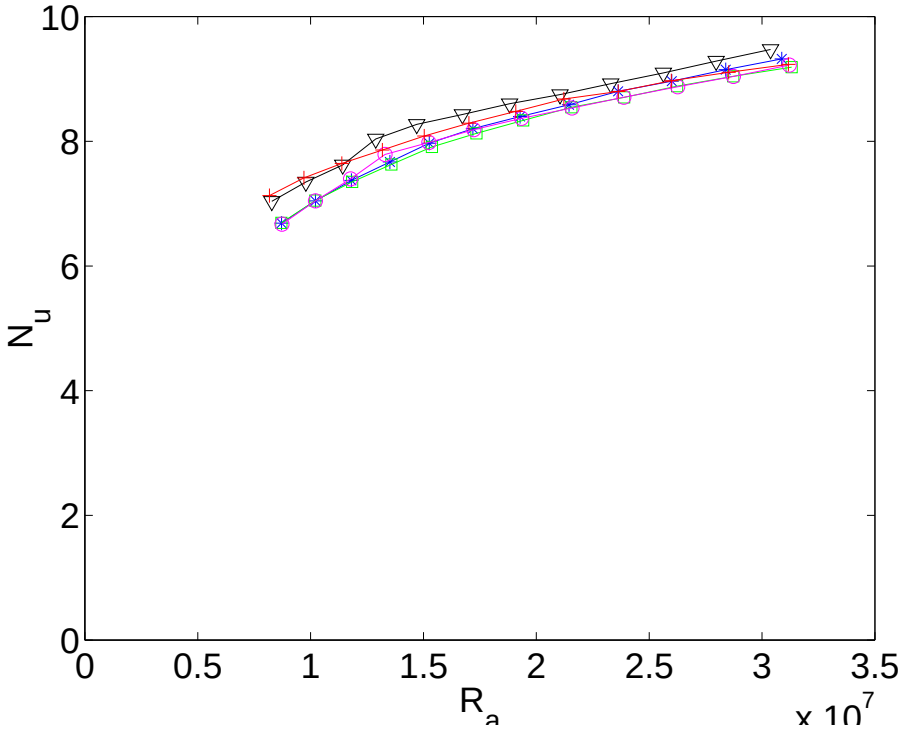

Figure 4.1: Nusselt number as a function of the Rayleigh number for an applied magnetic field of ($\bigtriangledown$) : $B = 0\,G$; ($\star$) : $B = 328\,G$; ($\square$): $B = 655\,G$; ($\circ$) : $B = 874\,G$; ($+$): $B = 1092\,G$. The colored lines are guide for the eyes.

This parameter is the ratio between the Lorentz force and the buoyancy force if the magnetic Reynolds number R_m is small so that the field induced by the flow is proportional to $R_m\,B$

The important parameters for this problem are ΔT, $\alpha \Delta T g$, ν, κ, ρ, σ, μ_0, B and d resulting in four dimensionless numbers. Therefore, the temperature fluctuation $std(T_{cb})$ follows a law of the form

$$\frac{std(T_{cb})}{\Delta T} = f\left(Lj = \frac{\sigma B^2}{\rho}\sqrt{\frac{d}{\alpha g \Delta T}},\, P_m,\, Pr,\, Ra\right) . \tag{4.7}$$

In the range of our measurements, the unknown function is a function of Lj only and does not depend on P_m, Pr and Ra. This can be understood the following way. If the flow is highly turbulent ($Re \gg 1$), one expects that the transport of impulsion, resp. of heat, is not controlled by the molecular viscosity ν, resp. the thermal conductivity κ. Therefore these two numbers can not appear in eq.(4.7). Moreover, if the magnetic Reynolds number R_m is small, one expects that the magnetic field induced by the flow is proportional to R_m. Thus, the Lorentz force is proportional to σB^2 which is the pertinent parameter instead of σ and B. Under these assumptions, there are

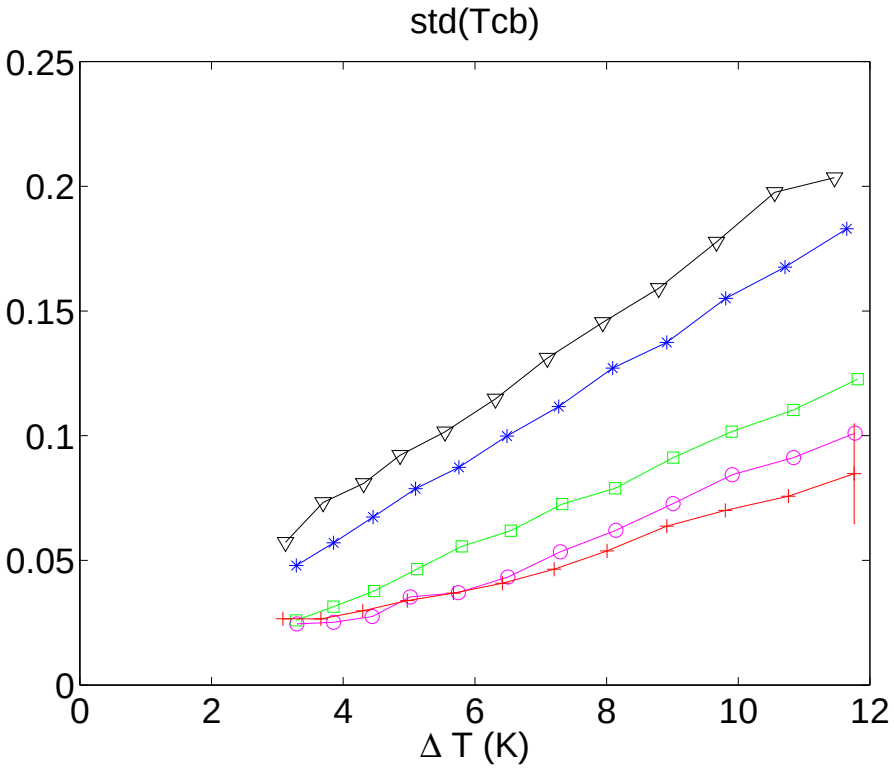

Figure 4.2: R.m.s. fluctuations of the temperature at the surface of the bottom layer T_{cb} as a function of the applied temperature difference ΔT for an horizontal magnetic field of ($\bigtriangledown$) : $B = 0\,G$; ($\star$) : $B = 328\,G$; ($\square$): $B = 655\,G$; ($\circ$) : $B = 874\,G$; (+): $B = 1092\,G$. The colored lines are guide for the eyes.

three less parameters in the dimensional analysis and the unknown function f is a function of Lj only.

4.3.5 Power spectra density of the temperature fluctuations

Applying a magnetic field reduces the temperature fluctuations. It is important to identify if this reduction amounts to globally lower the intensity of the power spectrum density (PSD) of the fluctuations or if only part of the spectrum is modified. To wit, we calculate the PDF of T_{cb} and plot it in fig 4.4. All the spectral components of the fluctuations are reduced when applying a magnetic field. At the highest value of the magnetic field, the frequency components between $0.02\,Hz$ and $0.2\,Hz$ are more decreased than the higher frequencies between $0.2\,Hz$ and $1\,Hz$. This may be related to the appearance of a low frequency peak in the spectrum around $0.02\,Hz$ for the highest magnetic field.

The presented temperature measurements are located at the bottom of the convective layer.

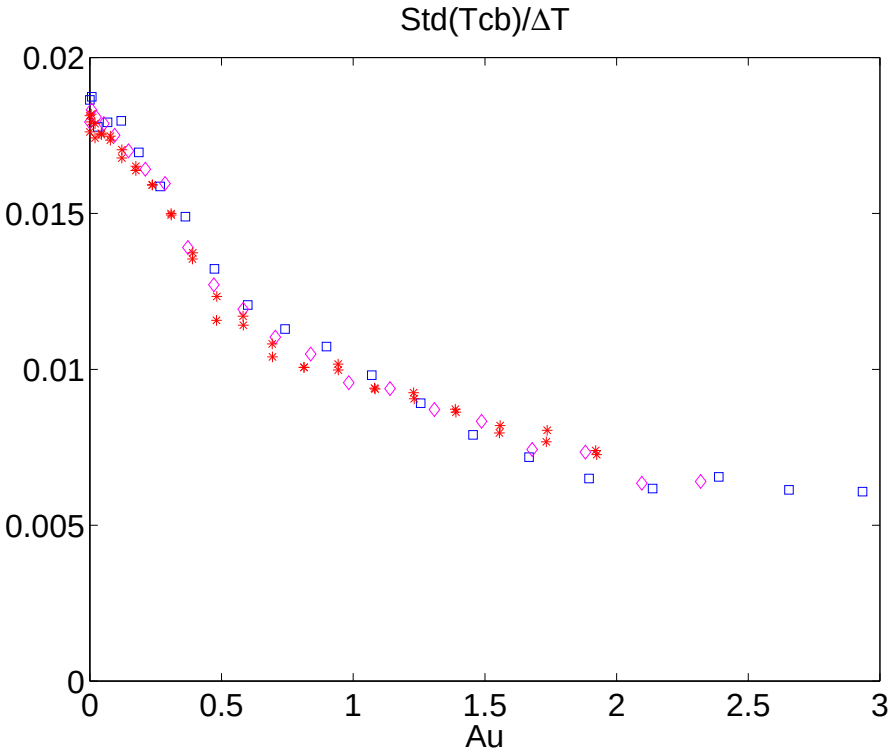

Figure 4.3: R.m.s. fluctuations of the temperature at the surface of the bottom layer T_{cb} divided by the temperature difference ΔT as a function of Lj for various temperature differences ($\square$): $\Delta T = 5\,K$; ($\diamond$) : $\Delta T = 8\,K$; ($\star$): $\Delta T = 11.6\,K$.

We also measured the temperature fluctuations at the lateral boundary. There again, applying a magnetic field reduces the amplitude of the PSD of the fluctuations but one peak appears in the spectrum for some values of the magnetic field and temperature difference. The amplitude of this peak can be large so that the r.m.s. fluctuations of the temperature can increase. This is due to the appearance of a periodic fluctuation but the level of turbulent fluctuations (the part of the spectrum out of the peak) is reduced when applying a magnetic field. Some PSD of the temperature T_l measured at a lateral boundary are presented in figure (4.5).

4.3.6 Conclusions

We have studied the effect of a horizontally applied magnetic field on a turbulent convective layer of liquid metal. On the one hand, the mean heat flux is not sensitive to a magnetic field up to $0.11\,T$; on the other hand, the temperature fluctuations are strongly reduced for such magnetic field. A possible mechanism is that the magnetic field acts mostly at the small scale of the velocity field, *i.e.* at the higher frequencies. The reduction of these components lowers the temperature

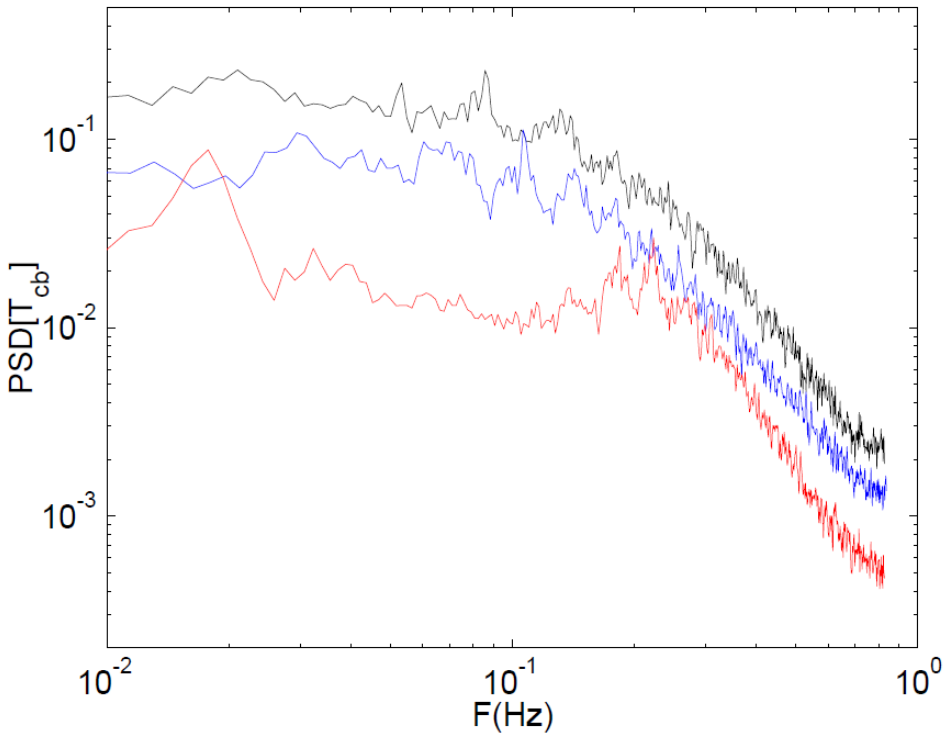

Figure 4.4: Power spectrum density of the temperature fluctuations at the surface of the bottom layer T_{cb} for fixed imposed temperature difference $\Delta T = 11.6K$ and various magnetic fields, from the upper curve to the lower curve $B = 0\ G$ (in black); $B = 546\,G$ (in blue); $B = 1092\,G$ (in red).

fluctuations but does not modify the mean heat flux that is dominated by the larger scales of the flow.

In the regime of large Rayleigh numbers, large Reynolds number and small magnetic Reynolds number, the reduction of the temperature fluctuations at the lower boundary depends only on Lj a dimensionless number that compares the Lorentz force and the buoyancy force.

4.4 Wave and instabilities in electromagnetically driven flow in cylindrical geometry

Works in collaboration

Jean Boisson[1], Andreï Klochko[1], François Daviaud[1], Cecile Gasquet–Wierthel[1], Vincent Padilla[1]

[1]Sphinx–SPEC CEA-Saclay, France

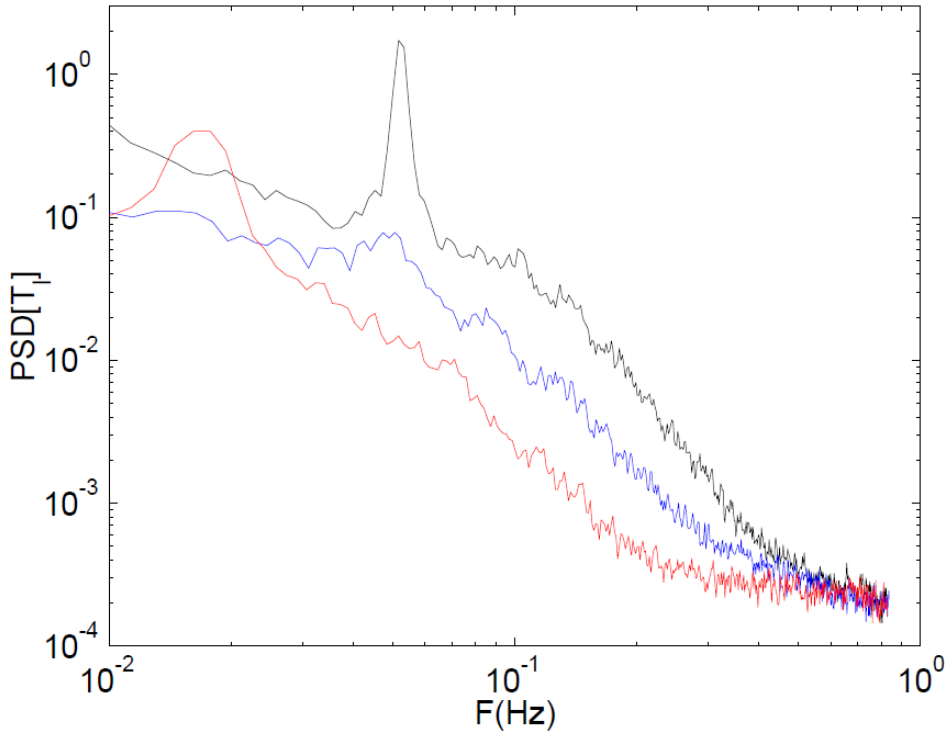

Figure 4.5: Power spectrum density of the temperature fluctuations at the surface of the lateral boundary, T_l for fixed imposed temperature difference $\Delta T = 11.6K$ and various magnetic fields, from the upper curve to the lower curve $B = 0\ G$ (in black); $B = 546\,G$ (in blue); $B = 1092\,G$ (in red).

The aim was to use the Lorentz force to drive a conductive fluid in a very simple geometry. We built a setup with a Taylor-Couette like geometry. There are 2 cylindrical electrodes generating a radial electrical current and the entire cell is put in an axial and constant magnetic field. Hence, we generate tangential force in the bulk. It moves the fluid without motion of the boundaries. It is known that in the traditional Taylor-Couette flow, a large range of flows and instabilities can be observed depending on the relative velocities of the cylinders forcing the fluid. In our case, we would like to know what will be the flows observed with our setup? Moreover, as the boundaries are motionless, we can expect that torque measurements will be easier. One experimental difficulty is to supply a uniform (or at least a symmetrical) electrical current. Accurate time-resolved velocity measurements in liquid metal were another challenge. We solved it by the use of Ultrasonic velocity probes. Moreover, due to induction phenomena, the current and thus the driving are limited to boundary layers. Hence, the forcing is not really in the bulk. After starting the experiment, we noted that such electromagnetic forcing has been explored in the past [106] with a different aspect ratio.The most surprising result is that, using accurate velocity measurement, resolved in time and in space along the probe axis, we show some instabilities and waves behaviors very similar to the ones observed by our predecessors. Indeed both experiments have used very different aspect ratios, cell geometries, fluids and forcing range parameters.

- *Travelling waves in a cylindrical magnetohydrodynamically forced flow [107]*

  J. Boisson, A. Klochko, F. Daviaud, V. Padilla and S. Aumaître Phys. Fluids **24** , 044101 (2012)

  Abstract: We present an experimental study of a liquid metal flow electromagnetically forced in a large aspect ratio coaxial cylindrical geometry. An azimuthal Lorentz force is applied on the liquid metal gap through a radial current and an axial magnetic field. Using ultrasonic velocity measurements we focus on the effect of these two parameters on the flow properties. We show that depending on the strength of the magnetic field and not only on the applied Lorentz force different dynamical states exist. We first observe a stationary structure at low forcing. Then two other regimes of different travelling waves are exhibited at higher forcing. We characterize them by their different frequencies and speeds. Higher magnetic fields clearly promote the faster waves. Connections with other magnetohydrodynamic instabilities are discussed.

4.5 Dynamics and instability in electromagnetically driven free surface flows

Works in collaboration

Pablo Gutierrez[1], François Daviaud[1], Cecile Gasquet–Wierthel[1], Vincent Padilla[1] Aurelie [2]and Daphné Heyres, Andreï Klochko, Ippeï Folliot, Tristan Rigaut[2]

This part is mainly extracted from the PhD work of Pablo Gutierrez [108]. As previously, we use an electromagnetic forcing, but we generate here a free surface turbulent flow. The aim is to characterize the properties of the free surface deformation induced by the turbulence and to study surface waves generation and their propagation. First we used floaters to track the properties of the flows generated by two magnet arrays of different geometries. Doing so, we noted that floaters do not behave like a passive scalar, but tend to cluster. They are expelled from the upwelling part of the flow and are clustered on the down-welling part of the flow. We quantified this phenomenon. Then we tried to characterize the surface deformation induced by the turbulent underlying flow. Finally, we are starting the study of the surface wave propagation on turbulent flows. Besides this work, we initiated also the study of the destabilization induced by a vertical magnetic field and a vertical current at the interface of a liquid metal and an electrolyte. Such instabilities might occur in aluminum production cell. In order to study a simpiflied problem where the same instability should occur, we used a mechanical analogue made of a flat copper pendulum immersed in copper sulfate solution .

[1]Sphinx–SPEC CEA-Saclay, France
[2]Studient ENSTA, France

4.5.1 Experimental devices

The aim of the device is to generate a strong turbulent flow with a free surface in an enclosed volume of fluid in a laboratory scale experiment. To do so, we used a layer of liquid metal forced by a uniform horizontal current and the magnetic field of an array of magnets. The use of a liquid metal, more precisely Gallinstan (an alloy made of Gallium Indium and tin), allows strong current densities hence a high stirring of the flow and an important surface deformation. The flow generated thereby is far from the 3D isotropic turbulence since the applied shear, mainly horizontal, produces mainly vertical vortices but it is not purely 2D because of the surface deformation and the secondary flows generated around the vortex. Liquid metals, like all metals, oxidize in air. The oxide forms a solid skin at the surface of Gallinstan. Therefore, to prevent it, one has to use reducer environment in order to keep the surface fluid. We use diluted solution of Chlorite acid (pH$\sim$1). This layer of acid is large enough to be in a *deep water limit*. IThis ensures that the Gallistan–acid interface is independent of the boundary condition at the top of the acid layer. Therefore one has to consider a single interface between the liquid metal (density of 6440 kg/m^3) and the HCl solution (density of 1000 kg/m^3).

Pictures and sketches of the device are depicted in figure 4.6. We use the two arrays of magnets shown at the bottom of figure 4.6. The flows produced by both arrays present different level of fluctuations. Indeed the regular array generates vortex about the same size and strength that compete all the time. Therefore, there are strong temporal fluctuations and the time-averaged flow contains only about 30%–25% of the total kinetic energy of the flow. In contrast the random array anchors large stable structures and the time-averaged flow contains more than 70% of the total kinetic energy. We will take advantage of this difference.

We used this device to study: the dispersion of floaters at the surface of a turbulent flow (section 5.4.2), the generation of waves by the deformed interface (section 5.4.3) and the propagation of waves on turbulent flows (section 5.4.4). These sections constitute a crude summary the Pablo Gutierrez PhD thesis [108].

4.5.2 Clusterization of floaters at the surface of turbulent flows

- *Experimental study on the clustering of floaters on the free surface of a turbulent flow [74]*
  P. Gutierrez and S. Aumaître submitted to Phys Fluid (2013)

  Abstract: We present an experimental study of the statistical properties of millimetric spheres floating on the surface of a turbulent flow. The flow is generated in a layer of liquid metal by an electromagnetic forcing. Using two arrays of magnets, we are able to create a highly fluctuating and an almost stationary flow. For both flows, we follow the motion of hundreds of millimeter-size particles floating at the deformed interface of the liquid metal. In both cases, we evidence the clustering of the floaters by a statistical study of local density of the particles. Some dynamical properties of clusters are exposed. With the almost stationary flow obtained with the random array of magnets, we are able to relate the cluster formation to compression effects. Hence, although floaters are not some passive scalars and move on a disturbed interface, we propose that the main clustering effect is the

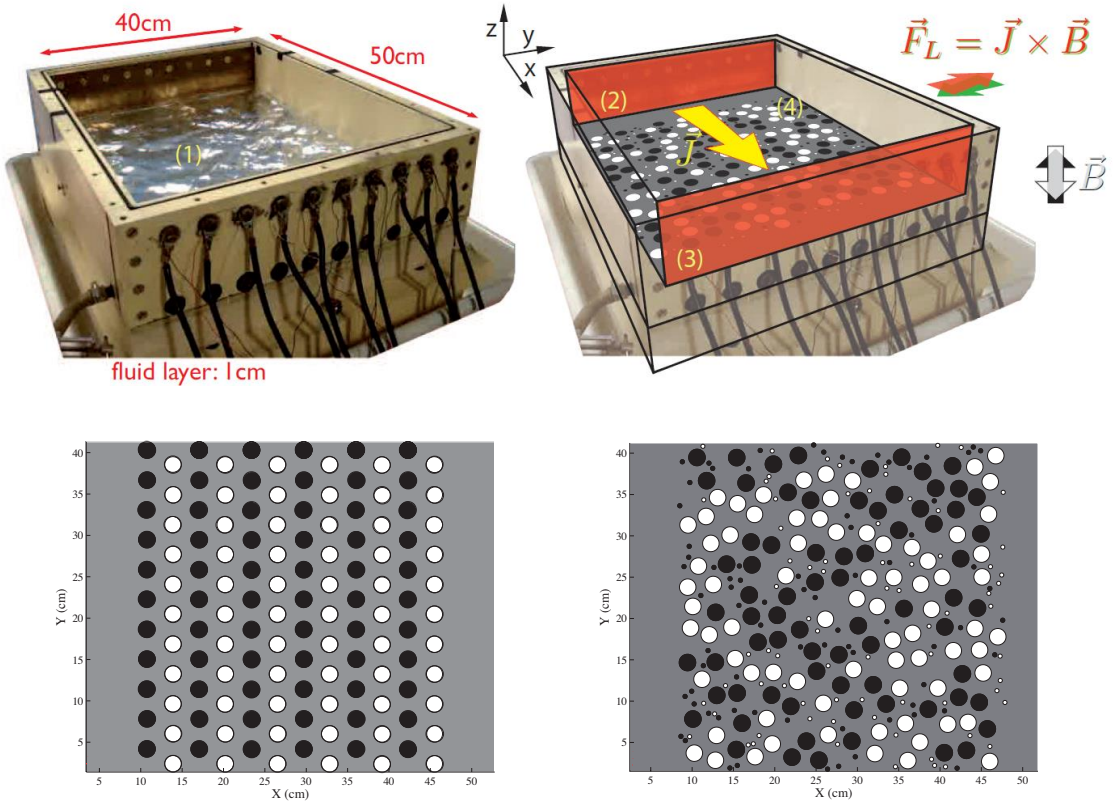

Figure 4.6: **Top:** Experimental device devoted to the study of free surface turbulence (left picture of the experiment. Right a cutaway). A layer of Gallinstan (1) is stirred by a density of current **J**, crossing the layer between the 2 brass electrodes (2) and (3), and the magnetic field, **B**, produced by the array of magnets (4). Current and magnetic field apply a Lorentz force $\mathbf{F_L}$ mainly horizontal.**Bottom** The regular (left) and random (right) magnets arrays used to stir the fluid.

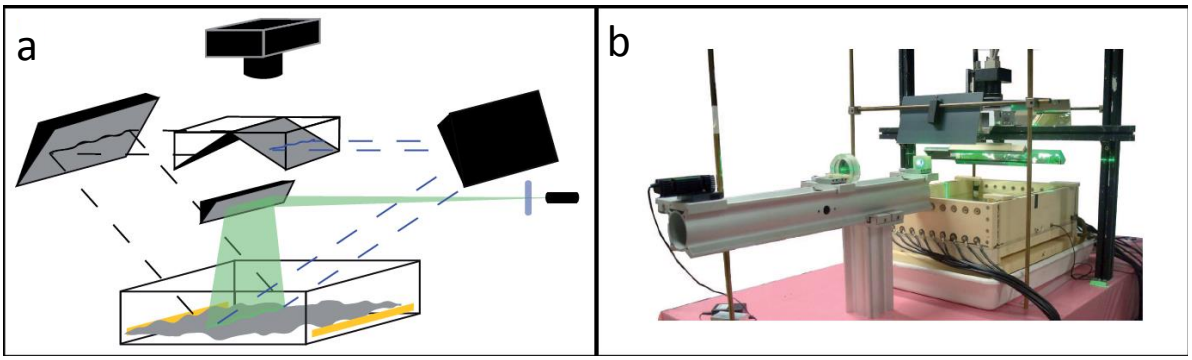

Figure 4.7: Optical measurement setup to track a diffusive line. **Left:** Sketch of the 2 angles triangulation technique using a single CMOS Camera. **Right:** Real picture of the experiment.

same than the one reported for passive scalar on an almost flat surface of a turbulent flow [109, 110].

4.5.3 Statistical properties of the surface deformation induced by turbulent flows

The measurements of the elevation of a liquid metal interface involve some difficulties. Liquid metals have a reflective surface, but the slope of the deformation is quickly too high to be deduced from the distorted image reflected on it. Indeed this image cannot be reconstructed unequivocally. The poor diffusivity of the surface does not allow the Fourier Transform Profilometry [111]. Local measurements are complicated by the presence of the acid, the magnetic field and the high current crossing the fluid. To get the local position of the interface we use inductive position sensors. These sensors filter the shortest wavelengths. Pablo also performs measurement of the surface deformation along a line by following the diffused trace lets by a laser sheet on the surface liquid metal that is not a perfect mirror. As the diffusivity is much weaker than the reflectivity, the CMOS sensor of the camera is sometime blinded by direct reflections in its direction. To solve this issue Pablo makes a tracking of the diffusive line under two viewing angles, as shown in figure 4.7.

Pictures in figure 4.8 show the surface state for different applied currents. It seems that more and more short wavelengths appear when the current is increased. The measurement of the fluctuations of the local elevation has a skewness that changes its sign from negative to positive around 300 A as shown figure 4.9. It is well known that weakly nonlinear waves induced interface fluctuations following a Tayfun distribution with a positive skewness [112]. In contrast, the deformation generated by vortex may induce fluctuations with negative skewness. Indeed the shape of the deformation is opposite as depicted in the inset of figure 4.9. Therefore waves-like

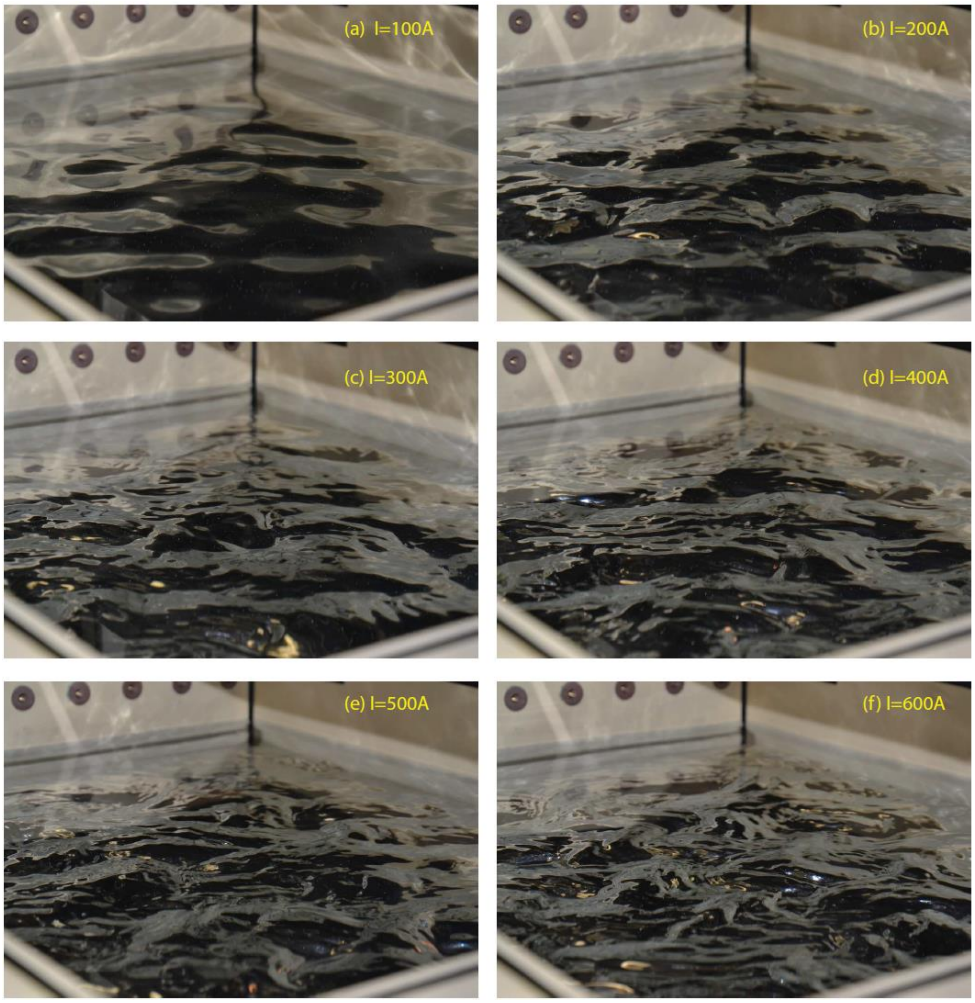

Figure 4.8: Pictures of the surface of the liquid metal driven by the regular magnets arrays and currents of 100, 200, 300, 400, 500, 600 A (from left to right and from top to bottom).

deformations may dominate under strong forcing and vortex deformations prevail at low forcing. Nevertheless, this measurement seems to depend on the sensor position and may be biased by the spatial filtering of the probe. Moreover results are less clear when one considers the fluctuations of the fluid height measured on the line.

The temporal fluctuations of the measurements along a line allow performing a 2D Fast Fourier Transform in both time and space. Therefore we can compute 2D Power Density Spectrum (PDS) in the frequency–wave number plane. In this plane, surface waves have to follow the dispersion relation:

$$f^2 = \frac{g}{2\pi\lambda} + \frac{2\pi\gamma}{\rho\lambda^3} \tag{4.8}$$

with f the wave frequency and λ its wavelength. Figure 4.10 shows the 2D PDS in logarithmic color scale for both magnets arrays at two different intensities. The dispersion relation (4.8) is

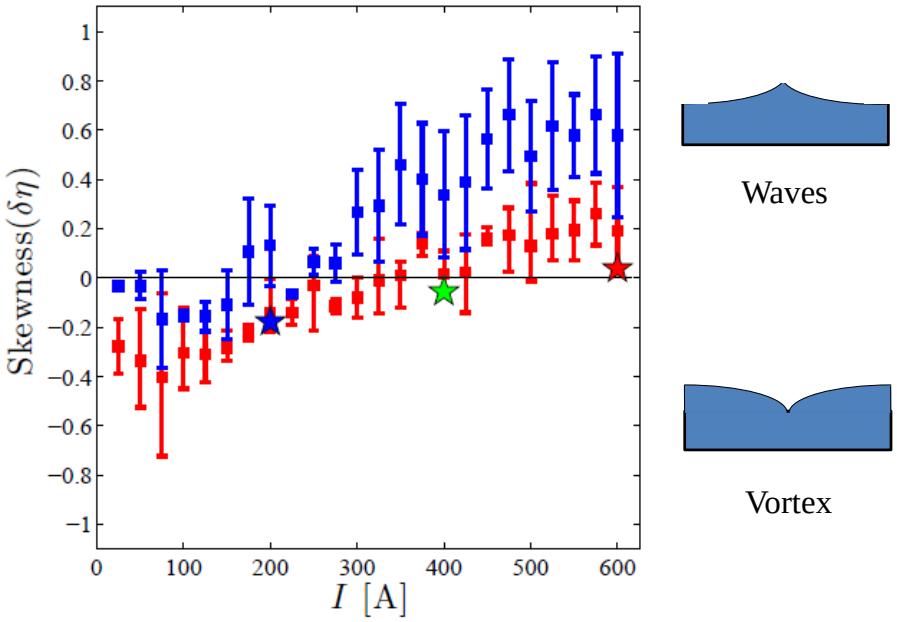

Figure 4.9: Evolution of the skewness of the surface deformation measured by the local inductive probe with the forcing intensity in both magnets arrays. Stars underline this skewness for longer measurements performed at different positions. The inset depicts a typical surface deformation induced by a wave (top) and a vortex (bottom).

drawn by a black line. The intense patch at low frequencies and large wavelengths is due to the vortex, but we can see a branch following (4.8). However this represents a small part of the PDS (one has to take a logarithmic color scalar to see it in figure 4.10) and seems to evolve only slightly with the forcing. Moreover, it will be difficult to get a more quantitative estimate of the energy transmitted to the surface waves with this measurement. A more accurate reconstruction of the 2D surface elevation is required.

4.5.4 Surface wave propagation on a turbulent flow

The last phenomenon studied with this device is the propagation of dispersive surface waves above the free surface of a turbulent flow generated by the regular array of magnets. It is related to the general problem of wave propagation through random media and localization. Here the waves are dispersive and nonlinear and the scatters, consisting of velocity gradients and vortices, are not isotropic and have long range interactions. To tackle this complex problem, we consider first the global damping of the waves induced by turbulence. A monochromatic wave is generated by a wave maker pushing the surface sinusoidally at a single frequency. The surface elevation is controlled with the diffused line technique. Motion of the wavemaker is controlled by an inductive position sensor. Another sensor is used to probe the local elevation in several locations. The precise geometry of the setup is depicted in the figure 4.11.

In order to remove the fluctuations of the turbulence, we perform a coherent time-average of the surface elevation, η, i.e. we average the measurements occurring at the same period of the wave. Hence one keeps the coherent spatial evolution of the wave and one cancels the incoherent fluctuations of the surface induced by the regular array of magnets. Since the aquisition

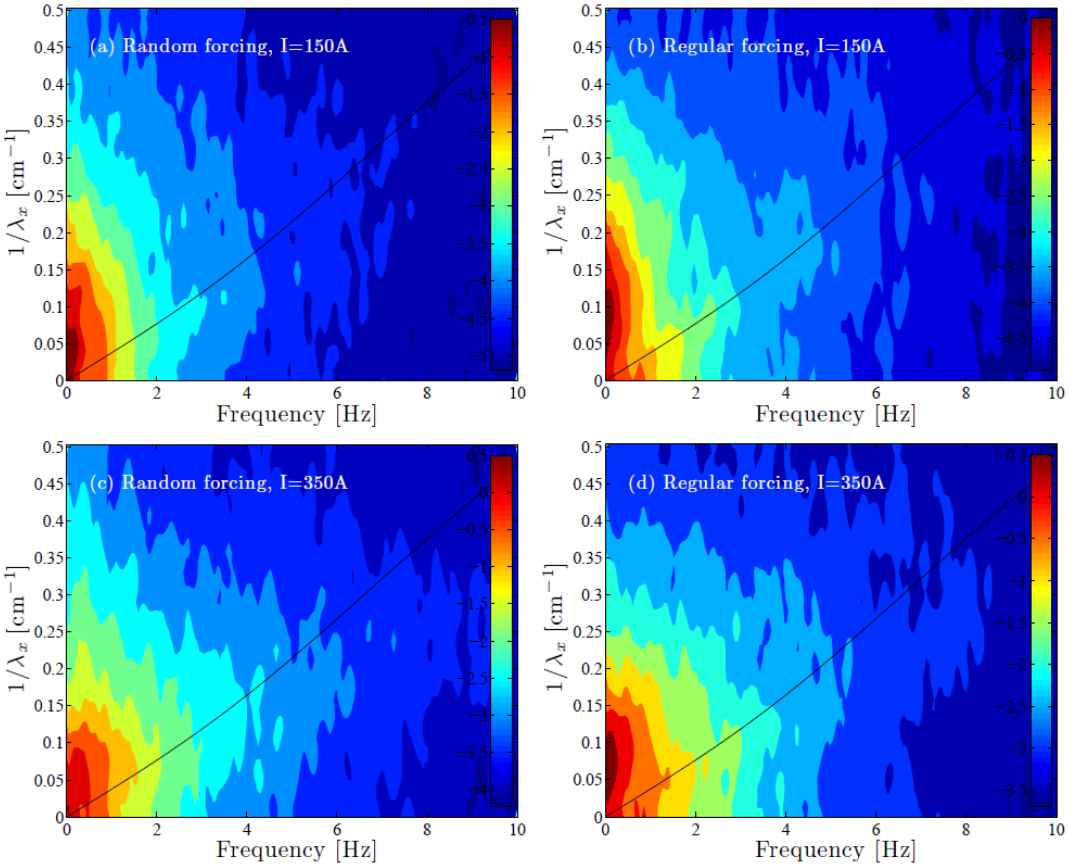

Figure 4.10: 2D power density spectra of the surface deformation. **Left:** Random forcing, **right:** regular forcing. **Top** for a driving intensity of 150 A, **bottom** for a driving intensity of 350 A.

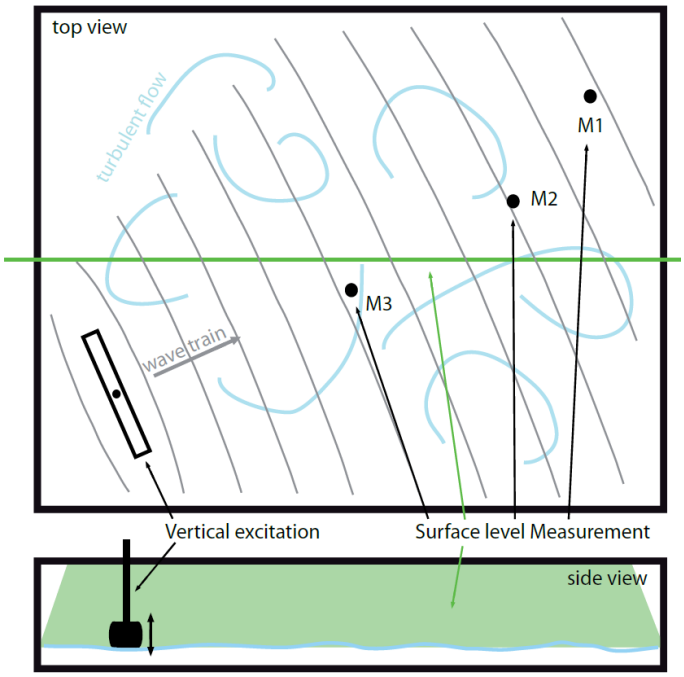

Figure 4.11: Sketch of the experimental setup built to estimate the damping of surface waves by a turbulent flow.

time is smaller than the wave period, we can match several measurement points per period. Therefore several coherent averages can be computed corresponding to different phases of the wave. They are plotted all together in figure 4.12 showing the spatial evolution of the wave at various driving current intensities and two specific wave frequencies. We clearly see that the stronger is the forcing, the stronger is the damping. To quantify this, we compute the rms of spatial fluctuations of the wave amplitude σ_η. Smaller is this rms, larger is the damping. For a classical viscous damping, the amplitude decreases exponentially as $\langle \eta \rangle_T(x) \propto \exp(-\alpha x)\cos(k_x x)$ with $\langle \cdot \rangle_T$ notifying the coherent average. In that case, the decay rate is given by $\alpha \propto 1/\sigma_\eta^2$. In our measurements even without turbulence, we do not observe an exponentially decaying oscillation. This is due to the fact that this decay is very small in liquid metals and the wave can travel back and forth in the cell. Therefore the propagating wave undergoes a lot of interferences with the waves reflected by the cell boundary. Moreover, the waves are generated by the finite size wavemaker and thus they are not plane waves. This explains why no decay is observed on the messy black curves in the bottom of the figure 4.12 where no electromagnetic forcing is applied. However we will assume that the ratio of the variance of the spatial fluctuations with and without turbulence gives an idea of the excess of damping introduced by turbulent flows i.e. we assume that

$$\frac{\alpha_I}{\alpha_o} \propto \frac{\sigma_\eta^2|_o}{\sigma_\eta^2|_I} \tag{4.9}$$

where $\sigma_\eta^2|_I$ is the variance of the spatial fluctuations of the elevation after coherent–averaging with an applied current I.

Two theoretical predictions have been proposed for the damping of gravity surface wave induced by turbulence. They consider two opposite limits. The first one, proposed by Phillips,

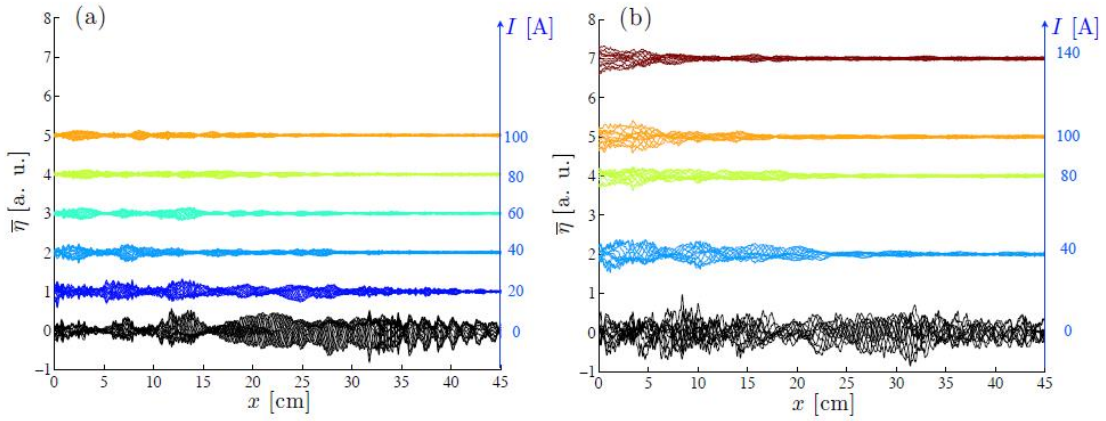

Figure 4.12: Spatial evolution of the coherently averaged surface waves for various applied currents going from 0 to 140 Amp. (a) the wave is generated at 5 Hz corresponding to a wavelength of 6.5 cm. (b) the wave is generated at 8 Hz corresponding to a wave length of 3.18 cm

considers that the wavelengths of the surface wave are much smaller than the injection scale of turbulence [113]. This is more an oceanographic limit where the swell is damped by very large scale currents. In contrast, Teixeira and Belcher consider wavelengths much larger than the characteristic size of the flow [114]. Actually both points of view can merge in a single one. Indeed in both cases, it is assumed that the energy of the wave is transmitted to the flow by the Reynolds stress, $R_{ij} \equiv \rho\overline{u_i' u_j'}$, acting at the wavelength of the wave $\lambda = 2\pi/k$, where u_i' is the fluctuating part of the the velocity component i , ρ is the density and $\overline{\cdot}$ stands for time average. One can argue, with dimensional arguments, that $\alpha_{tur} \propto \frac{U_k^2 k^2}{g}$ where U_k is the typical value of the velocity increments at the scale k. In Phillips case, where k is in the inertial range, one can deduce U_k form the classical Kolmogorov theory of turbulence. One gets $U_k^2 \propto \epsilon^{2/3} k^{-2/3}$, where $\epsilon \propto U_o^3/L$ is the turbulent rate of energy transfer with U_o the velocity at the energy injection scale L. Therefore the Phillips prediction is recovered $\alpha_{tur} \propto \frac{\epsilon^{2/3} k^{4/3}}{g}$. In the large wavelength limit, one has to take $U_k \sim U_o$ to recover the Teixeira and Belcher prediction $\alpha_{tur} \propto \frac{U_o^2 k^2}{g}$.

Our experimental case is not in these limits. In contrast, we can easily generate wave with wavelength of order of the forcing length scale (the matching is reached with a wave of 7 Hz). Moreover the capillarity cannot be completely neglected and corrections like $\frac{U_k^2 \rho}{\gamma}$ can be expected at the shortest wavelengths. Hence, we do not expect that one of the predictions fits our data. Figure 4.13 shows the ratio of the damping rate as defined in equation 4.9, as a function of the driving intensity for four different wave frequencies. With our electromagnetic forcing, one expects $U_o \propto \sqrt{I}$. Therefore using the Teixeira and Belcher prediction, one expects a collapse of all curves

in a single straight-line when the ratio is plotted as function of I/λ^2. Although we are not in the limit of the Teixeira and Belcher prediction, the collapse of the curve is better when the rescaling by λ^2 is applied (figure 4.13-right) than when no rescaling is used (figure 4.13–left). However the curves follow a linear behavior at low control parameter and another at larger forcing. The figure 4.13 shows also that the wave at 7 Hz (for which the wavelength match with the forcing length scale) still differs from the other and the turbulent damping seems less efficient.

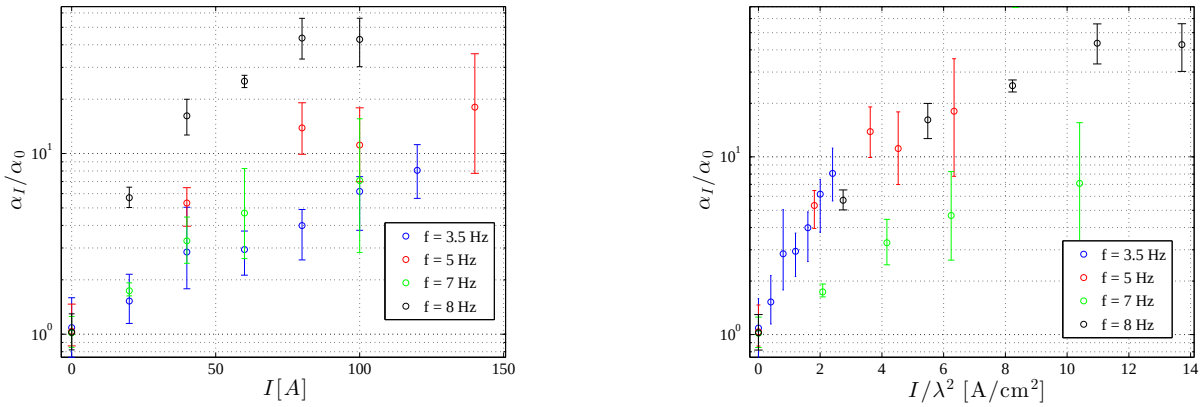

Figure 4.13: Relative turbulent damping as a function of the applied current (left) and as a function of the applied current divided by the square of the wavelength of the surface wave. Monochromatic wave of frequencies $f \in [3.5\ 5\ 7\ 8]$ Hz corresponding to wavelengths $\lambda \in [13\ 6.55\ 3.85\ 3.18]$ cm are represented.

Both theoretical predictions assume that the energy lost by the wave is transmitted to the underlying flow, either by vortex stretching or through the turbulent cascade. However, other energy transfer mecanisms like the specific scattering of the waves by vortices and the nonlinear interactions between waves, can contribute as well to the damping. To go further in this study a 2D measurement of the surface elevation will be helpful. Another interesting perspective will be the use of horizontal magnetic field with alternating polarities. We should therefore generate rolls with a much stronger horizontal vorticity that should affect strongly the wave propagation.

4.5.5 Surface instability induced by a vertical magnetic field and a vertical current

Motivations

The aim is to study an interface destabilization generated by a vertical electrical current and a vertical magnetic field. The configuration, sketched in figure 4.14–a, is the following: a liquid metal (a good conducting fluid) is below an electrolyte (a bad conducting fluid). An electrical current and a magnetic field are applied perpendicularly to the interface. Hence, for a flat interface no resulting force occurs. But if the interface is deformed, the current tends to go preferentially where the electrolyte layer is reduced, because it is the lower resistive electrical path. Then some horizontal short-circuit currents appear in the liquid metal in order to reach the equipotential

electrodes underneath the liquid metal. This horizontal component of the current can interact with the magnetic field and generates a Lorentz force perpendicular to the initial perturbation. Hence, we have a typical two–dimensional destabilization process. Such a mechanism might be involved in the Hall-Héroult cells used to produce aluminum [115]. It imposes a relatively large layer of electrolyte that limits the current available for electrolyze and thus, the efficiency of the aluminum production.

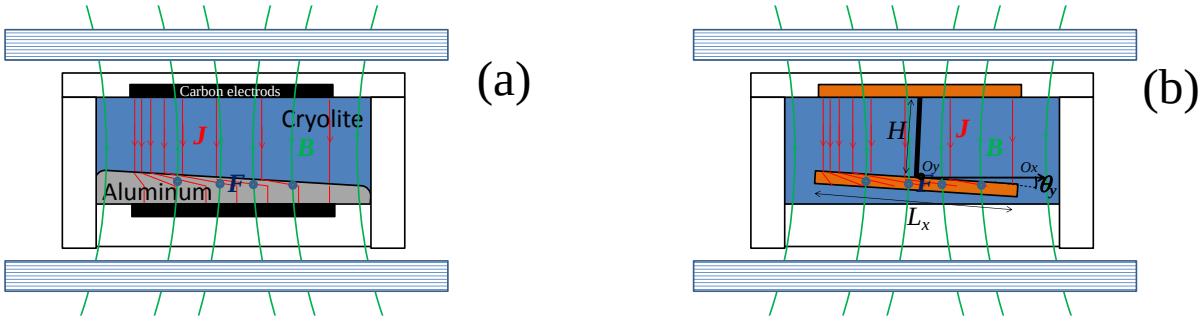

Figure 4.14: Sketch of the surface or pendulum 2D instability induced by a vertical electrical current of density J and a vertical magnetic field B. **(a)** In the case of the aluminum electrolyze cell, the current provided by Carbon electrodes crosses vertically the poorly conducting electrolyte (named Cryolite) with a density inversely proportional to the electrolyte depth. In the good conducting aluminum layer, there are an horizontal short-circuit current in order to reach the Carbon Anode with a uniform distribution. Hence horizontal currents interact with the magnetic field to generate a Force perpendicular to the initial slope of the interface. **(b)** A flat copper pendulum immersed in copper sulfate and crossed by a vertical current and magnetic field should experience the same instability process.

The same mechanism has to occur also when the conducting fluid layer is replaced by a flat metallic pendulum immersed in an electrolyte in presence of vertical current and magnetic field as depicted in figure 4.14–b. This mechanical analogue has been proposed by Davidson and Lindsay [115]. By using a copper pendulum immersed in Copper Sulfate solution, we prevent any complex reactions and gaseous emissions at electrodes, the ions Cu^{++} produced at the anode being consumed at the cathode (to our knowledge this is the only red-ox couple allowing this simple reversible mechanism). For such a simplified problem, if we neglect the viscous damping, one can write

$$\begin{aligned} \ddot{\theta_x} &= \omega_x^2 \theta_x + \beta_y \theta_y \\ \ddot{\theta_y} &= \omega_y^2 \theta_y - \beta_x \theta_x \end{aligned} \tag{4.10}$$

where θ_x (resp. θ_y) is the oscillation angle around the Ox (resp. Oy) axis, ω_x (resp. ω_y) is the eigen frequency in the corresponding direction, and $\beta_x = J_o B_o L_x/(2\Delta\rho H^2)$ is the cross term induced by the Lorentz force with J_o the imposed current density, B_o the imposed magnetic field,

H the pendulum height, L_x and L_y the sizes of the flat pendulum and $\Delta\rho = \rho_{Cu} - \rho_{el}$ the copper density minus the electrolyte density.

The instability onset is then given by

$$\beta_x \cdot \beta_y \geq (\omega_x^2 - \omega_y^2)^2/2 \tag{4.11}$$

Hence for a symmetrical pendulum where $\omega_x = \omega_y$, the pendulum without dissipation should move alone as soon as a magnetic field and a current are switched on. Obviously to really describe the instability onset one has to introduce a damping term. Moreover this damping term might depend on the applied current and magnetic field. For instance, the motion of the copper in the magnetic field will induce Foucault currents which dissipate energy by Joule effect. Hence, magnetic field and current may not play a symmetrical role and their product may not be the relevant control parameter. In order to evaluate this damping term, we build the flat copper pendulum immersed in Copper Sulfate solution depicted in figure 4.15 and we studied its mechanical response to an external horizontal forcing as a function of the applied magnetic field and the current. Without amplification by the current and magnetic field together, the mechanical response of a damped pendulum to an external sinusoidal acceleration $\mathbf{A}(t) = A_o \cos(\Omega_o t)\mathbf{e_x}$ is:

$$\theta_x = \frac{A}{(\Omega_o^2 - \omega_x^2)^2 + \gamma^2\Omega_o^2}\Big((\Omega_o^2 - \omega_x^2)\cos(\Omega_o t) - \gamma(I,B)\Omega_o \sin(\Omega_o t)\Big) \tag{4.12}$$

where the damping term $\gamma(I, B)$, may depend either on the applied current or the applied magnetic field or both. By studying the pendulum displacement as a function of the forcing frequency Ω_o, one should observe a resonance peak at the eigenfrequency $\Omega_o = \omega_x$, the width of the peak being fixed by the damping.

Preliminary results

The experimental device, briefly described in figure 4.15, consists of a circular flat copper pendulum about 100 mm diameter for 5 mm width. The distance, H, between the pendulum and the upper copper electrode is about 60 mm. It is immersed in a saturated solution of Copper sulfate. In this geometry, one expects $\omega_x \sim \omega_y$ and $\beta_x = \beta_y$. The magnetic field is provided by a strong Neodymium-Bore-Nickel magnet of size $16 \times 9 \times 2.5$ cm. The magnetic field is neither perfectly vertical nor uniform but by symmetry, it should not induce any force on the pendulum at rest. The strength of the magnetic field can be modulated by changing the distance from the pendulum to the magnet. The entire cell is vibrated horizontally by a motor and connecting-rods. The velocity in the co-moving frame of the lower plate is known from US probes working at 4MHz. The echo peak gives the position and the velocity is known by the variation of the flight time of two successive pulses. We also tried to measure the depth of the electrolyte layer under the pendulum by resistive measurements, but they were not quantitative enough to be used. The driving force is known by an accelerometer screwed to the cell.

We first check the pendulum response as the function of the external forcing frequency without current and magnetic field. As expected, the response presents a peak which is the eigenfrequency of the pendulum. This peak is around the expected one, $f_o = \sqrt{g/H}/(2\pi)$. Once the magnetic

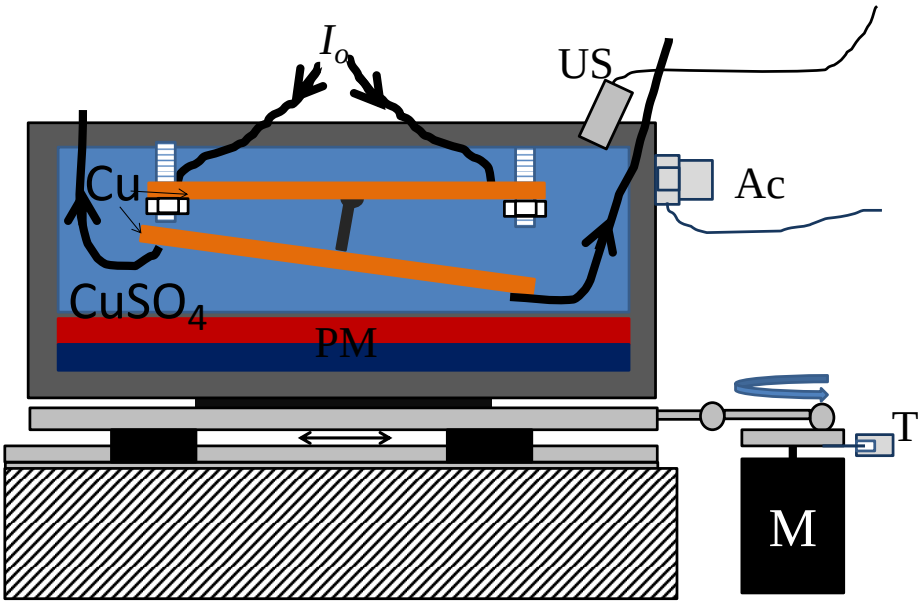

Figure 4.15: Sketch of the electromagnetic surface instability device. Two circular copper plates remote from a distance H are used as electrodes. The bottom one is free to move in all directions. The horizontal vibration in the Ox direction is supplied by the motor (M). Its velocity is controlled by a tachymeter (T). The accelerometer (Ac) records the applied force to the cell. The velocity and the position of the bottom copper plate is measured by Ultrasonic probes (US) in the direction of the forcing and perpendicular to it. An underneath permanent magnet (PM) provides a strong magnetic field (about 0.1 T).

field is added without electrical current, a clear damping effect is illustrated by the decay of the resonance peak and its enlargement. Moreover a slight shift of the order of $(\pi\gamma/f_o)$ is expected for an increment of the damping about γ. Surprisingly, when the current is switched on, no measurable effects are detected neither in the excitation direction nor perpendicular to it.

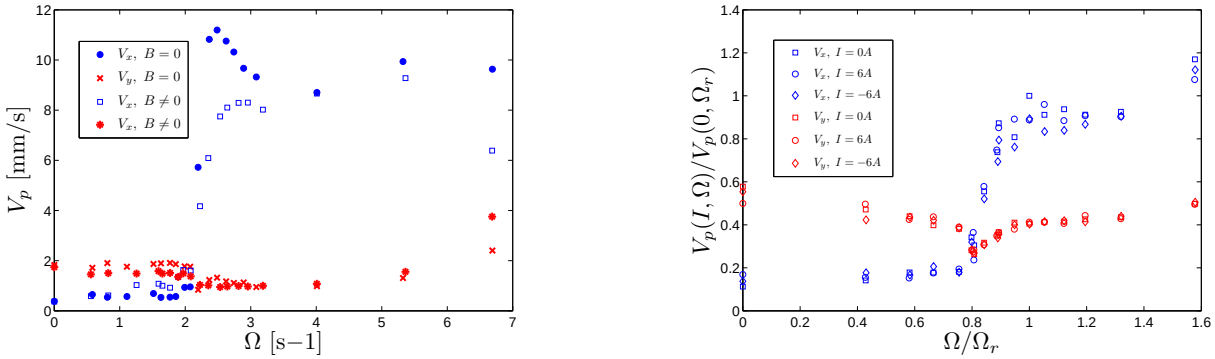

Figure 4.16: **Left :** Mechanical response of a flat 2D copper pendulum without magnetic field and without current in the excitation direction Ox (full blue circle) and perpendicular to it (red cross); with a vertical magnetic field only, in Ox direction (open blue square) and Oy direction (red asterix). **Right :** Mechanical response of the pendulum when the current is added normalized by the response at the resonance without current.

To conclude, in our experiment geometry (where an electrical current and a magnetic field are applied perpendicularly to the interface of a poorly conducting but light electrolyte and a good conducting but heavy metal), we underline the important role of the damping and especially the dissipation induced by the Foucault currents. However, we do not see any effect of the applied current. This might be because we are too far from the instability onset. Unfortunately we cannot increase much further the current without generating lot of copper particles and complex reactions at the electrodes that perturb the measurement. Recently, Pedchenko, Molokov *et al* have circumvented the difficulties induced by the electrolyze [116]. They mimic the current in the electrolyte by a network of vertical wires dipping in a liquid metal. With this trick, they succeeded to reach the instability onset. Although our experiment seems to show that the magnetic field and the current do not play a symmetrical role at least at the level of the dissipation, in [116], when the threshold of the surface instability is concerned, it seems to depend only on the product $J_o \times B_o$ [116].

Chapter 5

Perspective and further experiments

Works with further collaborators

To conclude with this manuscript, we present two experiments that we dream to realize. Both concern turbulent transport. The first proposal is about the heat transport in the turbulent Rayleigh–Bénard convection. Our goal is to measure the heat transfer in a Rayleigh-Bénard convective cell as a function of the height. Indeed this heat flux, constant in average, is subject to very different transport mechanisms. In the center, a turbulent transport occurs, whereas conductive boundary layers dominate close to the walls. We expect to learn a lot about the main transport phenomena in turbulent convection and about the role of the large scale flow, by the study of the temporal fluctuations as well as the spatial fluctuations of the heat flux. This necessitates the measurement of the temperature field and of the vertical velocity field in the cross section of the cell at various altitudes. Some possible measurement techniques and experimental devices are discussed. The second proposal is even more challenging. We would like to be able to measure of the dissipation rate resolved in time in a turbulent flow. To do so, we propose to use the correlation of speckle images of a multi-scattered light crossing the flow. This technique is commonly used in solid state physics to measure small displacements and elastic properties of materials. In fluids, it could give a direct access to the square of the velocity gradient averaged on the volume of the crossed sample and thus to the dissipation occurring in this volume. The feasibility of the measurement and the best experimental configurations will be discussed.

5.1 Introduction and motivations

In previous parts of the manuscript, we gave some potential extensions of the works already realized and some evolution of existing experiments. This ultimate part presents two experiments that we would like to build up. Both concern the energy transport in turbulent flows. Both are challenging from an experimental point of view. However, we think that their potential impact deserves that we devote time and means to them.

The first experiment concerns the well knonw problem of turbulent convection. Due to its large impact in geophysical flows and thermal engineering, the determination of the law between the temperature difference, ΔT and heat flux q in the simple Rayleigh–Bénard configuration has attracted a lot of attention (see [117, 118, 119] for recent reviews). Several scaling laws between the dimensionless Rayleigh number and Nusselt number have been proposed depending on the main transport mechanism : through boundary layers or in the turbulent bulk. Our objective is to measure the heat flux across the convective cell at different heights. Although it has to be constant in averaged, the heat transport mechanism will be different near the boundary, where conduction dominates, and in the bulk, where turbulent advection prevails. The measure of the local repartition of heat flux and its temporal fluctuations should help to estimate the main transport mechanisms, the role of the large scale flow etc....

The second prospective experiment will be dedicated to probe the dissipation in turbulent flows. As often discussed previously in the manuscript, a turbulent flow is a stationary out-of-equilibrium system where injected energy is balanced by the dissipated one in averaged. Instantaneously, the system may store or release energy and the time-correlation between injected and dissipated power is not obvious and should depend on the complex energy transfer through inertial range scales. Global measurements resolved in time of the dissipative power are very challenging. The promising method proposed here will use turbid media. The analysis of the speckle images coming from multi-scattered light crossing the cell should give an estimate of the square the velocity gradients [120, 121] directly proportional to the dissipation rate. With the very high speed camera now available, one can expect to reach the time resolved fluctuations of this quantity or at least to its correlation time. By combining global and local measurements, one should be able to understand a little more how the highly inhomogeneous dissipative rate constructs the instantaneous global power dissipation which is constrained to converge to the injected power due to stationarity.

5.2 Measurement of the heat transport inside Rayleigh-Bénard turbulent convection

5.2.1 Motivation

In addition to rotation, convection is one of main motor of many geophysical and astrophysical flows from atmospheric motions to mantle flows. It is also a really efficient mechanism to evacuate the heat that has to be well modeled in climate prediction as well as in industrial designs (see for instance self-cooling nuclear reactors to compensate a cooling system deficiency [122]). In any case, it is crucial to have appropriate laws, linking temperature gradients and heat flux that could be extended on a huge range of parameters. However, even in the simplest case of the well posed problem of the convective transport between two horizontal plates, this subject is highly debated. The existence of an ultimate regime is still controversial and the role of a large scale mean flow, thermal boundary conditions etc. ...are still not clear.

The Rayleigh-Bénard configuration is probably the most studied system to understand turbulent heat transport. In the idealized case, one considers a Boussinesq fluid. In such an ap-

proximation, all the physical properties of the fluid are assumed to be temperature independent except in the buoyancy force, where linear temperature dependence is assumed for the density. This approximation is justified as long as the relative temperature difference is small and the hydrostatic pressure variation can be neglected [123]. The fluid is heated from below. It is enclosed in perfectly conducting horizontal plate at the top and bottom of the cell, separated by a distance H, and perfectly insulating lateral boundaries such that the heat flux has to be conserved over all the height. Using the imposed temperature gradient, ΔT, as temperature scale, H as a size scale, and H^2/κ as time scale with κ the temperature diffusivity, the dimensionless Boussinesq equations of heat transport are:

$$\begin{aligned} Pr^{-1}\left(\partial_t u_i + u_j \partial_j u_i\right) &= \partial_i p + Ra\theta\delta_{iz} + \partial_{jj} u_i \\ \partial_t \theta + u_j \partial_j \theta &= \partial_{jj}\theta \end{aligned} \tag{5.1}$$

with θ the dimensionless temperature fluctuations, u_i the dimensionless velocity component, p a dimensionless pressure. For a given aspect ratio of the cell $\Gamma = H/D$ with D the lateral size of the cell, they depend on two and only two dimensionless numbers, the ratio of the thermal over the momentum diffusivity $\mathrm{Pr} = \nu/\kappa$, called the Prandtl number, fixed by the fluid, and the Rayleigh number $Ra = \alpha g \Delta T H^3/(\kappa\nu)$.

Therefore, in a given configuration, the dimensionless heat flux, called the Nusselt number $Nu = qH/(\Delta T\lambda)$ with λ the heat conductivity, can be described by these two parameters. The main challenge of the Rayleigh–Bénard study is to determine the laws $Nu = f(Ra, Pr)$ and their range of validity. In the turbulent regime, various scaling laws have been proposed, based on different assumptions on the main transport mechanism. For instance, on one hand, Malkus [124] has first proposed that, in the turbulent regime, the heat transport is limited by thin thermal boundary layer near the horizontal walls. Thus the distance between the plates, H, becomes irrelevant in the estimation of q. One gets necessarily $Nu \propto Ra^{1/3}$. On the other hand, one can assume that in the fully turbulent regime, the thermal and viscous diffusivity do not play any role in heat transport [125]. Thus the scaling has to be $Nu = Pr^{1/2}Nu^{1/2}$. More recently, based on a precise study of the dominant transport process, Grossmann and Lhose established a diagram in the plane Pr, Ra of the expected exponent β and γ such that $Nu \propto, Pr^{\beta}Ra^{\gamma}$. They identified seven zones corresponding to different scaling laws in the plane $(Pr,\ Ra)$ [126].

The comparison with experimental measurements is difficult because the exact boundaries of the scaling area are not so well defined. Moreover, the different scaling laws have to be tested over a large parameter range to prevent the artifacts coming from the crossover region between two scaling laws. And it is often difficult to change the Rayleigh number over a wide range without modifying the Prandtl number. However, below $Ra = 10^9$, there is a relative good agreement between experiments at least for $Pr \geq 1$. Moreover the experimental measurements are compatible with theoretical scaling predictions [126, 118]. In contrast, above $Ra = 10^{12}$, the experiments exhibit very different behaviors [118]. And most challenging questions about turbulent convection, like the existence of an ultimate regime, arise at such high Rayleigh numbers [127]. Actually, small experimental changes seem to be able to generate different power laws. Moreover, experiments are never in the ideal case: boundary conditions are not perfect, real fluids are not Boussinesq. The cell aspect ratio should modify the large scale flow and thus the transport efficiency. The role of these imperfections in the scaling laws have to be clarified.

Our goal is to perform a direct measurement of the heat flux inside the cell, i.e. to compute the local vertical heat flux in the section of the cell at a given altitude z: $q(x,y,t)|_z = \partial_z\theta(x,y,z,t) - u_z(x,y,z,t)\theta(x,y,z,t)$. Averaged in x and y on the whole section, this quantity is assumed to be proportional to the Nusselt number and independent of z after time-average. However fluctuations are expected and they should differ in the middle of the cell where the turbulent fluctuations of the advective term: $u_z(x,y,z,t)\theta(x,y,z,t)$ are the strongest, and in the thermal boundary layer where by definition the conduction $\partial_z\theta(x,y,z,t)$ dominates. Hence the study of the fluctuations of $q(x,y,t)|_z$ should underline the main transport phenomena. By the study of the spatial fluctuations, one should underline the role of the large scale flows and of the role of the thermal plumes in the heat transport. But to do so, one has to measure simultaneously the temperature field and the vertical velocity field at a given altitude, both resolved in space and time.

5.2.2 Experimental techniques and setup

We would like to show that new techniques like the stereo PIV, the liquid crystal thermometry or the LIF could be useful tools for the prescribed objective: the measure of the local heat flux. All these techniques have been used and even combined [128, 129] to measure heat flux. However, they have not been fully exploited whereas they seems to be powerful tools to answer some of the open questions of turbulent convection. Let us first remind the characteristic length and time scales involved in turbulent convection, before briefly summarizing these techniques and theirs limits and discussing the experimental cell geometry.

Characteristics length and time scales

In convective cells driven by buoyancy one can define a characteristic velocity for the large scale flow $U_o = \sqrt{\alpha g \Delta T H}$ and a Reynolds number, $Re = U_o H/\nu = (PrRa)^{1/2}$. Therefore one can also use a characteristic time scale as $\tau_c = L_c/U_o$. However, depending on the phenomena under consideration, several length scales L_c can be defined. Obviously, there are global length scale like the cell height, H or the cell width, D; linked by the aspect ratio $\Gamma = D/H$ usually of order unity in experimental cells (It is typically 1 or 1/2 in most of the devices). It defines the turn over time of the large scale structure, $T_o = H/U_o$. Some others characteristic lengths can be defined like the Kolmogorov length scale $\eta_K/H \propto 1/Re^{3/4} \propto 1/(PrRa)^{3/8}$. The time scale associated with this length is the Kolmogorov time $\tau_K = \sqrt{\nu/\epsilon} = Re^{-1/2}T_o$ with ϵ the dissipation rate. Another important length scale is the width of the viscous sublayer, e_ν. There is one way to define it: it is the height where the viscous diffusivity compensates advection, thus $\nu U_o/e_\nu^2 \sim U_o^2/H$ and $e_\nu/H \propto 1/Re^{1/2} \propto 1/(PrRa)^{1/4}$. Finally the width of the thermal boundary layer, e_κ is also an important length that we would like to resolve. It is usually defined as the length able to transport all the heat flux by conduction, thus $e_\kappa/H = 1/Nu = 1/(Pr^\beta Ra^\gamma)$. The challenge is to design an experimental setup able to resolve most of this length scales and the associated time scale. With the usual exponents found in the literature for turbulent convection in water ($Pr \sim 7$), one has the hierarchy: $\eta_K << e_\kappa < e_\nu << H$.

Experimental measurement techniques

- Stereo-PIV: The Particle Image Velocimetry uses a fluid seeded with small isodense particles enlighten by a laser sheet. The principle of this technique is to follow the motion of the pattern induced by the inhomogeneity of the reflectivity or the diffusivity in the laser sheet that are caused the moving particles. Two successive images are divided in small windows about 10 pixel^2. A sub-window at a given position is correlated in the two successive images in order to get the Eulerian displacement in this subwindow. The spatial resolution is therefore ten times samller than the camera resolution. With a single camera, one gets the 2 components of the velocity field in the plane of the laser sheet. By the correlation of the velocity field obtained with 2 cameras pointing with different incident angles on the laser sheet, one can also deduce the 3rd component perpendicular to the laser sheet. Hence in the case of the heat flux in turbulent convection one can get $u_z(x,y,t)|_z$ in a horizontal plane. The stereo–PIV techniques are now well established. Their main limitation is related to the spatial resolution bounded by the size of correlation window. The time–resolution fixed by the camera frame rate, should not be a problem in turbulent convection (see below).

- Liquid Crystal Thermometry: Cholesteric nematic liquid crystals have a twisted structure and then diffract light with a given wavelength at a given angle following the Bragg diffraction law: $\lambda(\theta) = a(T)$. The twisted length $a(T)$ of the liquid crystals depend on the temperature. Hence a Cholesteric Liquid Crystals(CLC) enlighten with a white light source and observed at a fixed angle will diffract the incoming white light at a given wavelength depending on the temperature. This technique is used to measure temperature since the seventies [130]. Encapsulate CLC are now sold to measure temperature. They are proposed in various temperature ranges around the ambient temperature (from few degrees to few tenth degrees) and thus are quite well adapted to the temperature range of turbulent convection in water. The encapsulate CLC can be enlighten with a supercontinum white laser sheet and used as seeded particles for PIV measurements [129]. Their time response is about 3 ms [131]. The main problem of the technique comes from its relative imperfection (temperature measurement precision is about 5%). Moreover the color observed in a given direction depends on the precise geometry of the cell and a precise calibration has to be done *in situ*. Finally we have to use a color–camera usually 3 times less resolved than equivalent a monochrome camera.

- LIF: Light Induced Fluorescent (LIF) techniques are based on the temperature dependence of the light emitted by some fluorescent molecules like Rhodamine B or fluorescein 27. Excited at given absorption wavelength λ_a the emitted light of the molecule at a wavelength λ_e has an intensity $I = I_o C \epsilon \Phi(T)$ where I_o is the intensity of the incident light, C is the molecule concentration. In order to distinguish the temperature fluctuations from the variation of the incident light, from inhomogeneous concentrations etc..., it is helpful to use two fluorescent molecules having distinct emitted wavelength, λ_{e1} and λ_{e2}, and a different sensitivity to the temperature variation. The ratio of the light emitted at each wavelength depending on the ratio $\Phi_1(T)/\Phi_2(T)$ only, it gives a better the temperature cartography. This technique using light intensity is less sensitive to the setup geometry and easiest to

calibrate. It uses a monochrome camera but necessitate the measure of two distinct wavelengths. Encapsulate fluorescent particles can be used as seeded particles for the PIV. The sensitivity of the LIF with temperature is small compared to CLC but the time resolution should be faster.

Experimental setup design

Water has been commonly used as working fluid in turbulent convection, and most of the experimental studies have been devoted to it. It was easy to use but water can become non-Bossinesq at high temperature differences. It is usually admitted that linear Oberbeck–Boussinseq approximation is valid if $\alpha\Delta T$ is small [123, 132]. $\alpha\Delta T \sim 0.01$ corresponds to a Rayleigh number of 8×10^{11} for a cell height about a meters and thus, it is almost in the interesting region where experiments disagree. Note that $\alpha\Delta T \sim 0.01$ corresponds to $\Delta T \sim 50K$. The viscosity change becomes of order of 50% for such a ΔT around room temperature. This property can actually be used to check the discrepancy induced by non-symmetrical viscous boundary layers. However, this effect seems to affect only poorly the efficiency of the heat transport [117]. Tab. 2 resumes the physical properties of water at room temperature.

Physical properties of water at 20 ^{o}C						
density	Ther.exp.	cin.viscosity	Ther. diff.	Ther. cond.	Ra	Pr
ρ (kg/m^3)	α(K^{-1})	ν (m^2/s)	κ(m^2/s)	$\lambda((W/m/K)$	$\Delta T = 1$K $H = 1$m	ν/κ
998.2	2.04×10^{-4}	1×10^{-6}	1.35×10^{-7}	0.5631	1.65×10^{-10}	7.42

Tab. 2 Physical properties and characteristic dimensionless parameters of water around 20 ^{o}C

The largest Rayleigh numbers obtained in water in laboratory scale experiments used a 1m height convective chamber with an aspect ratio of 1 or 1/2 [133, 134]. These already large scales seem to be a reasonable base to build an experiment. Indeed, around $Ra \sim 10^{12}$, the amount of power to provide and evacuate is of order of $Q = 20$ kW using the reasonable scaling: $Nu \sim 0.06Ra^{1/3}$ [133, 134]. The thermal boundary layers, e_κ are of order of one mm, thus they can be probed with a laser sheet. The characteristic velocity scale, representative of the large scale flow $U_o = \sqrt{\alpha g \delta T H}$ is of order of 0.3 m/s and thus the turnover time of this large structure is about τ_H =3s. Hence long measurements are necessary to get good statistics that include lot of turnovers of the flow (which can be considered as the largest correlation time). 4 days measurements will correspond to 100000 turnovers. On the other hand, the Kolmogorov time scale is about 5 ms hence it can be resolved by Encapsuled Thermochrome Liquid Crystal and it does not necessitate ultrafast cameras. The time scale associated with thermal plumes $\tau_\kappa = e_\kappa/U_o$ is also about 5 ms. Therefore the technical issue here to resolve all time scales, is to manage the acquisition, the storage and the analysis of the data by combining slow and fast acquisitions, real time analysis, database management etc....

For LIF technique, the wavelength of the light source has to be tuned to the absorption ray of the fluorescent molecules. For CLC, a white laser source must be used. A sketch of the experimental device is proposed in figure 5.1. One of the experimental difficulties will be to get a good visualization of the flow without lateral thermal leaks. The use of a double wall made

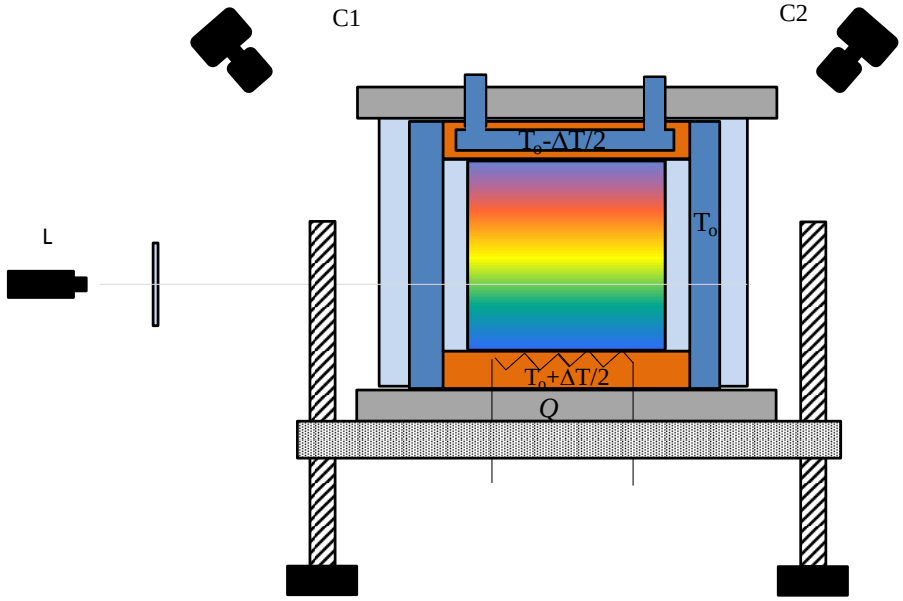

Figure 5.1: Sketch of a Convective cell in the Rayleigh–Bénard configuration. The cell is heated from below with the flux rate, q, in order to sustain a temperature gradient ΔT. The cell is immersed in a thermal bath maintained at T_o, in order to limit the thermal leaks. In addition it can allow an index-matching with boundaries. The cell is seeded with either encapsulate Cholesteric Thermochrome liquid crystals or encapsulate LIF particles. The laser (L) provides a horizontal laser sheet and the two cameras C1 and C2 allow the stereo-PIV as well as the temperature measurements in the horizontal laser sheet.

of thick insulating transparent boundary with an intermediate fluid maintained at the mid-cell temperature and with an optical index matched with the lateral boundary could be helpful to solve this issue. With this trick of index-matching, a cylindrical cell can be used as well as a square cell for the inner container. Calibration can be provided by a stable temperature gradient.

5.3 Measurement of the dissipation in an enclosed turbulent flow by multispeckle diffusing–wave spectroscopy

5.3.1 Motivations

We have seen in previous sections and especially in section 2.4, that the interplay between the fluctuations of injected power at large scale and dissipated power at small scale could have some impacts in the complex structure of turbulent flows. It is therefore an interesting experimental challenge to get a simultaneous measurement of these two global quantities well resolved in time.

Concerning the injected power, it is assumed to be a control parameter in most of the theory, however, in most experimental devices, one controls either the pump flow rate or the pressure gradient in channels and jets, the velocity of the propeller or its torque, the velocity or the force applied on models. When, for instance, the impellers rotation rate is controlled, therefore the fluctuations of the torque reveal the back action on the flow on the impeller. Although a control of the input power should be manageable and has been achieved recently [135], in practice it appears to be difficult, maybe because it necessitates some nonlinear feedback loops and because the fluctuations involve a large range of time scales. At least the injected power can be measured although some care should be taken concerning inertia and mechanical filtering [22]. Such a measurement have been performed in wave turbulence [22] and in the enclosed von Kármán turbulent flow, where the velocity is controlled and where the torque or power of the driving motors is measured [45, 46]. In these last cases, although the flow geometry and the Reynolds number are similar, different shapes of the power fluctuations are observed. This illustrates the sensitivity of this measurement to the details of the experimental device. In some configurations (e.g. with curved blades on the driving impellers), a forcing of the von Kármán flow with constant torque lets appear new large scale turbulent regimes [136, 137]. How these different driving affect the dynamics of the dissipative power is still an open question.

The measure of the global dissipated power is even more challenging. Indeed due to the structure of the Navier–Stokes equation, the dissipation occurs at small scales. Thus, one should be able to resolve extremely small scale gradienst in all the fluid volume to be able to resolve the global dissipated power. Usual experimental tools, like hot wires or zoomed PIV allow local measurements of dissipative structures but loose the global aspects of the dissipative power. Hence such measurement cannot be correlated to the injected power. Global temperature measurements and thermal budgets allow the estimation of the global dissipated power but thermal inertia prevents the measurement of the power fluctuations. Extremely small local thermometers (like thermochrome Liquid crystals) could be fast enough but they give local information and should not be able to resolve a temperature elevation at the Kolmogorov dissipative scale ΔT_η [1]. Jérome Crassous suggested the multidiffusive-wave spectroscopy as a powerful tool to measure the velocity gradients in turbid turbulent flows. Indeed this technique used initially to study statistical properties of colloidal particles [138, 139, 140] was extended to the study of the mechanical properties of complex media [141, 142, 143] and in solid state physics [121]. It has been employed in fluid mechanics to access to velocity gradients in shear flows [144, 145, 120, 146]. A similar technique of dynamics light scattering was used locally to measure velocity gradient in turbulent flows [147, 148, 149]. However this technique did not use the properties of the multi–diffusive light due to the smaller number of scatterers. Hence, it seems inappropriate to perform the global measurement of the dissipated power [150]. In the following we will first briefly report the method of multidiffusive–wave spectroscopy to underline its limitations and to show how it could give access to dissipated power. Then, we will try to estimate the relevance of this method to measure the dissipation in a von Kármán flow type with the available technologies.

[1] An estimate gives $\Delta T_\eta \propto \rho\nu^3 \cdot Re^{3/2}/(\lambda L^2)$, hence to obtain an already quite good minimal resolution of $\Delta T_\eta \sim 0.05$ K in a water cell of size $L \sim 10$ cm, one has to reach a Reynolds number of $Re \sim 4\times10^7$ corresponding to a velocity $U \sim Re \cdot \nu/L \sim 400$ m/s and an input power $P_I \sim \rho L^2 U^3$ about 8×10^5 kW !!

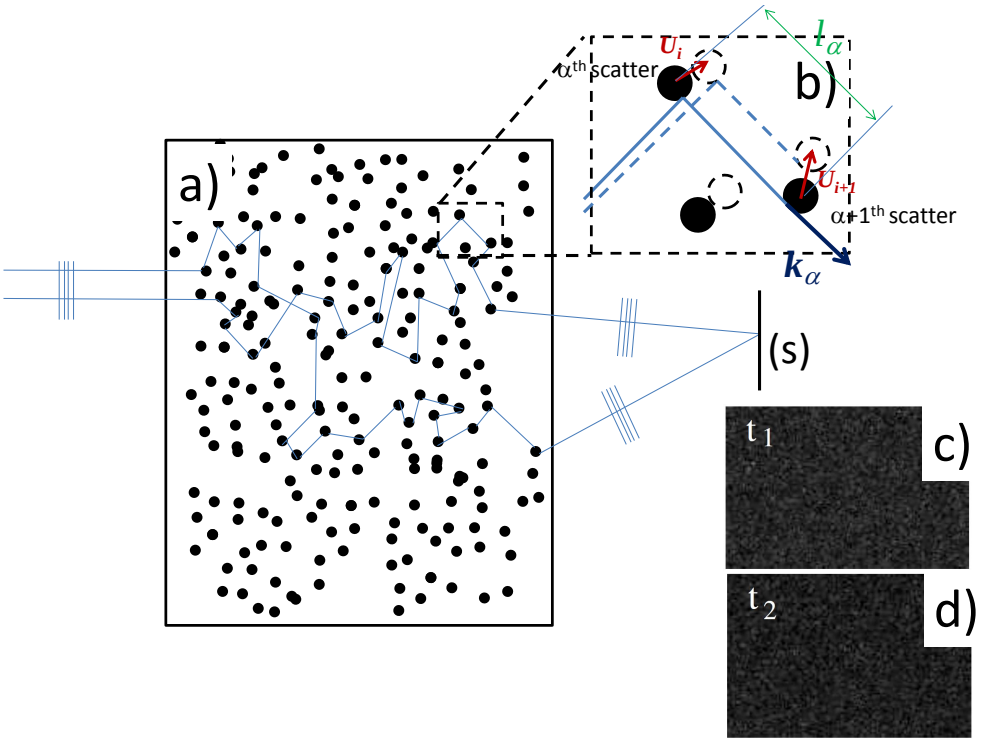

Figure 5.2: Sketch of the multidiffusing wave spectroscopy. a) illustrates the random walk of two light beams arising on the sensor (S) at the position r. b) Zoom on the scatterer displacement between two successive times. c–d) show the speckle patterns that can be obtained in retrodiffusion in the case of a solid deformation (from [121]).

5.3.2 The multidiffusing–wave spectroscopy

The diffusing wave spectroscopy (DWS) has been introduced by G.Maret and P.E. Wolf [138], and the theoretical background is well described in [144, 146, 121] for instance. Our aim here is to briefly report the theory of the DWS, insisting on the necessary assumptions allowing the theoretical predictions to hold. One considers a coherent light beam of wavelength, λ, propagating to a random network of elastic scatterers. Inside the turbid media the light beam is assumed to follow a random walk. Figure 5.2-a) sketches such a random walk of the beam. This approximation is valid in the weak scattering limit in which $k \cdot l >> 1$, with $k = 2\pi/\lambda$ and l is the scatterer mean free path. In this limit one can consider that the light propagates as beam in geometrical optics limit. Moreover, it assumes that we are in strong multiscattering regime imposing a sample size $L >> l$. The diffused light collected in any direction gives the speckle pattern shown on figure 5.2-c,d for two successive times. No information can be extracted from these patterns, but their time-correlation gives access to the displacement of the scatterers advected by the flow (cf figure 5.2-b)).

The theory of the DWS considers the normalized self–correlation function in time of the electric field $E(\mathbf{r},t)$ collected a point $\mathbf{r}$ of a sensor : $C_1(\mathbf{r},t) = \langle E(\mathbf{r},t) \cdot E(\mathbf{r},0)\rangle / \left(\langle E(\mathbf{r},t))\rangle\langle E(\mathbf{r},0)\rangle\right)$. This quantity is related to the measurable self–correlation function in time of light intensity $I(\mathbf{r},t)$ by $\langle I(\mathbf{r},t) \cdot I(\mathbf{r},0)\rangle / \left(\langle I(\mathbf{r},t))\rangle\langle I(\mathbf{r},0)\rangle\right) = 1 + \beta_e |C_1|^2$, with β_e an experimental constant of order unity.

The normalized self–correlation function $C_1(\mathbf{r},t)$ can be expressed as :

$$C_1(\mathbf{r},t) = I_o \sum_{n_r=1}^{\infty} P(n_r)\langle exp\left[j\Delta\phi_{n_r}(t)\right]\rangle \tag{5.2}$$

where $P(n_r)$ is the fraction of the total intensity I_0 remaining in all the paths including n_r scattering and arriving at the position $\mathbf{r}$ on the sensor. $\Delta\phi_{n_r}(t) = \sum_{\alpha=1}^{n_r}(\mathbf{k}_\alpha - \mathbf{k}_{\alpha-1})\cdot\Delta\mathbf{R}_\alpha(t)$ is the phase shift induced in a path of n_r scattering by all the motion of the scatterers, labelled, by α, included in this path. During the time t, the scatterer α moves from its initial position $\mathbf{R}_\alpha(0)$ to $\mathbf{R}_\alpha(t)$. The average $\langle\cdot\rangle$ is actually taken on all the paths of length n_r inciding on the probe at the position r. $(\mathbf{k}_\alpha - \mathbf{k}_{\alpha-1})$ is scattered wave number between the scatterers $\alpha-1$ and α (cf figure 5.2-b)). The phase shift $\Delta\phi_{n_r}(t)$ contains all the information about the dynamics of the scatterers. In the multiscattering regime, it is a sum over a large number of scattering. Thus the law of large number applies and its statistics can be assumed to be Gaussian and are characterized by its two first cumulants. Moreover in this case one can write:

$$\langle exp\left[j\Delta\phi_{n_r}(t)\right]\rangle = exp\left(j\langle\Delta\phi_{n_r}(t)\rangle\right)\cdot exp\left(\langle\Delta\phi_{n_r}(t)^2\rangle - \langle\Delta\phi_{n_r}(t)\rangle^2\right) \tag{5.3}$$

Assuming that the time t is short enough to get a ballistic motion of the scatterers so that $\Delta\mathbf{R}_\alpha(t) \sim \mathbf{U}(\mathbf{R}_\alpha)t$ and $\Delta\phi_{n_r}(t) \sim -kt\sum_{\alpha=1}^{n_r} l_\alpha\mathbf{e}_\alpha(\mathbf{e}_\alpha\cdot\nabla)\mathbf{U}(\mathbf{R}_\alpha)$, with $l_\alpha = ||\mathbf{R}_{\alpha+1} - \mathbf{R}_\alpha||$ and $\mathbf{e}_\alpha = (\mathbf{R}_{\alpha+1} - \mathbf{R}_\alpha)/l_\alpha)$. Here we assume that the characteristic scale of the velocity gradients is much larger than $l = \langle l_\alpha\rangle$. Finally one gets at the first order:

$$\begin{aligned}\langle\Delta\phi_{n_r}(t)\rangle \quad &\sim -\tfrac{1}{3}ktl\sum_{\alpha=1}^{n_r}\langle\nabla\cdot\mathbf{U}(\mathbf{R}_\alpha)\rangle \\ &= 0\end{aligned} \tag{5.4}$$

because we consider incompressible fluid. The second cumulant gives

$$\langle\Delta\phi_{n_r}(t)^2\rangle \sim -\frac{2}{15}(ktl)^2 n_r\epsilon(n_r) \tag{5.5}$$

where $\epsilon(n_r)$ is related to the strain tensor $\sigma_{ij}(\mathbf{R}) = \frac{1}{2}(\partial_i U_j + \partial_j U_i)$ as follows

$$\epsilon(n_r) = 2\int \sigma_{ij}^2(\mathbf{R})\rho_{n_r}(\mathbf{R})d^3R. \tag{5.6}$$

Hence in fluids, the variance of the phase shift of correlated speckle intensity is linked to the dissipation $D = \rho\nu\int\sigma_{ij}^2(\mathbf{R})d^3R$, but it is weighted by the density of path of length n_r passing at the point R. For a given experimental geometry, $P(n_r)$ and $\rho_{n_r}(\mathbf{R})$ will be given in the framework of the random walk.

In our experiment, we plan global measurements and we would like to enlighten the entire cell with an enlarged coherent beam and we would like to collect the beams transmitted through the entire cell. If the scatterer distribution is uniform in space, one can expect therefore that the number of path of length n will be uniform, hence $\rho_{n_r}(\mathbf{R}) \approx P(n_r)/V$ does not depend on space. Finally one gets:

$$C_1(\mathbf{r},t) = I_o\sum_{n_r=1}^{\infty} P(n_r)exp\left[\frac{4(klt)^2 n_r P(n_r)D}{15V\rho\nu}\right] \tag{5.7}$$

where $P(n_r)$ is given by the weight of the random walk crossing the experimental cell. It will depend on the cell geometry but it can be computed either analytically for simple geometries or at least numerically. We want to note that all speckle spots are independent. Therefore if we use the extended sensor of a camera, an average on all the pixels corresponds to an ensemble average. Hence, to compute the correlation function, one has to average over all pixels the product $I(\mathbf{r},t)\cdot I(\mathbf{r},0)$ measured by each pixel at different positions $\mathbf{r}$ i.e. no time-average is needed [151].

To conclude let us recall the successive assumptions made to reach equation (5.7), [120].

1. The weak scattering limit imposed $\lambda/2\pi << l = \frac{1}{n\sigma}$ with n the density of scatterer and σ the cross section of the scatterer.

2. Multidiffusion regime requires in contrast $l << L$ the characteristic system size.

3. The requirement of a ballistic displacement between two acquisition times imposes a motion of the scatterer smaller than the Kolmogorov scale between two image acquisitions.

4. The characteristic length scale of the velocity gradients has to be smaller than l. Ideally we would like $l \sim \eta$ and at least smaller than the Taylor micro-scale, λ_T, characterizing the velocity gradient and such that $\langle(\partial_{\mathbf{r}} u)^2\rangle \sim (u_{rms}/\lambda_T)^2$.

5. Scatterers should be homogeneously distributed, really passive, and enable to elastic weak scattering. Moreover we would like to keep a Newtonian fluid. These imply the use of really tiny isodense particles.

In the next part we will check if these requirements can be achieved in a turbulent flow.

5.3.3 Application to the measure of the dissipated power in turbulent flows

Although it is may be not the most relevant flow, one can select the von Kármán flow generated by two counter-rotating impellers as a possible candidate for such a study (see figure 5.3). Indeed in this flow the injected power can be estimated by the measure of the rotation rate and the applied torque on each impeller. The Reynolds number is unambiguously defined with the size of the impeller L and the impeller speed $\dot{\Omega}L$ thus $Re = \dot{\Omega}L^2/\nu$. We cannot expect to enlarge a coherent beam more than about ten cm. Then let us take $L = 0.1$ meter. Rotation rates from 1 to 10 Hz are commonly accessible in water, thus one can expect a Reynolds number of $Re \sim 10^4 - 10^5$. This corresponds to a Kolmogorov scale $\eta \sim LRe^{-3/4} \sim 100 - 17\mu m$. The Taylor micro-scale can be estimated as $\lambda_T \sim LRe^{-1/2}$ ranges from 1 to 0.3 mm. Although we do not reach huge Reynolds numbers, we are inside a turbulent regime with about 3 decades of inertial range.

In their study of the Taylor–Couette instability by DWS, Bicout and Maret [146] used TiO_2 particles suspended in water (with addition of surfactant agents). The size of the particles is about 0.3 μm. For a volume fraction of $\Phi = 0.25\%$, corresponding to an increase of viscosity to $1.15 \times 10^{-6} m^2/s$, they estimated a mean free path about 50 μm. Wu *et al* [145] in their square pipe flow used polystyrene spherical particles of 0.41 μm with a volume fraction of 2%. They

estimate the beam mean free path l about 100 μm . In these conditions using coherent laser light in the visible spectrum, the requirements 1, 2 and 5 are fulfilled. We get also a mean free path much smaller than λ_T, and of order of than η, thus requirement 4 is filled. The most sensitive point concerned the requirement 3, which fixes the needed acquisition rate.

To resolve the ballistic regime, one needs a scatterer displacement $\Delta R \sim \eta$ during an acquisition time delay. Crudely, one can take $\delta t \sim 1/\Delta f \sim \eta/(L \cdot \Omega)$ corresponding to a camera frame rate of $\Delta f = 500$ kHz ! Actually this high frame rate is reachable with commercial high speed cameras, through a reduction of the resolution at 132X64 pixels. This lets still 2816 independent events when the correlations are averaged over the pixels of the sensor, knowing that the best signal/ noise ratio is reached when a speckle spot occupies 3 pixels in average [151].

Moreover this previous estimate is probably too crude. Indeed, a displacement at uniform speed does not induce the phase shift. Thus, one may assume that a more relevant estimate is to use the velocity increment, δU_η, at the scale η. Therefore $\Delta f = 1/\tau_\eta$ with $\tau_\eta = (nu/\epsilon)^{1/2}$ is the Kolmogorov time scale, where ϵ is the dissipation rate per unit of mass. Actually it is more or less the characteristic time scale appearing in equation (5.7). Assuming $\epsilon = U^3/L$, one gets: $\Delta f = (U^3/L\nu)^{1/2} \sim 3$kHz. Actually to resolve τ_η, one needs to go at least 10 times faster, which is still accessible with a high speed camera within 640 x 480 pixels resolution (e.g. the Phantom V1210 from vision research) corresponding to the opportunity of 100000 independent instantaneous events that can be averaged. To insure that no bias is introduced by the use of δU_η instead of the full velocity U, one can perform measurements at both frame rates with a single high speed camera by reducing the resolution and check the consistency of the results.

Other miscellaneous problems would have to be overcome. For instance, if in order to have an easy access to the injected power, we select the von Kármán flow, we should have to make the impeller as transparent as possible for the light beam, otherwise theirs motions should dominate the multiscattering. To solve that, one can manufacture the impellers with (high quality) transparent material, index–matched with the fluid without the scatterers. Although the correlation method used here to extract the dynamics, should smear-out all optical aberrations, it may be wise to reduce them as much as possible, by using a square cell or a cylindrical cell in a square container, and to make all interfaces transparent by index matching. Most of the DWS measurements are performed in relatively narrow cells or/and they probe the backscattered light. Due to mutidiffusion only a small part of the light will be transmitted. Moreover, this amount, which is known by the random walk theory in cases of elastic scattering, should be decreased by inelastic effects. However, it should be proportional to the incoming light intensity and powerful laser sources are now available. Finally the high speed camera will generate a large amount of data and the storage and management of this data will become an important issue. The use of graphic computing unit (GPU) to process in parallel the correlation functions of each pixel of the camera could be a useful tool in our case. A good complete description of the optical device and precise description of DWS experimental setup can be found in [151, 121].

To conclude, let us remind that the aim is actually to measure the characteristic time of equation (5.7) which correspond to τ_η. We hope to estimate it quickly enough to deduce the slow evolution of $D(t)$, compared to τ_η, that survives, if any, to the spatial averaged (actually average over the optical path). It should be noticed that the fluctuations of a global quantity as the dissipated power can be too small to be measurable. Indeed if the dissipation occurs through

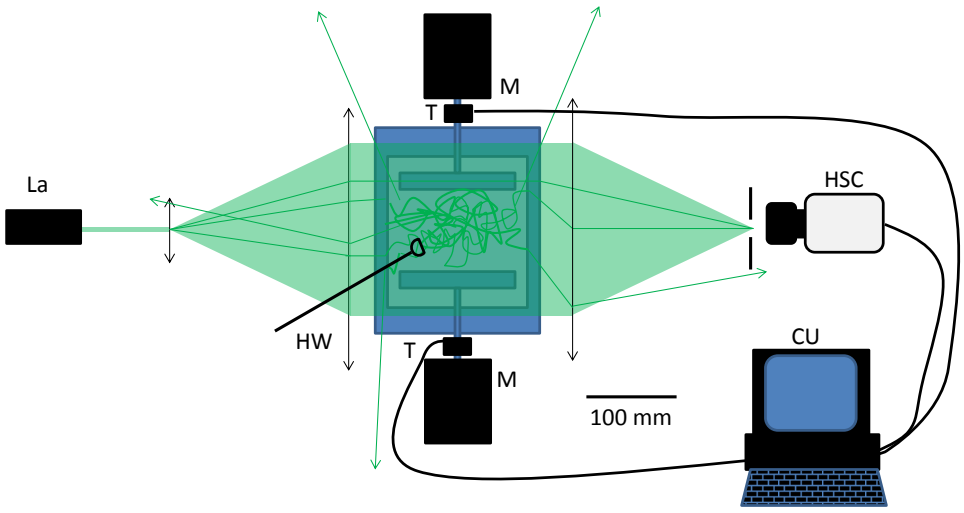

Figure 5.3: Sketch of an experimental setup using multidiffusing wave spectroscopy to measure dissipation in the von Kármán flow. The laser beam coming from a laser power source (La) is enlarged to enlighten all the von Kármán flow. Containers and impeller are index matched with the unseeded fluid. Transmitted light is collected into a High Speed Camera (HSC) and is processed by the Computational Unit (CU). Speeds and torques imposed by the Motors (M) are measured by a Tachymeter and a Torquemeter (T). Hot Wire (HW) or Laser Doppler velocimetry is added to allow local measurements.

many incoherent events, then the spatial average should cancel the fluctuations. However if the dissipation is dominated by few intense coherent structures, this measure should give an information on their life time. Nevertheless, even if the fluctuations cancel out, some measurements about the mean correlation time of the dissipation and its variation with the Reynolds are very suitable information that justify the experiment by itself. Moreover, with the relevant optical device, spatially resolved measurements and local probing are manageable [143]. In any case, the first relevant measurement to do, will be with turbulence in decline, i.e. after a sudden stop of the forcing. This should allow the calibration of the DWS measurements by combining it with some local probes like Laser Doppler velocimetry (since the media is already seeded with particles) or/and some hot wire anemometry. We will have also to measure the applied torque on the impellers and their speed in order to know the injected power.

Bibliography

[1] S. Aumaître, S.Fauve, P. Poggi and S. Mc Namara, Euro. Phys. J. B. **vol 19** (2001)

[2] G. Gallavotti, E.D.G. Cohen, Phys. Rev. Lett. **74** pp 2694 (1995)

[3] J. Kurchan, C.R. Acad. Sci. IV (2) pp 239 (2001)

[4] C. Jarzynski, Phys. Rev. Lett. **78** pp 2690 (1997)

[5] C. Maes, J. Stat. Phys. **95** pp 367(1999)

[6] G. E. Crooks, Phys. Rev. E **60** pp 2721 (1999).

[7] Noise in Dynamical Systems, edited by F. Moss and P.V. E. McClintock (Cambridge University Press, Cambridge, England, 1989)

[8] Horsthemke W. and Lefever R., Noise-Induced Transitions (Springer-Verlag, 1984)

[9] J. Farago, J. Stat. Phys. **118** pp 373 (2004)

[10] F. Pétrélis, S. Aumaître, Eur. Phys. J. B **34** pp 281 (2003)

[11] S. Aumaître, F. Pétrélis, K. Mallick, Phys. Rev. Lett. **95**, 064101 (2005)

[12] S. Aumaître, F. Pétrélis, K. Mallick, J. Phys. Stat. **123** pp909 (2006)

[13] F. Pétrélis, S. Aumaître, K. Mallick, Euro. Phys. Lett. **79** 4004 (2007)

[14] F. Pétrélis, S. Aumaître, S. Fauve, Phys. Rev. Lett. **94** 070603 (2005)

[15] N. Leprovost, S. Aumaître, K. Mallick, Eur. Phys. J. B **49** pp453 (2006)

[16] F. Pétrélis, Thèse de doctorat,

[17] M. Lucke, F. Schank, Phys. Rev. Lett. **54**, pp1465 (1984)

[18] K. Mallick, Ph Marcq Eur. Phys. J. B **36** pp119 (2003)

[19] H. Fujisaka, T. Yamada, Prog. Theor. Phys. **74** pp 918 (1985)

[20] N. Platt, E.A. Spiegel, C. Tresser, Phys. Rev. Lett. **70** pp 279 (1993)

[21] D. Fuster, J.-P. Matas, S. Marty, S. Popinet, J. Hoepfnner, ACartellier and S. Zaleski, J. Fluid Mech. **736** pp150–176

[22] E. Falcon, S. Aumaître, C. Falcón, C. Laroche, S. Fauve , Phys. Rev. Lett. **100**, 064503 (2008)

[23] R. Kubo, M. Toba, N. Hashitsume, *Statistical Physics II: Nonequilibrium Statistical Mechanics*, (Springer Series in Solid–State Sciences, Springer, Berlin 1985).

[24] J. Farago, J. Stat. Phys. **107** pp 781 (2002)

[25] G.M. Wang, E.M. Sevick, E. Mittag, D.J. Searles, D.J. Evans, Phys. Rev. Lett. **89** n^o 050601 (2002)

[26] B. Blickle, T. Speck, L.Helden, U. Seifert, C. Bechinger, Phys. Rev. Lett. **96** n^o 070603 (2006)

[27] P. Job, A. Petrosyan, S. Ciliberto, EuroPhys. Lett. **81**(6) n^o 070603 (2008)

[28] M. Bandi and C. Connaughton to be published in Review of psychopathology Released

[29] N.G. van Kampen *Stochastic Processes in Physics and Chemistry*, (3rd Edition, North-Holland Personal Library, 2007)

[30] H. Risken *The Fokker-Planck Equation–Method of Solution and applications* (2d Ed, Springer, Berlin, 1996)

[31] W. Feller *An introduction to Probability Theory and Its Applications* Vol. II (2d Ed, J. Wiley & sons, NY, 1971)

[32] : I.S Gradshteyn, I.M Ryzkik *Table of integrals, Series and Products* (4th Ed, Academic Press, NY, 1965)

[33] C.C. Graig, Ann. Math. Statist. **7** (1936) 1–15

[34] V. E. Zakharov, V. Lvov, and G. Falkovich, *Kolmogorov Spectra of Turbulence* (Springer-Verlag, Berlin, 1992)

[35] E. Falcon, C. Laroche, S. Fauve, Phys. Rev. Lett. **98** n^o 094503 ($\geq$ 2006)

[36] Gustavo Düring, Christophe Josserand, and Sergio Rica Phys. Rev. Lett. 97, 025503 (2006)

[37] L. Schimanski–Geier and Ch. Zülicke, Z. Phys. B **79** (1990) 451–460

[38] E.B. Geldzer, Sov. Phys. Dokl. **18** (1973)

[39] M. Yamada, K. Ohkitani, J. Phys. Soc. Jpn **56** pp 4210 (1987)

[40] L. Biferale Annu. Rev. Fluid Mech. **35** (2003) pp 441-468

[41] S. Aumaitre, S. Fauve, Europhys. Lett. **62**–6 (2003) 822–828

[42] X.-D. Shang, X.-L. Qiu, P. Tong, K.-Q. Xia, Phys. Rev. Lett. **90** n^o 07501(2003)

[43] W.L. Shew, Y. Gasteuil, M. Gibert, P. Metz and J.F. Pinton arXiv:physics/0703245

[44] O. Shiskina and C. Wagner, Phys. Fluids **90** n^o 085107 (2007)

[45] R. Labbé, J.F. Pinton, S. Fauve, J. Phys II France **6** pp 1099 (1996)

[46] J.-H.C. Titon, O. Cadot, Phys. Fluids **15** pp 625 (2003)

[47] F. Ravelet, A. Chiffaudel, F. Daviaud, J. Fluid Mech. **601** (2008) pp339

[48] D.J. Evans, E.D.G. Cohen, G.P. Morris, Phys. Rev. Lett. **71** pp 2041 (1993)

[49] U. Frisch *Turbulence* (Cambridge university Press 1995)

[50] F. Anselemet *et al* J. Fluids Mech. **140** (1986) pp 63

[51] R.H. Kraichnan, J. Fluid Mech. **62** pp305 (1974)

[52] R.S. Ellis, *Entropy, large distributions and statistical mechanics* (Springer-Verlag, New York, 1985)

[53] L. Kadanoff *et al* Phys. Fluids **7**–3 (1995) pp617

[54] E. Leveque, Z.S. She Phys Rev. E **55**–3 (1997) pp 2789

[55] V.N. Desnyansky and E.A Novikov, Ivz. Akad. Nauk SSSR Fiz. Atmos. Okeana **10**(2) (1974) pp 127–136

[56] S. Cerutti and C. Meneveau, Phys. Fluids **10**–4 (1998) pp 928–936

[57] S.T Bramwell, P.C. Holdsworth, J.P. Pinton, Nature **396** pp 552 (1998)

[58] M Clusel, J.-Y. Fortin, P.C. Holdsworth, EuroPhys. Lett. **76**(6) pp 1008 (2006)

[59] G. Palmas, T. Meyer, R. Labbé, Phys. Rev. E **66** n^o 026108 (2002)

[60] C. Lamriben, P.P Cortet, F. Moisy J. of Phys.: Conf. Series **318** (2011) 042005.

[61] B. Tao, J. Katz,and C. Meneveau, Phys. Fluids **12**–4 (2000) pp 941–944

[62] A. Pumir Phys. Fluids, **8**–11 (1996) pp3112–3127

[63] S. Aumaître, Thèse de Doctorat, ENS-Lyon (1999)

[64] E. Falcon, S. Aumaître, P. Évesque *et al*, Europhys. Lett. **74** –5 (2006) pp 830–836

[65] S. Aumaître, S. Fauve, Phys. Rev E, **73** 010302(R) (2006)

[66] S. Aumaître, J. Farago, S. Fauve and S. Mc Namara, Eur. Phys. J. B **42** (2004) pp255–261

[67] S. Aumaître, A. Alastuey, S. Fauve, Euro. Phys. J. B. **54**–2 263–266 (2006)

[68] E. Opsomer, F. Ludewig and N. Vandewalle, Euro. Phys Lett.,**99** (2012) 40001

[69] S. Aumaître, T. Schauntz, C.A Krülle and I. Rehberg, Phys Rev Lett **90**–11 114302 (2003)

[70] S. Aumaître, C.A. Krülle and I. Rehberg, Phys Rev E **64** 041305 (2001)

[71] S. Aumaître, C. Plus, J.N; McElwaine and J. Gollub Phys Rev E **75** 061307 (2007)

[72] GDR MiDi, Eur. Phys. J E **14** (2004) pp341

[73] N.J. Balmforth, Y. Forterre, O. Pouliquen, J. Non–Newtonian Fluid Mech. **158** (2009) pp46–53

[74] P. Gutierrez and S. Aumaître submitted to Phys Fluid (2013)

[75] F. Moisy, M. Rabaud, K. Salsac, Exp. In Fluids **46**–6 (2009) pp1021–1036

[76] M. Berhanu, A. Kudrolli, Phys Rev Lett. **105**–9 098002 (2010)

[77] M.-J. Dalbe , D. Cosic,M. Berhanu *et al.*, Phys Rev. E 83–5 051403 (2011)

[78] A. Soulier and S. Aumaître submitted to Am. J Phys. (2014)

[79] J.S. Olafsen, J.S. Urbach, Phys. Rev. Lett. **81**-20 (1998) pp 4369-4372

[80] G. Castillo, N. Mujica, R. Soto, Phys. Rev. Lett. **109** 095701 (2012)

[81] P. Melby F. Vega Reyes, A. Prevost *et al*, J; Phys.: Condens Matter **17** (2005) S2689–S2704

[82] S. Warr, J.M. Huntley, Phys. Rev. E **52**–5 (1995) pp5596–5601

[83] N. F. Carnahan and K.E. Startling, J. Chem. Phys. **51**–2 (1969) pp 635–636

[84] L. Oyarte, P. Gutierrez, S. Aumaître and N. Mujica, Phys Rev E **87**-2 022204 (2013)

[85] P.A Davidson *An Introduction to Magnetohydrodynamics* (Cambridge Texts in Applied Mathematics, Cambridge University Press UK, 2001)

[86] S. Fauve and F. Petrelis *The dynamo effect* Lecture Notes of the Rencontres Nonlénaire

[87] R. Stieglitz, U. Müller, Phys. fluid **13** (2001) pp561

[88] A. Gailitis *et al*, Phys. Rev. Lett. **86** (2001) pp3024

[89] R. Monchaux *et al*, Phys. Rev. Lett. **98** 044502 (2007)

[90] M. Berhanu *et al*, Europhys Lett. **77** 59001 (2007)

[91] R. Monchaux, Thèse de doctorat

[92] M. Berhanu, Thèse de doctorat

[93] F. Pétrélis N. Mordant and S. Fauve, Geophys. Astrophys. Fluid Dyn. **101** (2007) pp289

[94] F. Ravelet *et al*, Phys. Rev. Lett. **101** 074502 (2008)

[95] R. Monchaux *et al*, Phys. Fluids **21** 035108 (2009)

[96] S. Aumaître *et al* C.R. Physique **9** (2008) pp689–701

[97] M. Berhanu *et al*, J. Fluid Mech. **641** pp 217–226

[98] B. Gallet *et al*, Phys. Rev. Lett.

[99] F. Pétrelis, S. Fauve, Phil. Trans. R. Soc. A **368**–1916 (2010) pp 1595-1605

[100] E. D. Siggia, Annu. Rev. Fluid Mech. **26**, 137 (1994).

[101] S. Grossmann and D. Lohse, J. Fluid Mech., **400**, (2000).

[102] S. Aumaître and S. Fauve, Europhys. Lett. **62**, 822 (2003).

[103] S. Chandrasekhar, *Hydrodynamic and hydromagnetic stability*, Clarendon Press (Oxford, 1961).

[104] S. Fauve, C. Laroche, and A. Libchaber, J. Physique Lettres **45**, 101 (1984).

[105] S. Fauve, C. Laroche, A. Libchaber and B. Perrin, Phys. Rev. Lett. **52**, 1774 (1984).

[106] P. Tabeling Phys. Rev. Lett. **49** (1982) pp 460

[107] J. Boisson, A. Klochko, F. Daviaud, V. Padilla and S. Aumaître Phys. Fluids bf 24 , 044101 (2012)

[108] P. Gutierrez PhD thesis (2013)

[109] J. Larkin, W. Goldburg, M.M. Bandi, Physica D **239** (2010) 1264–1268

[110] S. Lovecchio, C. Marchioli, A. Soldati,Phys. Rev. E **88**, 033003 (2013)

[111] Cobelli P., Maurel A., Pagneux V., Petitjeans P. Exp. Fluids, **46**–6 (2009) pp1037-1047

[112] M. A. Tayfun, J. Geophys. Res. **85** (1980), pp 1548–1552.

[113] O.M Phillips, J. Fluid Mech, **5**, (1959) pp 177–192

[114] M.A.C Teixeira and S.E Belcher, J. Fluid Mech, **258**, (2002) pp 229–267

[115] P.A Davidson and R. Lindsay JFM **362** (1998) pp 273

[116] A. Pedchenko, S; Molokov, J. Priede, A. Lukyanov, P.J. Thomas, Europhys. Lett. **88**–2 (2009)

[117] G. Alhers, S. Grossmann & D. Lhose, Rev. Mod. Phys. **81**–2 (2009) pp503

[118] F. Chilla and J. Schumacher, Eur. Phys. J. E **35**:58 (2012)

[119] D. Lohse, K.D. Xia, Annu. Rev. Fluid Mech. **42** (2010) pp335-364

[120] D. Bicout and G. Maret, Physica A **199** (1993) pp 387–411

[121] M. Erpelding, A. Amon and J. Crassous, Phys Rev E **78** 046104 (2013)

[122]) A. F.Wibisonoa,1, Y. Ahna,1, W.C. Williams, Y. Addadc, J.I. Lee Nucl. Eng.& Des. **262** (2013) 390– 403

[123] W.V.R. Malkus, WHOI GFD Notes ref. 64–46 (1964)

[124] W.V.R. Malkus, Proc. R. Soc. London Ser. A **225** (1954) pp185 & pp 196

[125] E. A. Spiegel Ann. Rev. Astro. and Astrophys. **9** (1971) 323-352

[126] S. Grossmann & D. Lhose, Phys Fluids **16** 2004 pp 4462

[127] X. Chavanne *et al* Phys. Rev. Lett. **79**–19 (1997)

[128] S. Funatani, N. Fujisawa, H. Ikeda Meas. Sci. Technol. **15** (2004) pp983

[129] N. Fujisawa, S. Funatani, N. Katoh, Exp. In Fluids **38** (2005) pp291

[130] P. G. de Gennes and J. Prost *The physics of Liquid Crystals* (Oxford University Press UK, 1993)

[131] R. Guillerm, A. Prigent & I. Mutabazi, C. R. RNL (2010) pp 79–84

[132] D.D. Gray, A. Giorgini, Int. J. Heat Mass Transfer **19** (1976) pp545

[133] C. Sun, L.Y Ren, H. Song, K.E. Xia, J Fluid Mech. **545** (2005) pp 165–174

[134] J.C. Tisserand, M. Creyssels, Y. Gasteuil *et al* Phys fluids **23** 015105 (2011)

[135] R. Labbe private communication

[136] B. Saint-Michel. PhD thesis, 2013

[137] B. Saint-Michel, B. Dubrulle, L. Marié, F. Ravelet and F. Daviaud, Forcing-type-dependent stability of steady states in a turbulent swirling flow, submitted to Phys. Rev. Let. (2013)

[138] G. Maret, P.E. Wolf, Z. Phys. B— Condense Matter **65** (1987) pp 409–413

[139] D.J. Pine, D.A.Weitz, P.M. Chaikin and E. Herbolzheimer, Phys. Rev. Lett. **60**–12 (1988) pp1134–1137

[140] D.J. Pine, D.A.Weitz, J.X. Zhu and E. Herbolzheimer, J. Phys France **51** (1990) pp2101-2127

[141] G. Maret, Current Opinion in Colloid & Interface Science **2**–3 (1997) pp251-257

[142] A. Amon, R. Bertoni and J. Crassous, Phys Rev E **87** 012204 (2013)

[143] J. Crassous, Eur. Phys. J. E **23** (2007) pp145–152

[144] D. Bicout, E. Akkermans and R. Maynard, J. Phys I **1** (1991) pp471–491

[145] X–L. Wu, D.J. Pine, P.M. Chaikin, J.S. Huang and D.A.Weitz, J. Opt. Soc. Am. B **7** (1990) pp15–20

[146] D. Bicout and G. Maret, Physica A **210** (1994) pp 87–112

[147] P.Tong and W.I. Goldburg, Phys. Fluids **31**-10 (1988) pp2841–2848

[148] W.I. Goldburg, P.Tong, H.K Tang, Physica D **38** (1989) pp134–140

[149] S. Stefanus S. Steers, W.I. Goldburg, Physica D **240** (2011) pp 1873–1876

[150] W. Goldburg, Am J Phys**67**-12 (1999) pp1152–1160

[151] V. Viasnoff, F. Lequeux, and D.J. Pine, Rev. Sci. Instrum. **73**–6 (2002) pp2336–2344